PTB bericht
Wissenschaftliche Veröffentlichungen

Diss-15
Juni 2025

Dissertation

Mutaib Mohammed Zackaria

Towards Reducing the Measurement Uncertainty of Rockwell Hardness Testing

ISSN 2941-1297
ISBN 978-3-944659-47-3

DOI 10.7795/110.20250619

Physikalisch-Technische Bundesanstalt

Dissertationen
PTB-Diss-15
Braunschweig, Juni 2025

Mutaib Mohammed Zackaria

Towards Reducing the Measurement Uncertainty of Rockwell Hardness Testing

ISSN 2941-1297
ISBN 978-3-944659-47-3

DOI 10.7795/110.20250619

Empfohlene Zitierweise/recommended citation

Zackaria, M., 2025. *Towards Reducing the Measurement Uncertainty of Rockwell Hardness Testing*. Dissertation, Technische Universität Braunschweig. Braunschweig: Physikalisch-Technische Bundesanstalt. PTB-Bericht Diss-15. ISBN 978-3-944659-47-3.
Verfügbar unter: https://doi.org/10.7795/110.20250619

Herausgeber:
Physikalisch-Technische Bundesanstalt
ISNI: 0000 0001 2186 1887

Presse und Öffentlichkeitsarbeit

Bundesallee 100
38116 Braunschweig

Telefon: (05 31) 592-93 21
Telefax: (05 31) 592-92 92
www.ptb.de

Towards Reducing the Measurement Uncertainty of Rockwell Hardness Testing

Von der Fakultät für Maschinenbau
der Technischen Universität Braunschweig
zur Erlangung der Würde

eines Doktor-Ingenieurs (Dr.-Ing.)

genehmigte Dissertation

von:	Mutaib Mohammed Zackaria
geboren in:	Margao, Goa

eingereicht am:	05.12.2024
mündliche Prüfung am:	09.05.2025

Vorsitz:	Prof. Dr.-Ing. Michael Müller
Gutachter:	Prof. Dr.-Ing. Rainer Tutsch
Gutachter:	Univ.-Prof. Dr.-Ing. Klaus Dilger
Gutachter:	Dr. Uwe Brand

2025

https://doi.org/10.7795/110.20250619

Abstract

Rockwell hardness values obtained by performing a Rockwell hardness test give an indication about some of the mechanical properties of metals. The prevalence of this value and the widespread recognition it enjoys across the industry is due to the simplicity of its definition and the low cost of testing. However, for a unit to be trusted and internationally accepted, it must be well-defined, and its realization at the highest level of the calibration pyramid must be undertaken with the least amount of measurement uncertainty. Since the Rockwell scale is an empirical scale, the definition of the unit is mainly based on measurement procedures developed by national metrology institutes (NMI). Therefore, it is vital for low measurement uncertainties that a unified scale and well-defined standardized procedures are used by the NMIs.

A hurdle hampering the implementation of a standardized testing cycle is the adherence to the ISO 6508 without performing time-consuming pre-measurements on hardness reference blocks. This work builds on a method developed by the Physikalisch-Technische Bundesanstalt (PTB) that makes use of measurement data from the preload phase of a Rockwell hardness test to perform the calibration without pre-measurements. The definition of the estimating parameters is improved, and the method is extended to all Rockwell scales. Furthermore, this automated approach is developed to be independent of the hardness testing machine by identifying and measuring the key factors and validating the results through an interlaboratory comparison. This work also reviews the available methods of correction of the measured Rockwell hardness value on the basis of the measured indenter geometry. It has been shown that the determination of the accurate indenter radius and opening angle for Rockwell hardness diamond indenters is crucial for an effective correction of the measured hardness value. Traditionally, tactile methods are used to extract 2D profiles of the indenter topography and to determine the tip radius. In this work, a novel method to evaluate the entire 3D spherical tip measurement data is proposed. This method also assists in exploring the limits and capabilities of a confocal laser scanning microscope (CLSM). It has been shown that a CLSM can be used to perform calibrations of the Rockwell indenter tip radius, contingent upon a few caveats. Finally, a measurement uncertainty budget for calibrating the indenter tip radius with a CLSM and the improvement in the measurement uncertainty of the Rockwell hardness test resulting from using the measured radius are presented.

https://doi.org/10.7795/110.20250619

Abstract (German)

Rockwell-Härtewerte, die durch eine Rockwell-Härteprüfung ermittelt werden, geben Aufschluss über einige mechanische Eigenschaften von Metallen. Die weite Verbreitung dieses Wertes und seine breite Anerkennung in der Industrie sind auf die Einfachheit seiner Definition und die geringen Prüfkosten zurückzuführen. Damit eine Einheit jedoch vertrauenswürdig und international anerkannt ist, muss sie genau definiert sein, und ihre Umsetzung auf der obersten Ebene der Kalibrierungspyramide muss mit der geringsten Messunsicherheit erfolgen. Da die Rockwell-Skala eine empirische Skala ist, basiert die Definition der Einheit hauptsächlich auf Messverfahren, die von nationalen Metrologieinstituten (NMI) entwickelt wurden. Daher ist es für geringe Messunsicherheiten von entscheidender Bedeutung, dass die NMIs eine einheitliche Skala und genau definierte standardisierte Verfahren verwenden.

Eine Hürde, die die Umsetzung eines standardisierten Prüfzyklus behindert, ist die Einhaltung der ISO 6508 ohne zeitaufwändige Vormessungen an Härtevergleichsplatten. Diese Arbeit baut auf einer von der Physikalisch-Technischen Bundesanstalt (PTB) entwickelten Methode auf, die Messdaten aus der Vorlastphase einer Rockwell-Härteprüfung nutzt, um die Kalibrierung ohne Vormessungen durchzuführen. Die Definition der Schätzparameter wurde verbessert und die Methode auf alle Rockwell-Skalen erweitert. Darüber hinaus wird dieses automatisierte Verfahren so entwickelt, dass es von der Härteprüfmaschine unabhängig ist, indem die Schlüsselfaktoren identifiziert und gemessen werden und die Ergebnisse durch einen laborübergreifenden Vergleich validiert werden. In dieser Arbeit werden auch die verfügbaren Methoden zur Korrektur des gemessenen Rockwell-Härtewerts auf der Grundlage der gemessenen Eindringkörpergeometrie untersucht. Es wurde gezeigt, dass die Bestimmung des genauen Eindringkörperradius und des Öffnungswinkels für Rockwellhärte-Diamant-Eindringkörper entscheidend für eine wirksame Korrektur des gemessenen Härtewerts ist. Traditionell werden taktile Methoden verwendet, um 2D-Profile der Topografie des Eindringkörpers zu extrahieren und den Spitzenradius zu bestimmen. In dieser Arbeit wird eine neuartige Methode zur Auswertung der gesamten 3D-Messdaten der sphärischen Spitze vorgeschlagen. Diese Methode hilft auch dabei, die Grenzen und Möglichkeiten eines konfokalen Laser-Scanning-Mikroskops (CLSM) zu erkunden. Es wurde gezeigt, dass ein CLSM zur Kalibrierung des Spitzenradius eines Rockwell-Eindringkörpers verwendet werden kann, wenn einige Vorbehalte beachtet werden. Schließlich werden ein Messunsicherheitsbudget für die Kalibrierung des Radius des Eindringkörpers mit einem CLSM und die Verbesserung der Messunsicherheit der Rockwell-Härteprüfung, die sich aus der Verwendung des gemessenen Radius ergibt, vorgestellt.

https://doi.org/10.7795/110.20250619

Declaration

I hereby declare that this work titled "Towards reducing the measurement uncertainty of Rockwell hardness testing" is a record of original work carried out by me at the Physikalisch-Technische Bundesanstalt, Braunschweig, Germany.

I confirm that:

- I have written this thesis without any external help and without the use of documents and aids other than those stated in the references.
- This work was undertaken to obtain a doctoral degree in Mechanical Engineering from the Technische Universität Braunschweig.
- There are no known conflicts of interest associated with this work and that the outcome has not been influenced or altered based on hidden financial support.
- All the sources have been listed.

Parts of this work have been published in the following scientific journals:

1. Zackaria M, Menelao F, Nimptsch D, Stegmaier T, Beisel P, Reinstaedt R, Brand U and Tutsch R 2022 Universal automation approach for efficient calibration of Rockwell hardness reference blocks *IMEKO 24th TC3, 14th TC5, 6th TC16 and 5th TC22 International Conference (Cavtat-Dubrovnik, Croatia)*
2. Zackaria M, Menelao F, Felgner A, Brand U and Tutsch R 2024 Correcting Rockwell hardness values based on improved measurements of diamond indenters using confocal laser scanning microscope *Measurement: Sensors* **38** 101446, doi:10.1016/j.measen.2024.101446
3. Zackaria M, Felgner A, Menelao F, Ahbe T, Brand U and Tutsch R 2024 Calibration of the spherical tip radius of Rockwell hardness diamond indenters using a confocal laser scanning microscope *Measurement Science and Technology* **35** 125017

Mutaib Mohammed Zackaria

Date: 05.12.2024

https://doi.org/10.7795/110.20250619

Acknowledgement

I am deeply grateful to Dr. Ludger Koenders for believing in me and providing me the opportunity to pursue research and a PhD in mechanical engineering. This incredible opportunity has been a pivotal moment in my life, and I cannot thank him enough for his trust and support.

My heartfelt thanks go to Mr. Febo Menelao, who generously shared his extensive knowledge of hardness metrology with me. His dedication to teaching me the nuances of the field—day in and day out—has been invaluable.

A special thank you to Dr. Uwe Brand for his unwavering support during my time at the PTB. As my supervisor, he has gone above and beyond, offering constant encouragement and guidance. His mentorship has greatly influenced both my work and my personal growth, and for that, I am profoundly thankful.

I would also like to express my deepest gratitude to Prof. Dr.-Ing. Rainer Tutsch and the Institut für Produktionsmesstechnik (iprom) of the Technische Universität Braunschweig. As my *Doktorvater*, his dedication, invaluable feedback, and generous investment of time have been instrumental in shaping my research. I could not have asked for a more supportive doctoral supervisor.

I also wish to thank Univ.-Prof. Dr.-Ing. Klaus Dilger for agreeing to review this work as an examiner. In addition, I thank Prof. Dr.-Ing. Michael Müller for accepting the chairmanship of the doctoral committee.

The technical aspects of this work would not have been possible without the cooperation and collaboration of my colleagues at the PTB and the industry project partners. I am immensely grateful to each of you for your contributions and for fostering a fruitful and collaborative environment.

Finally, I want to thank my parents and siblings, my wife and children, and my friends for their steadfast support and encouragement throughout this journey. Above all, I offer my praise and gratitude to God, the Creator of the universe, for His guidance and blessings in my life.

https://doi.org/10.7795/110.20250619

Contents

https://doi.org/10.7795/110.20250619

https://doi.org/10.7795/110.20250619

List of Figures

https://doi.org/10.7795/110.20250619

https://doi.org/10.7795/110.20250619

https://doi.org/10.7795/110.20250619

List of Tables

https://doi.org/10.7795/110.20250619

List of Abbreviations

2D	Two dimensional
3D	Three dimensional
AFM	Atomic force microscope
ASTM	American Society for Testing and Materials (former name)
CCM	Consultative Committee for Mass and Related Quantities
CIPM	International Committee for Weights and Measures
CLSM	Confocal laser scanning microscope
CMC	Calibration and Measurement Capability
CM	Confocal microscope
CMM	Coordinate measuring machine
DIN	*Deutsches Institut für Normung* (German Institute for Standardization)
EDK	*Eindringkörper* (german for indenter)
FoV	Field of view
GSM	Group standard method
HBW	Brinell hardness value
H_{IT}	Indentation hardness
HR	Rockwell hardness value
HRTS	High-resolution topographic scanner
HV	Vickers hardness value
IIT	Instrumented indentation testing
ISO	International Organization for Standardization
MEMS	Micro-electromechanical systems
NMI	National Metrology Institute
NMM	Nano measuring and positioning machine
OIML	The International Organization of Legal Metrology
O-P	Oliver and Pharr method
PLC	Programmable logic controller
PTB	Physikalisch-Technische Bundesanstalt
R-h	Radius vs. height

https://doi.org/10.7795/110.20250619

RMS	Root mean square
SI	International system of units
SM	Schwenk’s method
WC	Tungsten Carbide
WGH	Working Group on Hardness

https://doi.org/10.7795/110.20250619

1. Introduction and Motivation

Mechanical characterization of materials is of tremendous importance in the development of a product in any industry. Product designers, engineers and scientists are interested in the mechanical properties of a material to predict the performance of the product during practical application in day-to-day life. Failure to choose the right material affects the reliability, functionality, durability and in some cases safety of the product which could end up in catastrophic consequences.

A manufacturer primarily identifies the loads that would act upon the final product and chooses a material appropriately. Of particular interest are the Young's modulus and the yield stress of a material. The Young's modulus gives information about the stiffness of the material and helps calculate the extent of deformation in the material when a stress is applied. The yield stress is the upper limit of the stress after which the material deforms plastically and does not return to its original shape. Typically, a tension test is performed on the material to obtain these two mechanical properties.

Another popular technique to characterize materials is hardness testing. It is easy to perform, cost-effective, and a near non-destructive method. From the results of this test, a general understanding of the material's elastic and plastic behavior can be gained. Nonetheless, ensuring the accuracy and traceability of a hardness measurement through a metrological chain to the definition of a hardness scale is crucial.

This is where the Physikalisch-Technische Bundesanstalt (PTB), the National Metrology Institute (NMI) of Germany comes into play. The PTB calibrates hardness reference blocks using its primary standard hardness testing machines. These hardness reference blocks are then used by accredited calibration laboratories to calibrate their hardness testing machines. Subsequently, hardness reference blocks calibrated by the accredited laboratories are used by the industry to calibrate their testing machines and thereupon perform reliable hardness measurements.

Besides ensuring the framework for traceability, the PTB takes part in international measurement comparison campaigns. Furthermore, the PTB works alongside other NMIs to improve the definition of the primary standards. Currently, the measurement uncertainty offered by the PTB for the majority of hardness scales is the same as that offered by accredited calibration laboratories. Therefore, it is in the interest of the PTB to improve its measurement technology and to reduce the measurement uncertainty it offers.

The focus of this research is on a particular type of hardness test called the Rockwell hardness test. It is a very popular testing method for metals and is widely used in the industry for quality assurance. However, it poses severe metrological challenges because the existing Rockwell scale is not ideal. The hardness values vary considerably depending upon the type of testing machine used, the geometry of the indenter, or the choice of testing parameters, even if they are within the permitted tolerances in ISO 6508. Over the previous decades, there have been efforts to establish a worldwide

https://doi.org/10.7795/110.20250619

unified Rockwell hardness scale. Despite these efforts, many problems remain unsolved. The aim of this research is the identification and addressing of the critical factors that detrimentally affect a Rockwell hardness test and its overall measurement comparability.

The structure of the dissertation is as follows. Firstly, the theoretical background on hardness is provided in Chapter 2. This contains the history and future, importance, and types of hardness testing methods. Emphasis is laid on the procedure of Rockwell hardness testing and the working mechanisms of the primary standard Rockwell hardness testing machine of the PTB. This is followed by the description of a few surface metrology instruments used to measure the topography of Rockwell hardness diamond indenters. The objectives of the research are elucidated in Chapter 3.

The core work of this research is subdivided into three main chapters. Chapter 4 deals with the definition of a standard testing cycle and the universal automation of a Rockwell hardness testing machine. The different methods available to correct the hardness value based on the deviations in indenter geometry are described in Chapter 5. In Chapter 6, the calibration of the tip radius of a Rockwell diamond indenter is addressed. An affordable and efficient measurement method and a novel method of evaluation are presented. Furthermore, an estimation of measurement uncertainty is undertaken, and the measurement uncertainty budget is presented.

Using the results from Chapter 4, Chapter 5, and Chapter 6, it is possible to reduce the measurement uncertainty in the Rockwell hardness test offered by the PTB. This is demonstrated for the Rockwell hardness scale HRC in Chapter 7. Finally, a summary of this work is provided along with the recommendations for future work in this field.

https://doi.org/10.7795/110.20250619

2. Theoretical Background

2.1. Hardness testing: History, importance, and future

Linguistically, the word hardness is used in a multitude of contexts in daily life. For example, a footballer could gauge the hardness of a football by juggling it with his feet. A task at work can be categorized based on hardness. Hardness is also used to classify water based on the amount of minerals in it. In a negative connotation, one speaks about the hardness of the heart when dealing with an unpleasant person. Thus, every one of us has an innate understanding of hardness.

According to the Cambridge dictionary, hardness is defined as the quality of being firm and solid, and difficult to bend, break, or cut [1]. Metrologically, hardness of a material can be defined as the resistance to local indentation when the surface of the material is pressed by an indenter harder than itself [2].

Oftentimes, a variety of physical and material properties are oversimplified and replaced by the term hardness. This is true for both our daily lives and in the field of engineering and technology, such as in the case of a mechanic, who understands hardness based on the ease of drilling, sawing, or filing [3]. This, however, has led to the development of more than half a dozen standardized methods of measuring hardness based on the needs of the specific era, area of application, and the material being tested.

It is difficult to pinpoint when the first hardness measurement was performed. Hardness testing in a vague sense of tools and weapons has always been happening and can safely be dated back thousands of years. It is ascribed to Democritus and Aristotle to have described hardness as an attribute of the elements. In 1640, Barba used a file to scratch precious stones. After about two centuries, Friedrich Mohs sorted minerals in an increasing order of hardness, giving talc a value of one and diamond a value of ten. Despite the strong nonlinearity in the Mohs scale, it still finds use in mineralogy, especially in assessing the quality of grinding tools [4].

Owing to the growth in the railway sector, a need for testing the hardness of metals emerged. A gradual shift from scratching to indenting can be observed during this time of the second half of the nineteenth century. It is during this time that Adolf Martens put forward his methods for instrumented indentation testing. Shortly after, Johan August Brinell, a Swedish engineer, proposed the ball indentation test [4]. By the twentieth century, hardness testing machines were commercially available [5]. Subsequently, the Rockwell hardness test and Vickers hardness test were introduced in 1920 and 1925 respectively, marking the genesis of the microhardness testing. Since then, the focus has been on standardizing the test methods. The first testing standard on Brinell hardness was published in 1926 in the United States of America. The *Deutsches Insitut für Normung* (DIN) came out with a Vickers test standard in 1940 [4]. A detailed description of the historical origins of indentation hardness testing up until the works of David Tabor in the 1950’s can be found in [5].

https://doi.org/10.7795/110.20250619

Alongside the development and standardization of hardness testing methods, the subject of contact mechanics was also brewing. Heinrich Hertz derived the solution for the deformation of two perfectly elastic spheres in normal contact. This was followed by Boussinesq deriving the analytical solutions for stresses and displacements in an elastic body indented by a rigid indenter that is axisymmetric. Further work by Sneddon on the Boussinesq problem gives us a relation between the load, indentation depth and the contact area for any indenter that can mathematically be described as a solid of revolution of a smooth function [6].

The next breakthrough was the publication of a novel method to evaluate the continuously measured force and displacement signals during an indentation test by W.C. Oliver and G. M. Pharr [7]. The Oliver and Pharr (O-P) method doesn't require optical imaging of indents and can be used to calculate the elastic modulus of materials. The fusion of contact mechanics and the principles of conventional hardness testing has enabled instrumented indentation testing (IIT) to be the future of hardness testing.

IIT has the potential to easily replace most of the conventional hardness testing methods. Most importantly, a plethora of information about the material can be deduced during an indentation test and not just the hardness. Some of these material properties are yield stress, time-dependent plasticity, fracture toughness, stress-strain curves, and elastic and plastic energies. Perhaps the greatest advantage of this technique is the probing of the material surface and mapping its properties on a spatially resolved basis. Furthermore, it is one of the few methods that can be used to measure the mechanical properties of small volumes or isolated phases, such as the alpha and beta phases, depending on the grain size [8]. Due to the great strides in the development of IIT in the past decades, it has even established itself in the fields of geology, biology, forestry, and medicine. However, it is most often used in the fields of miniature components, such as coatings, sensors, micro-electromechanical systems (MEMS), and nanopillars [9].

Although IIT is the undisputed future of hardness testing, conventional hardness testing methods are still very much around. The industry heavily relies upon these methods, and it is extremely unlikely that it will get replaced anytime in the coming years. A small indicator for this is the number of calibrations undertaken by the working group for hardness metrology at the PTB. Regular calibration requests for Rockwell hardness testing, Brinell hardness testing, and Vickers hardness testing are received, whereas the calibration requests for IIT in comparison to them are negligible.

The trends in material testing also indicate a rise in the use of portable hardness testing devices. These devices can be used outside a laboratory and offer a quick hardness test result. Nonetheless, the accuracy and reliability of these devices lag far behind that of a conventional laboratory-based hardness test [10, 11].

https://doi.org/10.7795/110.20250619

2.2. Types of hardness measurements

There are different ways in which the various types of hardness tests can be classified. A few of them are:

- Deformation mechanism such as indenting, scratching, bending, etc. [12]
- Nature of test: destructive or nondestructive
- Static testing and dynamic testing [13]
- Standardized and unstandardized tests
- Classification based on the applied load or resulting indentation depth, such as macro, micro, or nano hardness.

Every hardness test has its own set of advantages and disadvantages. Depending on the field of application, an appropriate hardness test must be chosen [14]. In this section, the Brinell hardness test, Vickers hardness test and instrumented indentation testing are briefly described.

2.2.1. Brinell hardness test

This is a static indentation test that uses a spherical indenter made of hard metal to exert a force on the specimen. After the removal of the test force, the averaged diameter of the resulting indent is used to calculate the Brinell hardness value. A sketch of the test procedure is shown in Figure 1.

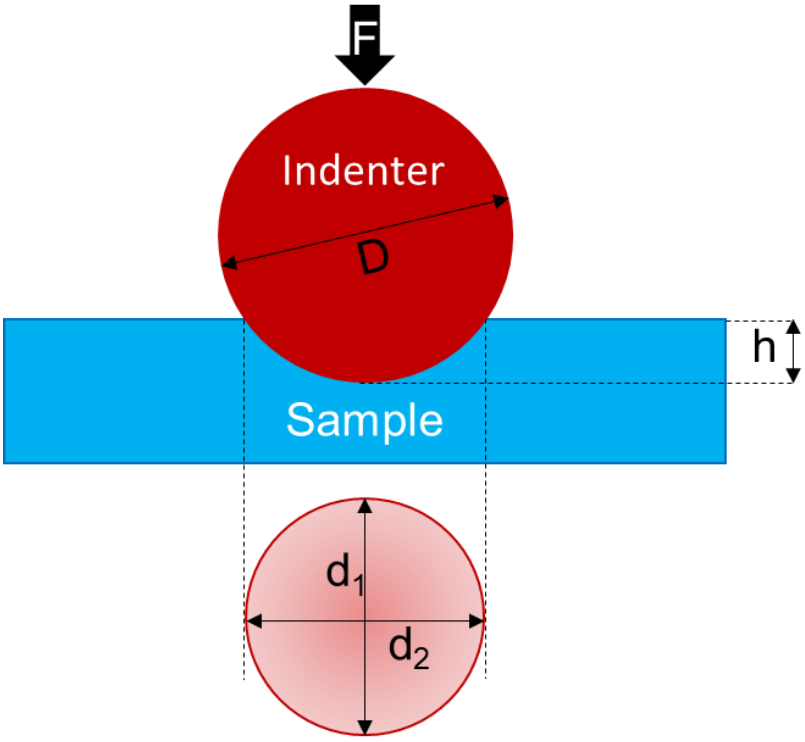

Figure 1: Schematic representation of a Brinell hardness test

https://doi.org/10.7795/110.20250619

The Brinell hardness value (HBW) is defined as the ratio of the applied force to the surface area of the indentation and can be determined using Equation 1.

$$HBW = \frac{0.102 \cdot 2 \cdot F}{\pi D\left(D - \sqrt{D^2 - d^2}\right)} \quad \textbf{Equation 1}$$

where:

F is the test force in newtons,

D is the diameter of the indenter in mm and

d is the mean of the indent diameters d_1 and d_2 in mm.

The testing procedure is standardized [15] and the test force along with the diameter of the indenter used to measure the Brinell hardness value must be mentioned alongside the measured hardness value.

2.2.2. Vickers hardness test

This test also belongs to the static indentation test category. A four-sided pyramid made of diamond with a face angle of 68° is used as an indenter. Similar to the Brinell hardness test, the indenter is pressed into the specimen with a test force. The arithmetic mean of the diagonals of the indent, which are measured after the removal of the test force, is used in Equation 2 and forms the basis of the calculated Vickers hardness value (HV). The diagonals are typically measured using an optical microscope.

$$HV = \frac{0.102 \cdot 2 \cdot F \cdot \sin\left(\frac{136°}{2}\right)}{d^2} \quad \textbf{Equation 2}$$

where:

F is the test force in newtons and

d is the mean of the diagonals d_1 and d_2 in mm.

A sketch depicting the test procedure is shown in Figure 2. The ISO standard [16] regulates the testing parameters such as minimum sample thickness, force application rate, and permissible length of indent diagonals. The development of the Vickers hardness test is attributed to the need for testing heat-treated metals [17]. The main advantage of Vickers hardness test over Brinell hardness test is the independence of the indenter size in the calculation of the hardness value. Moreover, the use of a diamond indenter in comparison to the hard metal spheres ensures that the shape of the indenter remains nearly intact over a prolonged period.

https://doi.org/10.7795/110.20250619

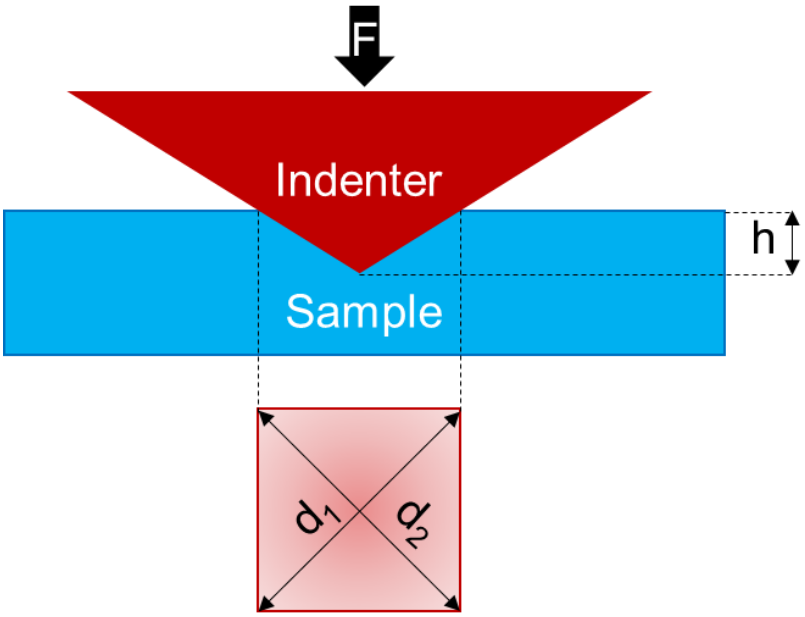

Figure 2: Schematic representation of a Vickers hardness test

2.2.3. Instrumented indentation test

The specialty of IIT with which it distinguishes itself from other types of hardness testing is the continuous measurement of the force and displacement signals during an indentation process [18]. Additionally, the imaging and measurement of the indent after the unloading of the specimen is circumvented by using an indenter whose geometric properties are accurately known [19]. Typically, IIT deals with forces in nanonewtons and displacements in the range of nanometers. Hence it is also called nanoindentation [20].

Analyzing the force vs. indentation depth data obtained from an IIT reveals the type of material that is being tested. Three distinct material responses are shown in Figure 3. Curve 1 represents a perfectly elastic material. As the applied force increases, the indentation depth increases, whereas during unloading, the curve retraces the loading path. On the other hand, no elastic recovery during the unloading phase is observed in curve 3, which implies that the material is perfectly plastic. Generally, most materials lie between these two extreme responses (see curve 2) and exhibit both elastic recovery and permanent plastic deformation. Other material responses, such as creep behavior or pressure-induced phase changes, can also be observed in the force vs. indentation depth curves [21]. The slope of the initial portion of the unloading curve is used to extract the indentation modulus of the material [22].

The hardness obtained from IIT is called indentation hardness, and it is expressed using the unit pascal. It is defined as the ratio of the maximum applied force to the projected contact area between the indenter and sample. Naturally, the projected contact area varies based on the choice of the indenter and its real geometry. A diamond indenter called the Berkovich indenter is the most widely used indenter in IIT [23]. It is

https://doi.org/10.7795/110.20250619

a three-sided pyramid with a face angle of 65.27°. Other indenters that are commonly used in IIT are Vickers indenters, spherical indenters, conical indenters, etc.

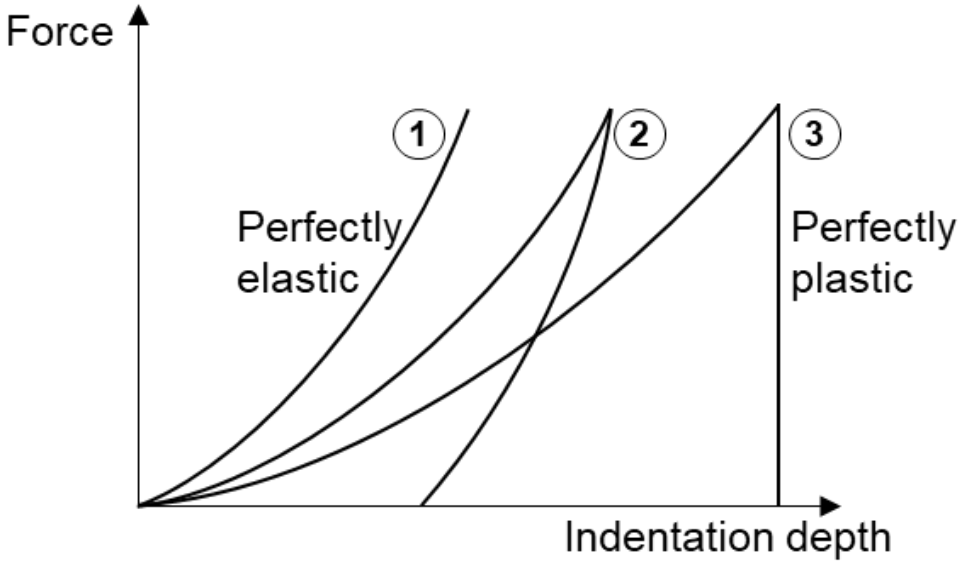

Figure 3: Force vs. indentation depth curves for three types of materials obtained by performing instrumented indentation tests

Assuming an ideal Berkovich indenter is used, the indentation hardness (H_{IT}) is given by the Equation 3.

$$H_{IT} = \frac{F_{max}}{24.49 \cdot h_c^2} \qquad \textbf{Equation 3}$$

where:

F_{max} is the maximum test force and

h_c is the contact depth.

The ISO standard [24] stipulates that the Equation 3 can only be used if the contact depth exceeds 6 µm. When this is not the case, a tip area calibration to determine the area with respect to the height (area function) must be performed to account for tip rounding and other indenter shape deviations. Furthermore, the part of the measured indentation depth that is associated with the deformation of the measuring instrument during a measurement must be isolated. This is known as load frame stiffness calibration. Both of these calibrations can be performed with one set of measurements at different loads by using fused quartz as a reference material. Given its isotropic nature and since it does not exhibit appreciable pile-up or sink-in during an indentation process, it is ubiquitously used as a standard reference material in IIT [25].

https://doi.org/10.7795/110.20250619

Other factors, such as thermal drift, point of first contact, and surface roughness of the sample, must also be considered before interpreting the measurement results of IIT.

2.3. Rockwell hardness test

Since the focus of this work is on Rockwell hardness testing, it is elaborated here in detail. The hardness testing methods that existed prior to Rockwell hardness testing, such as Brinell and Vickers hardness tests, needed a microscope to measure the indent diameter or diagonal, respectively. Keeping up with the high demand and the need for simplifying hardness testing, the brothers H. M. Rockwell and S. P. Rockwell filed an application to patent their hardness tester in 1914 [26]. This hardness tester used a straightforward dial indicator to display the hardness number, which reduced the overall time of a hardness test. This was followed by the patenting of a diamond conical indenter which enabled the testing of very hard metals [27]. The popularity of this method soared during the Second World War and continues to be among the most popular material testing methods to this day [28, 29].

2.3.1. Test procedure and scales

To perform a Rockwell hardness test, an indenter is pressed into a material, whose hardness is to be measured. The force is increased until the preliminary force F_0 is experienced by the material. The preliminary force serves as a depth reference and reduces the effect the testing machine has on the hardness test. This force is held constant for a certain amount of time before measuring the indentation depth. Subsequently, a larger force called the additional force F_1 is applied at a set rate until the total force F is reached. The total force is held for a certain amount of time before the additional force is withdrawn. At the preliminary load, the indentation depth is measured once again after a certain dwell time. Finally, the indenter is separated from the material completely. The difference between the measured indentation depths serves as the basis of the Rockwell hardness value. A schematic has been provided in Figure 4.

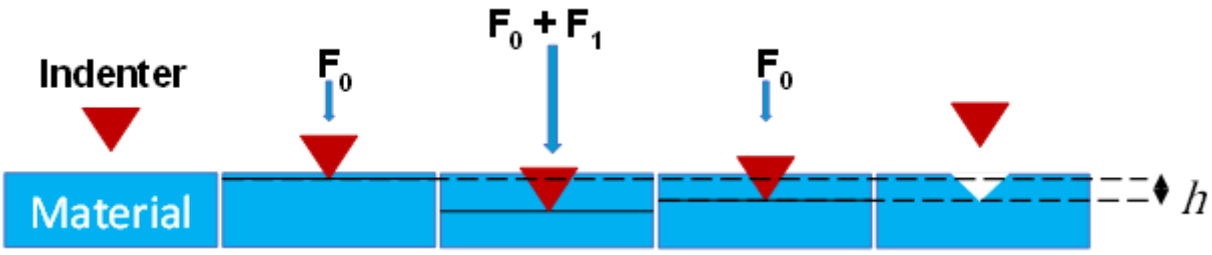

Figure 4: Schematic representation of a Rockwell hardness test

Based on the material being tested, around 30 scales of Rockwell hardness can be chosen. They are broadly categorized into two types: regular Rockwell and superficial Rockwell. The regular scales apply higher loads, whereas the superficial scales utilize

https://doi.org/10.7795/110.20250619

lighter loads and hence are used for testing thinner materials. The various scales differ in terms of indenter type, preliminary force, total test force, and the calculation of the hardness value.

For most of the Rockwell hardness scales, balls of varying diameters are used as indenters. Historically, the use of hardened steel balls was prevalent. Due to the flattening of the steel ball indenters with progressive usage and the subsequent variation in the Rockwell hardness values that arise from the shape deviation of the indenter, they have now been replaced by tungsten carbide (WC) composite balls as the new standard [30, 31]. The material of the ball indenter used to perform a hardness test is mentioned at the end of the hardness value as initials (WC or s for steel). Some scales use conical diamond indenters with a spherical tip, which are also known as Brale indenters. The preliminary test force is 98.07 N or 10 kgf for the regular Rockwell scale, whereas 29.42 N or 3 kgf for the superficial Rockwell scale.

Every scale has its typical application. For example, the superficial scale N is used for testing case hardened materials, whereas the superficial scale T is used for testing soft coatings. The regular Rockwell scale C is the most popular scale, abbreviated as HRC, and is used to test steel and hard cast irons [32, 33]. A consolidated overview of the Rockwell scales classified based on the indenter type and the total test force is presented in Table 1.

Regular Rockwell hardness scale					
Indenter / Total test force	Diamond cone	Ball of diameter 1.5875 mm	Ball of diameter 3.175 mm	Ball of diameter 6.35 mm	Ball of diameter 12.7 mm
F = 1471 N	C	G	K	P	V
F = 980.7 N	D	B	E	M	S
F = 588.4 N	A	F	H	L	R
Superficial Rockwell hardness scale					
F = 441.3 N	45N	45T	45W	45X	45Y
F = 294.2 N	30N	30T	30W	30X	30Y
F = 147.1 N	15N	15T	15W	15X	15Y

Table 1: Classification of regular and superficial Rockwell hardness scales with respect to the total test force and the type of indenter used

https://doi.org/10.7795/110.20250619

After choosing an appropriate scale and performing a hardness test, the Rockwell hardness value (HR) can be calculated using the Equation 4.

$$HR = N - \frac{h}{S} \quad \textbf{Equation 4}$$

where:

N and *S* are scale dependent constants and

h is the difference between the measured depths of indentation at the preliminary test force and after the removal of the additional test force, as indicated in the Figure 4.

The values of the constants *N* and *S* have been tabulated in Table 2.

Rockwell hardness scale	Value of constant *N*	Value of constant *S*
A, D, C	100	2 µm
B, E, F, G, H, K	130	2 µm
N, T (superficial)	100	1 µm

Table 2: Values of the scale dependent constants for the calculation of the Rockwell hardness value

The value of the constant *N* is indicative of the largest possible Rockwell hardness value in the respective scale, and the constant *S* divides the Rockwell scale into the required resolution. Assuming a material is tested for the Rockwell scale C and a value of *h* = 100 µm is measured, the Rockwell hardness value is reported as 50 HRC.

2.3.2. Standards

Since the evolution of the Rockwell hardness test from a simple quality check to a metrological tool, the need for standardization arose. In North America, ASTM standards are followed. In the rest of the world, ISO standards are prevalent. OIML, the International Organization for Legal Metrology, regularly publishes recommendations to guide countries in legal matters [34]. Furthermore, the Working Group on Hardness of the Consultative Committee for Mass and Related Quantities (CCM-WGH) under the International Committee for Weights and Measures (CIPM) constantly works to improve the harmonization of primary standards by developing and publishing new primary definitions [35]. In this work, the ISO standard 6508 is used [36].

The ISO 6508 under the common heading of Rockwell hardness test for metallic materials consists of three parts. The first part deals with the testing method [36], whereas

https://doi.org/10.7795/110.20250619

the second part details the verification and calibration of testing machines and indenters [37]. The third part specifies a method to calibrate hardness reference blocks that are used to perform a direct or indirect verification of testing machines [38], as specified in the second part.

2.3.3. Stages of a Rockwell hardness test

To perform a standard-compliant Rockwell hardness test, certain testing parameters need to be adhered to. Considering the test sample to be a hardness reference block and the measurement to be a calibration, the third part of the ISO 6508 standard must be complied with. The pertaining testing parameters are described in this subsection with the help of force vs. time (see Figure 5) and indentation depth vs. time (see Figure 6) diagrams for a regular Rockwell scale. It must be pointed out that the relation between force and indentation depth with respect to time is illustrated using straight lines. In practice, it is only possible to control either the loading rate or the indentation speed, which in turn varies the other.

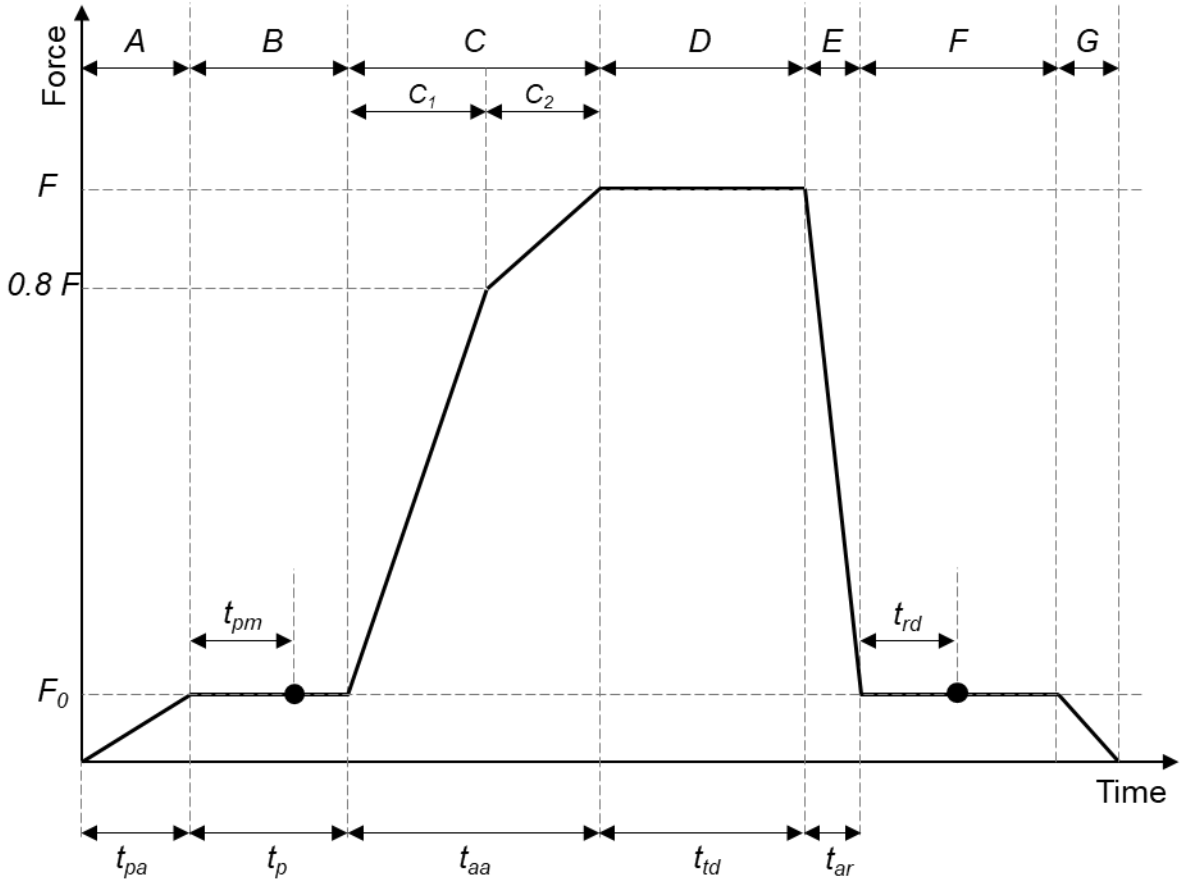

Figure 5: Force vs. time diagram of a regular Rockwell hardness test according to the third part of the ISO 6508

https://doi.org/10.7795/110.20250619

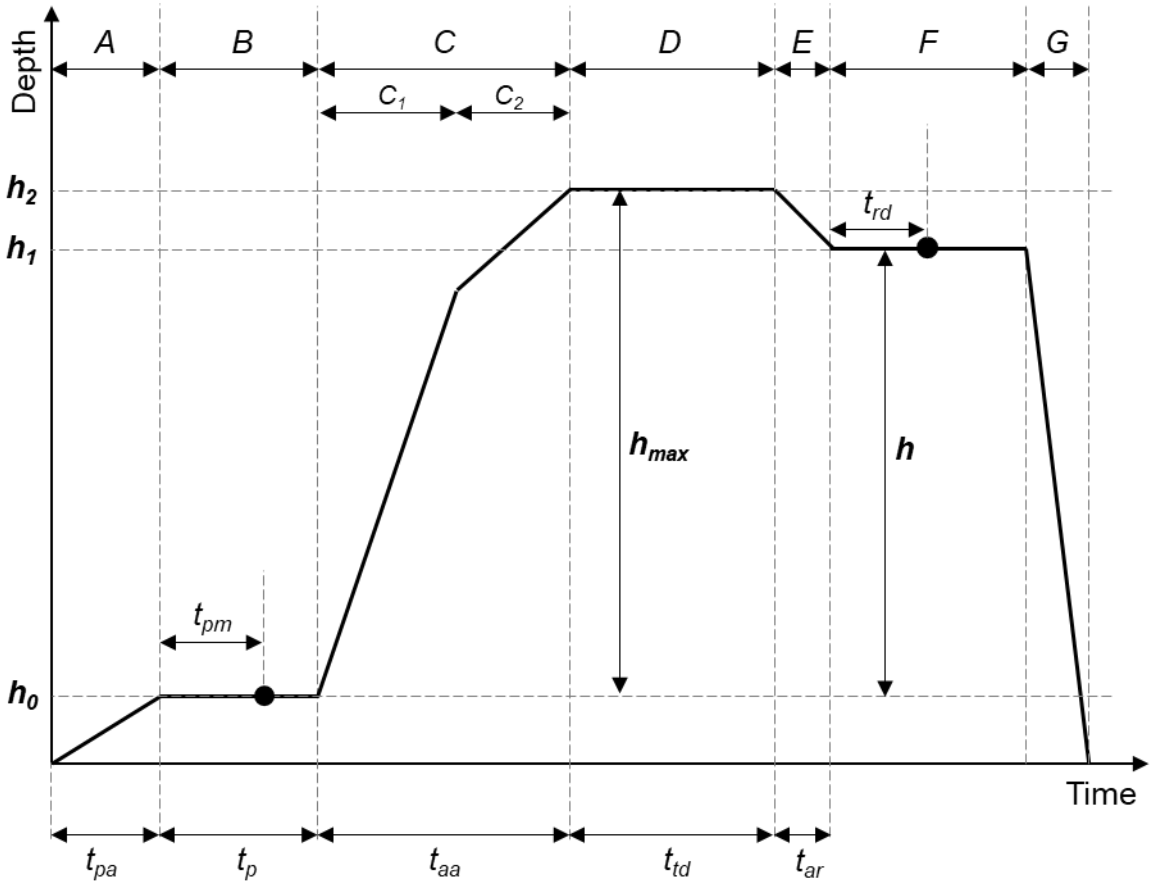

Figure 6: Indentation depth vs. time diagram of a regular Rockwell hardness test according to the third part of the ISO 6508

Firstly, it must be ensured that the calibration takes place at a temperature of (23 ± 5) °C and that the thermal drift during the calibration is maintained below 1 °C. At the start of the calibration, the indenter begins to move towards the surface of the hardness reference block. During the initial contact between the indenter and the surface, the indenter speed must be below 1 mm/s.

The testing cycle commences with the stage A after the initial contact at time t = 0 s. During this stage, the preliminary test force F_0 is applied without generating any shock, vibration, or oscillation and within an application time t_{pa} of 2 s. By the end of stage A, it must be seen that no overshooting of the test force occurs.

In Stage B, the complete preliminary test force acts on the hardness reference block. This force is maintained for a duration t_p of (3 ± 1) s. The duration of time t_{pm} before the initial measurement of the indentation depth h_0 is given by the Equation 5.

$$t_{pm} = t_p - \frac{t_{pa}}{2} \qquad \textbf{Equation 5}$$

https://doi.org/10.7795/110.20250619

The additional test force F_1 is applied in the stage C. The time duration for the application of this force t_{aa} is given as 7^{+1}_{-6} s. This means that the permissible range of t_{aa} is between 1 s and 8 s, with 7 s being the most desirable application time.

One major difference in the measurement procedure between the first and third parts of the ISO 6508 is the subdivision of stage C. The third part of the ISO 6508 requires that the indentation speed be set between 15 µm/s and 40 µm/s after 80 % of the total test force F is acting on the material (stage C_2). This indentation speed v_2 must be held constant until 99 % of the total test force F is exerted on the material. The indentation speed in stage C_1 is denoted by v_1.

The total test force F, which is the sum of the preliminary test force F_0 and the additional test force F_1, acts on the hardness reference block at the start of the stage D. It must once again be ensured that no undesired outcomes due to sudden loading are experienced by the material, especially the overshooting of the test force. The dwell time for the total test force t_{td} is (5 ± 1) s. Although the measurement of the indentation depth at the total test force is not relevant for the calculation of the Rockwell hardness value, it is nevertheless denoted in this work by h_2. Likewise, h_{max} is the indentation depth that corresponds to the deformation caused by the application of the additional test force F_1.

The unloading phase of a Rockwell hardness test begins with the stage E. The additional test force F_1 is removed while the preliminary test force F_0 continues to act on the hardness reference block. Before measuring the indentation depth h_1 in the stage F, a hold time t_{rd} of (4 ± 1) s is observed. Finally, in stage G, the preliminary test force F_0 is withdrawn, and the indenter separates from the surface marking the end of the measurement. The permanent depth of indentation h, which is used to calculate the Rockwell hardness value, is given by the Equation 6.

$$h = h_1 - h_0 \qquad \textbf{Equation 6}$$

A minimum of five measurements that are uniformly spread across the test surface must be performed to calibrate a hardness reference block. The hardness value of the reference block is the arithmetic mean of the hardness values of the individual indentations.

2.3.4. Testing machine

In addition to defining the loading rates and dwell times, the standard also requires the testing machine to be directly verified periodically, at least once a year. This involves the calibration of the test force [39], the depth measuring system [40], the testing cycle, and the machine hysteresis test. While undertaking the direct verification, it is checked if the aforementioned parameters lie within the specified tolerances. Subsequently, an

https://doi.org/10.7795/110.20250619

indirect verification using multiple hardness reference blocks is to be performed to ascertain the hardness measuring capability of a machine. Nonetheless, the overall performance of a Rockwell hardness testing machine is contingent not just on its calibrated state but also its make. Some machines are inherently better than the others [41].

Rockwell hardness testing machines can be broadly classified based on the following:

Classification based on loading mechanism:

The generation of the required force to perform a Rockwell hardness test can be realized in many ways. The first types of machines used compressed helical springs and dead-weights along with a force multiplying lever system to apply the preliminary test force and the additional test force, respectively [34]. Dead-weights generate force by virtue of the weight of the mass blocks in the gravitational field of the earth. The loading rate was controlled by hydraulic dashpots. The advantage of such a loading mechanism is the ease and inexpensive cost of manufacturing. The primary drawback is the problem associated with the transmission of the force of the dead-weight using force multipliers onto the small sized indenter. Furthermore, dead-weight systems cannot be modified easily to accommodate the changes in the standard requirements, such as a change in the force levels.

Newer machines use electric motors, actuators or moving spindles to generate the necessary forces. A recent advancement is the use of closed-loop systems to monitor the force during a hardness test. Load-cells are used along with a feedback mechanism, which enables the control of the entire test cycle. Additionally, these systems are much more flexible to change. Although the use of such systems eliminates the errors originating from the mechanical components, it gives rise to newer sources of errors relating to the electronics, such as the unavoidable oscillation of the force at any set value.

Classification based on indentation depth measurement:

Bearing in mind that an error of 1 µm in the measurement of the permanent depth of indentation in an HRC scale leads to an error of 0.5 HRC units, it is key to measure the indentation depth accurately and precisely to obtain the correct Rockwell hardness value. Classically, dial gauges that use a rack and pinion gear to mechanically measure the displacement have been used. The Rockwell hardness value corresponding to the measured displacement is indicated on the analog display. Besides the large resolution, the other drawbacks of a dial gauge that affect the measurement results are the wear and tear of the mechanical parts, misalignment errors, and the unwanted alteration of the applied force due to the physical contact between the indenter and the probe of the dial gauge. Other ways to measure the indentation depth are using inductive or capacitive sensors, or optically through microscopes, laser hologauges, graduated scales, or most importantly, laser interferometers.

Classification based on machine frame:

https://doi.org/10.7795/110.20250619

The two main types of machine frames typically used in Rockwell hardness testing are the C-shaped machine frame and the rigid machine frame. Due to its compact size and ease of installation and maintenance, the C-shaped machine frame finds widespread usage in the industry. The closed symmetric rigid frames, on the other hand, are generally used by NMIs as standardizing machines.

Classification based on mode of operation:

The mode of operation of a Rockwell hardness testing machine can be manual, semi-automatic, or fully automatic. Manual operation is where the operator has complete autonomy over the testing cycle. Needless to say, a fully automatic mode of operation helps eliminate the errors that are innate to humans, such as parallax errors or time-keeping.

2.3.5. Primary hardness testing standard

The hardness testing machine used by the PTB as the primary hardness testing standard for the regular Rockwell scale is shown in Figure 7. It is a closed symmetric machine with a rigid frame and is hence less susceptible to deformation during measurement. A similar machine is used for the super Rockwell scale. Since the loading mechanism uses dead-weights to apply the necessary test forces, and given the differences in the preliminary test forces of the regular and superficial scales, different testing machines must be used. Similarly, due to the different stages in the loading of Rockwell hardness testing, the primary hardness testing standards for Vickers and Brinell hardness tests are performed on a different machine. The need to use multiple hardness testing machines for different types of hardness testing methods is a disadvantage of a dead-weight system. Nevertheless, dead-weight systems offer the lowest level of measurement uncertainty for the test forces, which is extremely desirable for calibrations performed by an NMI.

The machine consists of two yokes. The mass of the upper yoke along with the indenter and its components equates to the required preliminary test force. The lower yoke along with the dead-weights has a mass that equates to the additional test force. Depending on the choice of the Rockwell scale, the dead-weights must either be connected or disconnected from the lower yoke. The combination of the masses of both the yokes is responsible for generating the total test force. Previously, hydraulic systems were used to actuate the yokes. This has now been replaced by a servomotor.

The material to be tested is placed on the rigid worktable and clamped into position using a sample down-holder. This inhibits the movement of the material in the lateral direction. The worktable is fastened to the machine frame, and its top surface is polished flat. Depending on the thickness of the material being tested, different heights of the worktable are available.

The monitoring of the load application is undertaken using a load cell, which is mounted on the machine frame. Due to its location in the machine, the load cell experiences the

https://doi.org/10.7795/110.20250619

total test force when there is no contact between the indenter and the material. Conversely, when the total test force acts on the material, the load cell experiences no force. The calibration of the load cell based on the chosen Rockwell scale is carried out by performing a trial run using the appropriate dead-weights.

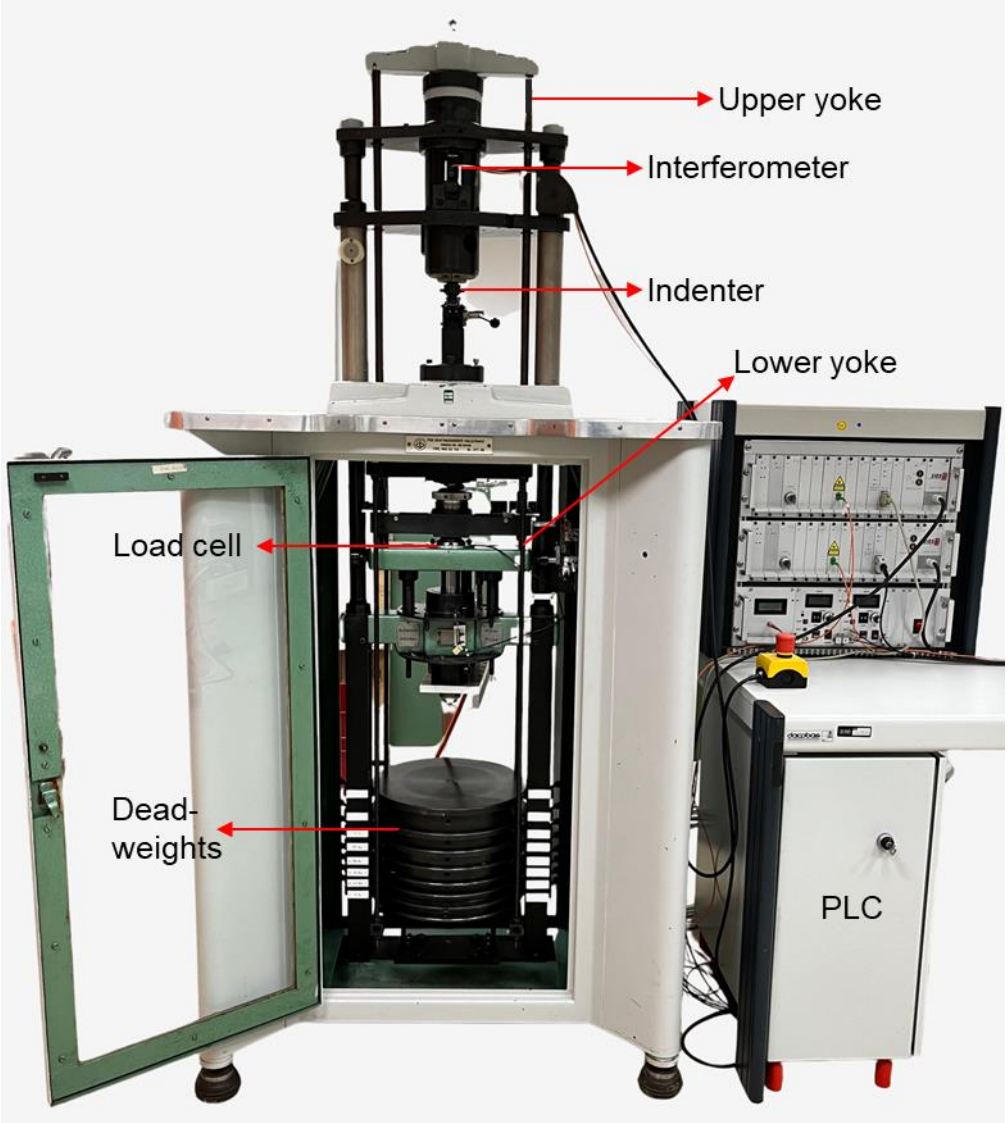

Figure 7: Image of the primary hardness testing standard of the PTB for regular Rockwell scales

In the parking position of the machine, both the yokes are supported by the machine frame on the ram, whereas the dead-weights are secured onto the weight support. Actuating the linear ram transfers the preliminary test force from the ram to the indenter via the coil spring, eventually causing the indentation in the material. Further actuation transfers the additional test force to the upper yoke through another coil spring. An upper and lower limit switch is installed in the system to contain the motion of the yokes. During the entire process, the indenter moves only along the vertical axis due to the guidance system.

https://doi.org/10.7795/110.20250619

The measurement of the indentation depth is performed using a laser interferometer. It is a contactless method that does not interfere with the force application system and offers nanometer resolution. Traceability to the SI unit meter is achieved by using a frequency-stabilized HeNe laser, whose wavelength is known with a relative uncertainty of approximately 3 x 10^{-6} [104, 105]. The movement of the indenter during a measurement is measured, which enables the determination of the indentation depth and indentation velocity.

The operation of the machine is automated using an industrial computer and a programmable logic controller (PLC). An ethernet-based fieldbus system is used to communicate between all the input and output devices. A graphical user interface assists the user to select the Rockwell scale and perform a hardness test. It also visualizes the force, displacement, and time measurements in real-time.

2.4. Measurement of indenter geometry

This section serves as an introduction to the measurement devices that have been used to measure the geometric properties of indenters and the topography of indents in this work. The calibration and verification of the indenter geometry are requirements put forth by the standards. The standards define the geometric shape of the indenter and dictate the permissible tolerances for the indenter's geometry. They also generally define the material that the indenter should be made of and the mechanical properties that it should possess. Furthermore, the temperature at which the calibration must take place as well as the frequency of the verification and calibration are detailed in the standards.

In some cases, the standard restricts the use of certain measuring instruments to characterize an indenter based on the measurement uncertainty. For instance, in Rockwell hardness testing, the standard [37] states that the measuring instrument used to measure the geometric properties of an indenter must have an expanded measurement uncertainty with a confidence level of 95 % under 0.1° and 5 µm for the angle and radius respectively and that the measuring instrument must be traceable to the national standards. However, the standard does not exclude any measuring instrument based on its working principle. Nevertheless, before choosing a measuring instrument it is imperative to take into consideration the accuracy and precision of the measuring instrument, resolution of the instrument, measurement speed and other influencing parameters that could affect the calibration result. It is equally important for the measuring instrument to be able to seat the indenter in place and measure it without physical barriers obstructing the measurement.

Broadly speaking, the working principle of measuring instruments can be classified into tactile or optical methods. Tactile methods are generally very time-consuming and require additional post-processing steps on the acquired raw data to obtain the true 3D surface of an object. Per contra, an optical measurement is quick and uncomplicated. Moreover, it is a non-contact measurement method that does not alter the surface of

https://doi.org/10.7795/110.20250619

the object in any fashion. The major shortcoming of optical methods is the establishment of a traceability chain. Therefore, tactile methods are considered as reference measurements in this work.

2.4.1. Tactile methods

The first type of measuring instrument used to characterize the geometry of the indenter is shown in Figure 8 and is called the high-resolution topographic scanner (HRTS) [42]. It is a tactile profilometer designed and realized at the PTB for the purpose of calibrating roughness standards. The HRTS consists of a low-noise air suspended table, whose position and motion along the axes are measured within an absolute deviation of 10 nm by optical linear encoders (LIP 281 R). The measurement head is a linearly guided stylus, whose motion along the z-axis is measured by an interferometer.

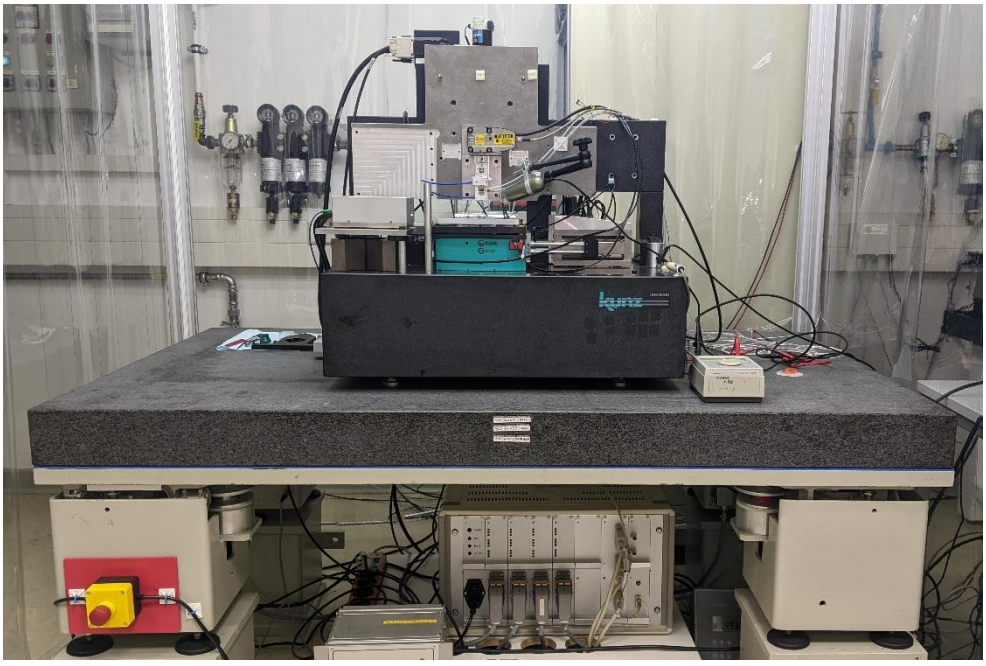

Figure 8: Image of the HRTS (Photo credit: Jürgen Kirchhoff)

The tip of the stylus is made of diamond and has a mean radius of 1.629 µm ± 0.040 µm and an opening angle of 60°. From the Figure 9, which shows the stylus tip in contact with the indenter, it is clear that the opening angle of the stylus tip is notably smaller than the opening angle of the indenter. This ensures that only the spherical part of the stylus tip probes the entire indenter and not its conical part. The contact force between the stylus tip and the sample is controlled and set at 150 µN. The instrument is isolated from the environment in a fully climatic room, where the temperature is controlled between 20 °C ± 0.1 °C. Furthermore, the environmental factors are measured every 30 s during a measurement. In case any significant disturbance is monitored, the measurement is aborted and repeated after addressing the problem.

https://doi.org/10.7795/110.20250619

With the HRTS, the radius and the opening angle of an indenter can be measured with an expanded measurement uncertainty lower than 0.1 µm and 0.01°, respectively. This fulfills the criteria set by the standard [37] on measuring instruments used to characterize indenters by a large margin. The geometry of the indenter is linearly scanned with single profiles along the x-axis with a frequency of 1 kHz. The y-axis functions as an infeed axis. The feed rate amounts to 40 µm s^{-1}. Considering a square shaped scan of length 1000 µm with 5000 profiles and 0.2 µm between the profiles amounts to a total measurement time of approximately 91 hours on an indenter. Due to the lengthy duration of measurement, it is necessary to check for thermal drifts. This is carried out by performing a second measurement on the same indenter with 200 profiles along the y-axis symmetric to the indenter tip with a profile distance of 0.2 µm on the same coordinate system. After the evaluation, it is concluded that no thermal drift correction is required for any of the measurements presented in this work.

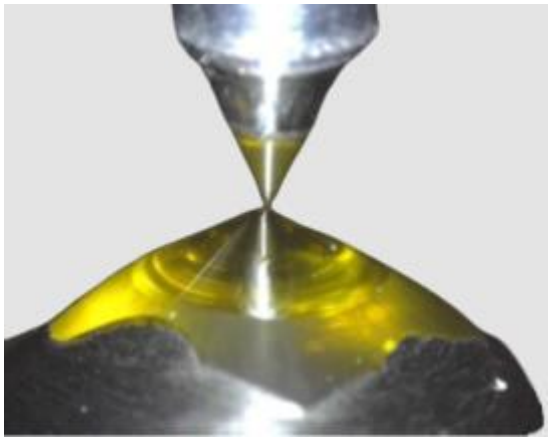

Figure 9: Stylus tip of the HRTS probing a Rockwell hardness diamond indenter (Photo credit: Peter Thomsen-Schmidt)

The evaluation of the measurement results, such as the calculation of the area function and extraction of parameters from individual profiles, is undertaken with the help of the software LabView. During the evaluation, the number of measurement points per profile is reduced from 25000 to 5000 equidistant points. Thus, a mesh of 5000 × 5000 profile points is available for the purpose of visualization and analysis.

Individual profiles are then filtered using a spline function with an adjusted cut-off wavelength of 1.4 µm for noise suppression. Subsequently, a vectorial algorithm is used to calculate the total area of the indenter by summing up the infinitesimal area elements as a function of the distance from the highest point on the indenter. In this way, the area is calculated for incremental heights of the indenter. Similarly, the program can determine the respective cross-sectional area of the indenter as a function of the height from the projection in the xy-plane. The instrument is capable of measuring objects up to a depth of 450 µm.

https://doi.org/10.7795/110.20250619

The second type of tactile instrument that is utilized in this work is based on the nano measuring and positioning machine (NMM). It is a versatile instrument that can incorporate a diamond stylus probe, a focus sensor, a regular atomic force microscope (AFM) probe, or an assembled cantilever probe as a sensor head to perform various kinds of dimensional measurements. The natural choice when measuring the geometric properties of indenters is a diamond stylus probe. Due to the height of the indenter, using an AFM probe for a measurement would result in undesirable contact between the cantilever of the AFM and the indenter. To obtain the topography of an object, it is mounted on the motion platform of the instrument and moved in a predetermined fashion. The stylus probe is held in position at the intersection between three laser beams, thus reducing the Abbe offset. The use of interferometers gives this instrument a resolution of 0.08 nm. A measurement range of 25 mm in the x and y axes, whereas 5 mm along the z-axis (height axis) is realizable. After the conclusion of the measurement, the obtained raw data is eroded to eliminate the dilation effects of the stylus probe [43, 44].

The final type of measuring instrument discussed here is the coordinate measuring machine (CMM). As the name suggests, CMM is used to measure the spatial coordinates of an object by moving a probing system over it. The CMM that is used to provide reference measurements in this work is a 3D micro-CMM that uses a tactile spherical microprobe of diameter 150 µm or 300 µm. It offers an insulated measurement chamber for a temperature-controlled measurement. Measurements can be performed in a scanning or a single point mode for a measurement range of 130 mm x 130 mm x 100 mm in x, y, and z axis respectively [45, 46].

2.4.2. Optical methods

The general concept of the extraction of the surface topography of an object using optical methods is similar to that of a tactile method. Instead of using a stylus tip, a source of light is projected and scanned over the surface. The main advantage of an optical method over a tactile method is the non-contact nature of measurement. This not only reduces the measurement time, but it also eliminates the likelihood of damaging the object being measured. The main disadvantage is the complexity of the phenomenon of the interaction of the light beam with the surface, which makes it necessary to separate the geometric or material properties of the surface to be measured from the measurement itself.

There are many types of optical instruments that can be used for the extraction of the indenter topography, such as confocal microscopes (CM), white light interference microscopes, phase shifting interference microscopes, and focus variation microscopes. In this work, a confocal laser scanning microscope (CLSM) is predominantly used. A CLSM collimates light obtained from a monochromatic source through a pinhole aperture. The collimated light is deflected by a dichroic beam splitter in the direction of the object’s surface. The light is focused on a small part of the surface using a lens system.

https://doi.org/10.7795/110.20250619

By means of a movable mirror and lens system, the entire surface is scanned accordingly. The reflected light from each scan passes through the dichroic mirror and finally lands on the photodetector. An additional pinhole prevents stray reflected light from the object's surface from reaching the detector [47]. Thus, only the in-focus image is captured. Figure 10 presents a sketch of the working principle of a CLSM.

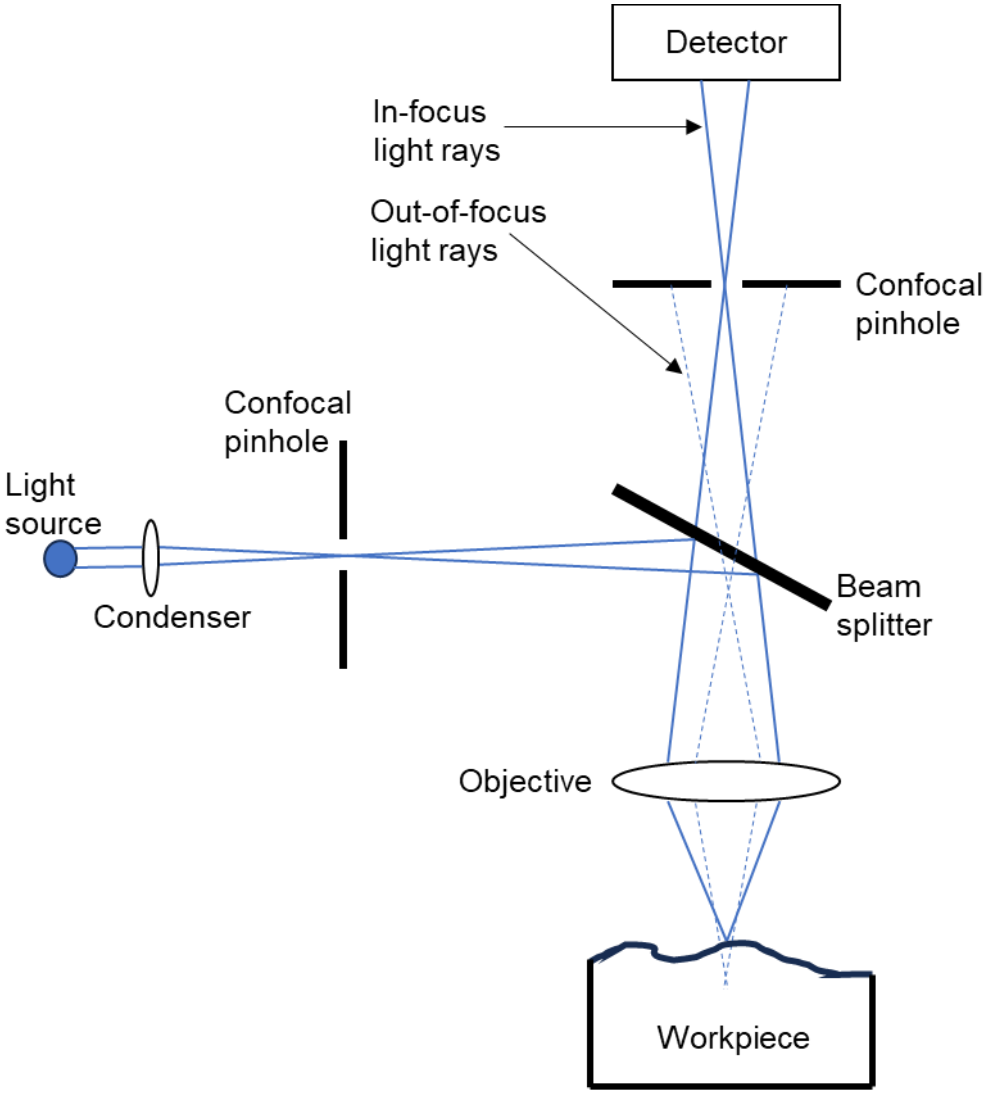

Figure 10: Working principle of a confocal microscope

A CLSM is a special type of CM that specifically uses laser illumination as a light source and also possesses advanced scanning capabilities. The other types of CM used in this study are spinning disk CM and structured illumination CM. A spinning disk CM utilizes a spinning disk with multiple pinholes to scan the surface, whereas a structured illumination CM projects structured light patterns onto a surface to improve image resolution [47].

https://doi.org/10.7795/110.20250619

3. Objectives

The deviation between a measured Rockwell hardness value and a true Rockwell hardness value of a material can be caused by a multitude of factors. A broad classification of the factors is depicted in Figure 11 using an Ishikawa fishbone diagram.

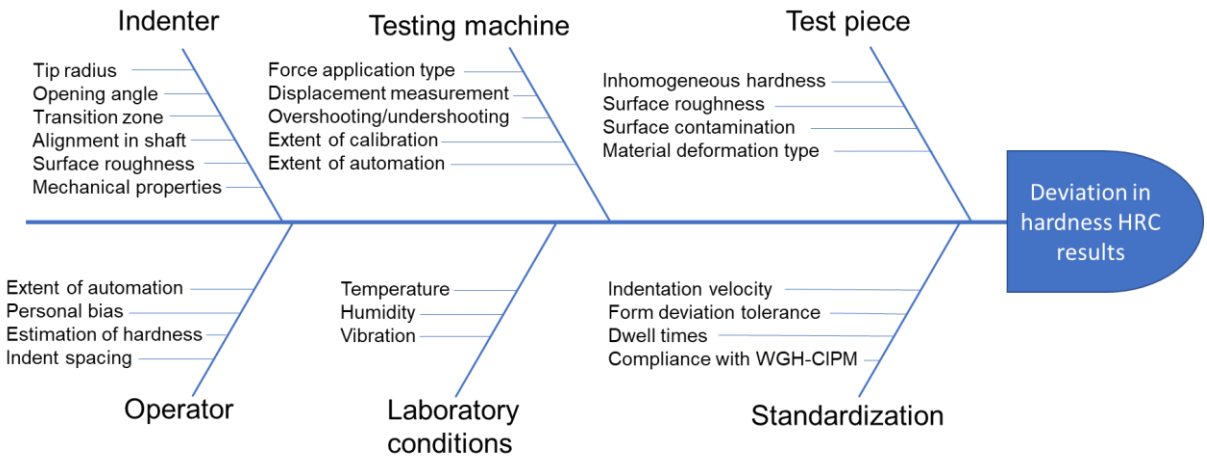

Figure 11: Ishikawa diagram for Rockwell hardness value

The factors pertaining to the test piece such as the surface roughness and surface contamination, can be readily handled and brought under control. Eliminating the inhomogeneity of the hardness of a material across its surface, on the other hand, is much more complex and must be addressed from a material science standpoint.

Likewise, the factors affecting the hardness deviation due to the variations in the laboratory conditions are well understood and effectively standardized.

In contrast, a hardness testing machine operator is provided a high degree of autonomy when conducting a hardness test, including the depth measurement, timekeeping, an a priori estimation of hardness, and spacing the indents. This contributes to an indeterminate amount of hardness deviation. To alleviate the impact of personal bias, it is prudent to opt for an automated approach to hardness measurement.

The primary hardness testing standard at the PTB aligns with the requirements of a standardized machine [48]. The application of the test force using a dead-weight system and the measurement of the indentation depth using a laser interferometer ensure the lowest amount of uncertainty in the force and indentation depth. Besides, the variation in the force levels (overshooting and undershooting) and machine hysteresis are periodically checked and can be classified as insignificant sources of error. The factor pertaining to the testing machine that remains to be addressed is the implementation of a standardized testing cycle. Addressing this factor also reduces the personal bias of the user and facilitates the harmonization of the national primary standards.

https://doi.org/10.7795/110.20250619

Therefore, the first objective is to implement a standardized testing cycle for all the Rockwell hardness scales in the primary hardness testing machine of the PTB and ensure the compliance with the standard [38]. In addition, the objective is to eliminate the need for an expert user to perform the calibrations of hardness reference blocks. Furthermore, it is intended that the implementation of this procedure is machine-independent so that it can foster better measurement comparability between calibration laboratories.

The next objective is in line with the factors affecting the hardness deviation due to the indenter. These factors can be grouped into two categories: geometric and nongeometric. The nongeometric factors, such as the mechanical properties of indenters are to be dealt with from a materials science perspective. The geometric factors such as the tip radius and the opening angle are among the largest contributors to the measurement uncertainty [49–51]. In light of these facts, the objective is to investigate and determine a suitable correction method that can be used to correct hardness deviations as a function of the geometric deviations of indenters. Additionally, the objective is also to develop a calibration strategy for the calibration of the spherical tip radius of a Rockwell diamond indenter.

The final objective of this work is to reduce the measurement uncertainty of Rockwell hardness testing. Furthermore, this work seeks to implement the definitions and analyze the feasibility of the definitions put forth by the standards, highlighting shortcomings and suggesting improvements for the betterment of the field of material testing and also to take a step towards a worldwide unified Rockwell hardness scale.

https://doi.org/10.7795/110.20250619

4. Calibration of Rockwell Hardness Reference Blocks

Hardness reference blocks are means through which the Rockwell hardness scale is disseminated from an NMI all the way down to the end user. Besides their use in calibration and verification of a hardness testing machine, they are also used during installation, maintenance, and as measurands during measurement campaigns between NMIs. Since they are key to ensuring traceability in hardness measurements, their calibration is standardized in a separate part of ISO 6508 [38] with tighter tolerances.

Principally, hardness reference blocks used in Rockwell hardness testing are blocks of metal that are heat treated to attain a particular hardness value. The metals that are most used are steel, aluminum, and brass. Hardness reference blocks come in different shapes and sizes depending upon the Rockwell hardness scale they need to cater to. Desirable properties that a hardness reference block needs to possess are stability and longevity of hardness value and a homogeneous hardness over the surface and along the depth.

Measuring the Rockwell hardness value of a hardness reference block is straight-forward. However, calibrating it poses a special challenge. This is because the standard [38] states that the indentation speed during the loading phase of a Rockwell hardness test cycle after 80 % of the total force F is applied needs to be between 15 µm/s and 40 µm/s. With regards to the initial speed of indentation up to the exertion of 80 % of the total force F on the hardness reference block, no specific information is provided.

The general effect of the force application rate on the measured Rockwell hardness value has been discussed in detail by Low [34]. The justification behind fixing the final indentation speed is its strong influence on the measured Rockwell hardness value. It has been shown in [34] that changing the final speed of indentation from 0.5 µm/s to 70 µm/s results in a decrease of the measured hardness by 0.6 HRC for a material with a nominal hardness of 50 HRC. This deviation is significant, and hence the standard [38] steps in to ensure the harmonization of the Rockwell hardness scale.

To further enhance the agreement between the primary standards of different nations, the CCM-WGH of the CIPM has agreed on a fixed value for several parameters of a Rockwell hardness test, including the final speed of indentation. For instance, the recommended final speed of indentation for the scale HR15N is 15 µm/s, whereas 30 µm/s for the scales HR30N, HR45N, and HRC [35].

It is intuitive that the extent of penetration is inversely proportional to the hardness of the material. Considering the indentation depth vs. time diagrams of a soft and hard material as shown in Figure 12, it is obvious that if the indentation speed v_2 is kept constant, the indentation speed v_1 must vary based on the hardness of the material. As the hardness of the material is a quantity that is measured during a hardness measurement and is not known a priori, the information about the value of the initial speed of indentation is unavailable. Thus, the setting of the initial speed of indentation during a measurement and, in general, the compliance with the standard [38] is complicated.

https://doi.org/10.7795/110.20250619

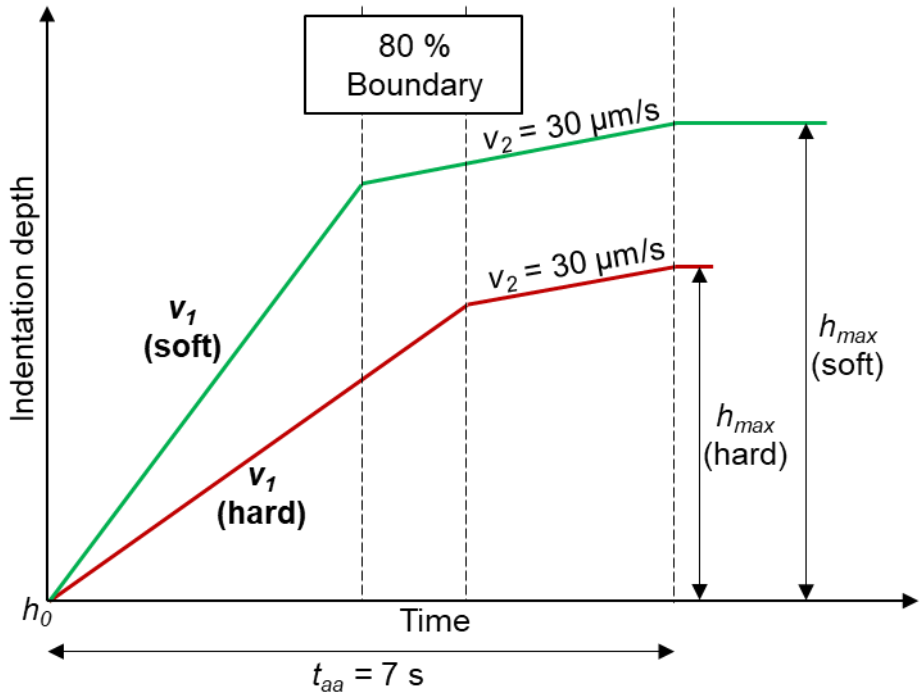

Figure 12: Indentation depth vs. time diagrams for a soft and a hard material

A rudimentary method to ensure compliance with the standard [38] is to perform multiple pre-measurements and estimate the hardness of the hardness reference block to subsequently set the initial speed of indentation. This is a time-consuming method and requires an expert user. Moreover, a hardness reference block has limited space on its surface where hardness calibrations can be performed. Therefore, pre-measurements lead to wastage of material and increase the overall cost to the customers.

A novel method that uses the information obtained about the material's hardness during the preload phase of a Rockwell hardness test has been developed and tested at the PTB for the Rockwell hardness scale HRA [52]. This method eliminates the need to perform pre-measurements and enables the determination of the initial speed of indentation during the measurement itself. Principally, a functional relationship is established between the indentation depths h_0, h_{max} and the material hardness, which are known as characteristic curves. These curves serve as a database for all future measurements and help calculate the initial speed of indentation v_1. However, this method and the characteristic curves are specific to the hardness testing machine with which they are determined.

Some metrology institutes redesigned the load monitoring system to include an external force sensor on the screw drive to detect the 80 % of the total force without altering the value or the accuracy of the test force being applied [53]. Other institutes use a similar approach with a closed loop system to monitor the load signal continuously and adapt the indentation speed accordingly [54]. Nonetheless, these methods allow laxity to the force application time t_{aa} and render its control arduous.

https://doi.org/10.7795/110.20250619

4.1. Estimation of the indentation speed

In order to estimate the indentation speed v_1, characteristic curves are required. Figure 13 shows the steps followed to calculate the indentation speed. Firstly, the indentation depth h_0 is measured during a Rockwell hardness measurement. Using this measured value an estimate of the material's hardness is made, followed by the estimation of the indentation depth h_{max}.

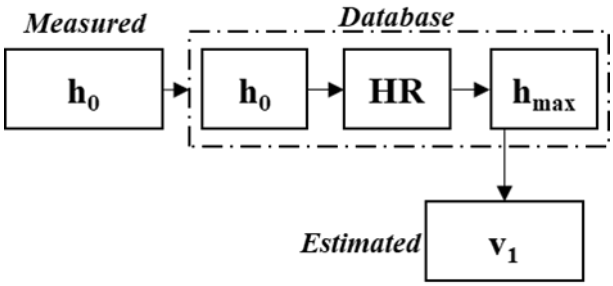

Figure 13: Automation concept for estimating the initial speed of indentation

To obtain the ratio of the indentation depths during the application of the additional test force, a linear relationship between the force and indentation depth is assumed in [52]. Regular work with the hardness testing machine has shown that this assumption is inaccurate and leads to variations in the final speed of indentation v_2. According to [55], the relationship between the test force and the indentation depth is best described using a power law, as shown in Equation 7.

$$F = ah^b \qquad \textbf{Equation 7}$$

In Equation 7, a is a material-dependent constant, whereas b is an indenter-dependent constant. There exists a class of indenters called self-similar indenters, where the shape of the indent remains the same during an indentation process and only the size increases with the increasing indentation depth. Berkovich and Vickers indenters belong to this class of indenters. It has been proven in [56] that the value of the constant b is 2 for self-similar indenters.

The indenters used in Rockwell hardness testing are either spherical or spheroconical in shape. Both these indenters do not belong to the category of self-similar indenters since the shape of the indent changes depending on the test force and the mechanical properties of the material being tested.

To determine an analytical relation between the test force and the indentation depth when a spherical indenter is used, the indentation depth can be decomposed into elastic h_e and plastic h_p portions as shown in Equation 8 [57].

https://doi.org/10.7795/110.20250619

$$h = h_e + h_p$$ **Equation 8**

The elastic deformation caused by a spherical indenter can be calculated using Hertzian contact theory [58]. For plastic deformation to occur, the maximum contact pressure must exceed 1.6 times the yield stress of the metallic material [59]. Inserting the respective deformations in Equation 8, a relation between the indentation depth and the test force in terms of the radius of the indenter R, the reduced elastic modulus E_r, and the yield stress of the material σ_y is obtained, as shown in Equation 9.

$$h = \left[\frac{9}{16 \cdot R \cdot E_r^2}\right]^{1/3} \cdot F^{2/3} + \frac{0.058}{R \cdot \sigma_y} \cdot F$$ **Equation 9**

From Equation 9, it can be deduced that elastic deformations dominate the total deformation for hard materials if the radius of the indenter is significantly larger than the indentation depth. When the indentation depth and the radius of the indenter are of similar magnitude, the type of deformation depends on the material properties. In any case, the value of the constant *b* lies between 1 and 2.

Due to the geometry of the spheroconical indenter, the shape of the indent depends on the indentation depth. This complicates the derivation of an analytical relationship between the test force and the indentation depth. Hence, measurement data of the test force and indentation depth obtained from multiple hardness measurements is fitted using a nonlinear least squares method to determine the value of the constants in Equation 7. The results of the curve fit for three hardness reference blocks of steel with different hardness levels and one hardness reference block of aluminum and brass each are presented in Table 3. The maximum test force applied on the material is designated using the Rockwell hardness scale.

From the tabulated results, the following conclusions can be drawn. Firstly, the value of the constant *a* depends on both the material and the test force. When a material is tested with a larger test force, the value of the constant *a* decreases. This could indicate differences in material properties with increasing indentation depth, also called the indentation size effect [60]. Secondly, the average value of the constant *a* increases with an increase in the hardness of the material.

Observing the behavior of the constant *b* reveals that it is bound between the values of 1 and 2. Furthermore, the results of testing a soft material with high test forces indicate that the value of the constant *b* tends towards the value of 2. This is because the spherical tip of a spheroconical indenter can be neglected when the indentation depths are very large compared to the height of the spherical tip, which results in the spheroconical indenter behaving like a self-similar indenter.

https://doi.org/10.7795/110.20250619

Nominal value of hardness reference block	Maximum test force w.r.t Rockwell scale	Constants	
		a	b
20 HRC (steel)	HRA	0.76	1.38
	HRD	0.50	1.48
	HRC	0.30	1.58
40 HRC (steel)	HRA	1.80	1.29
	HRD	1.24	1.38
	HRC	0.77	1.48
65 HRC (steel)	HRA	3.75	1.23
	HRD	2.79	1.31
	HRC	2.03	1.38
110 HV (aluminum)	HRA	0.20	1.55
	HRD	0.14	1.62
35 HRA (brass)	HRA	0.14	1.56
	HRD	0.10	1.64

Table 3: Values of constants *a* and *b* for different materials and hardness obtained by describing the test force and indentation depth data using a power law function as shown in Equation 7

Equation 7 can be rearranged to express the test force and the constants in terms of the indentation depth, as shown in Equation 10.

$$h = \left(\frac{F}{a}\right)^{1/b} \quad \textbf{Equation 10}$$

Let *c* be the proportion of the total indentation depth associated with 80 % of the total test force (see Figure 6). Thus, the ratio *α*, which is the ratio of the indentation depth when the test force is between 80 % and 100 % of the total test force to the indentation depth when the additional test force is applied, is given by Equation 11.

https://doi.org/10.7795/110.20250619

$$\alpha = (1 - c) \cdot \frac{h_2}{h_{max}} \qquad \textbf{Equation 11}$$

Assigning the respective test forces and inserting Equation 10 in Equation 11, the ratio *α* can be rewritten as shown in Equation 12.

$$\alpha = (1 - c) \cdot \frac{F^{1/b}}{F^{1/b} - F_0^{1/b}} \qquad \textbf{Equation 12}$$

The amount of time in which the final part of the additional test force must be applied with a constant speed v_2 is given by the Equation 13.

$$t_2 = \frac{\alpha \cdot h_{max}}{v_2} \qquad \textbf{Equation 13}$$

Likewise, the initial speed of indentation v_1 for the application of the additional test force is given by the Equation 14. With the help of the machine-specific characteristic curves, an estimate of the variable h_{max} can be obtained. Thus, every variable in Equation 14 is known, and this enables the estimation of the indentation speed during the preload phase of a Rockwell hardness test.

$$v_1 = \frac{[(1 - \alpha) \cdot h_{max}]}{[t_{aa} - t_2]} \qquad \textbf{Equation 14}$$

4.2. Universal automation approach

The estimation of the initial speed of indentation described in the previous subsection uses characteristic curves, which are unique to a hardness testing machine. A universal and machine-independent approach to automation is attractive due to the ease of transfer of the characteristic curves to any computerized Rockwell hardness testing machine. In this subsection, the critical parameters that affect the characteristic curves are addressed, and methods to determine these are described.

4.2.1. Surface detection

In most hardness testing machines, the occurrence of the force signal exceeding a predefined threshold is taken to indicate the initial contact between the indenter and the material. Another technique to determine the detection of the surface involves the

https://doi.org/10.7795/110.20250619

monitoring of the speed of the indenter. An abrupt deceleration of the indenter is indicative of the detection of the initial contact. Since the Rockwell hardness value is calculated using the differential depth with the indentation depth at the preliminary test force as the reference, most methods of surface detection are effective and do not affect the hardness measurement. In contrast, establishing universal characteristic curves requires the absolute values of indentation depths h_0 and h_{max}.

Therefore, an appropriate force threshold must be chosen such that the surface detection error is insignificant compared to the measured value of the indentation depth h_0. The finite deformation Δx as a result of the threshold force acting on the material can be estimated using the Equation 9 and corrected accordingly.

4.2.2. Machine compliance

The indentation depth measured by a displacement measurement system during a hardness test consists of the deformation due to the material-indenter interaction and the deformation of the machine. The extent of the deformation in the machine depends on the test load and the design of the machine frame. For instance, a C-shaped machine frame is more prone to deformation during loading in comparison to a rigid machine frame. Since the indentation depths for the calculation of the Rockwell hardness value are measured while the preliminary test force is acting, the contributions of the machine deformation cancel each other out. However, machine-independent absolute values of the indentation depths h_0 and h_{max} are required for the establishment of universal characteristic curves. Therefore, the accurate determination of the machine compliance is crucial.

Different methodologies could be used to measure the machine compliance. The ISO standard [37] outlines a method to minimize the scattering of measurement results caused by the hysteresial flexure of the testing machine. Due to the mechanical construct of the machine, there is an inevitable presence of elastic air gaps in addition to the elastic deformation of machine parts. Thus, the standard [37] states that multiple hardness tests with the highest test force using a spherical indenter having a radius larger than 5 mm are to be performed on a hard material with a hardness of at least 60 HRC before beginning with hardness testing. Consequent indentations are performed on the same location, which leads to the local hardening of the region of indentation. With every indent, the hardness of the material increases. Performing ten indents and averaging the results of the final three indents, the hardness value must be within 1 HR unit of the value of the constant N (Equation 4) to ascertain the successful completion of the machine hysteresis verification.

Although the undertaking of the machine hysteresis verification is pivotal to ensure that no offset errors creep into the characteristic curves, it does not determine the absolute value of the machine compliance. Furthermore, it does not account for the deformation of the indenter, the indenter holder and most crucially the deformation of material

https://doi.org/10.7795/110.20250619

placed under the test piece. One potential solution is to utilize a length measuring system such as an interferometer to quantify the machine deformation. If the machine design and the material properties of the machine frame are available, a finite element simulation could also be performed. Both of these methods are cumbersome and not the most feasible.

In this work, the machine compliance is determined using the method described in [25]. This approach is generally used to determine the machine compliance in IIT. The total compliance is assumed to be the sum of the contact compliance between the indenter and the material and the compliance of the machine frame, like two springs acting in series. After choosing a suitable material, Rockwell hardness measurements for three levels of test force, such as the Rockwell scales HRA, HRD, and HRC, are performed. The slope of the unloading curve for each of the measurements is extracted to obtain the total machine stiffness. The inverse of the total stiffness gives the total compliance. The contact stiffness between the indenter and material is calculated using Sneddon's equation [61]. By making the assumption that the hardness of the material and the reduced elastic modulus are independent of the indentation depth, Sneddon's equation can be rearranged to express it in terms of the maximum test force F_{max}. Thus, the total compliance C_t is given by the Equation 15, where k is a constant and C_f is the machine compliance.

$$C_t = \frac{k}{\sqrt{F_{max}}} + C_f \qquad \textbf{Equation 15}$$

Since Equation 15 is a linear equation with C_t as the dependent variable and $F_{max}^{-0.5}$ as the independent variable, the y-intercept gives the machine compliance C_f. With the known value of the machine compliance, the machine-independent value of the indentation depth h_{max} can be obtained from its machine-dependent measured value using Equation 16, where F is the total test force of the respective Rockwell scale.

$$h_{max} = h_{\max\,(measured)} - F \cdot C_f \qquad \textbf{Equation 16}$$

Likewise, the universal value of the indentation depth h_0 is given by the Equation 17, where F_0 is the preliminary test force of the respective Rockwell scale.

$$h_0 = h_{0\,(measured)} - F_0 \cdot C_f + \Delta x \qquad \textbf{Equation 17}$$

https://doi.org/10.7795/110.20250619

4.2.3. Velocity corrections

Having established the universal characteristic curves and estimated the initial speed of indentation, the next step is to ensure that both the indentation speeds v_1 and v_2 are adhered to during the indentation process. Figure 14 shows the difference between the measured indentation speed (output) and the set indentation speed (input) for different hardness levels of Rockwell scale HR45N. The initial and final indentation speeds are both affected, and deviate from the input indentation speeds, based on the hardness of the material being tested. The extent of the deviation is larger for the indentation speed v_1 than v_2, due to the longer range the indenter traverses during a hardness test. Moreover, the output of the indentation speed for v_1 is much larger for softer materials than harder materials because of the lack of resistance to penetration in a softer material.

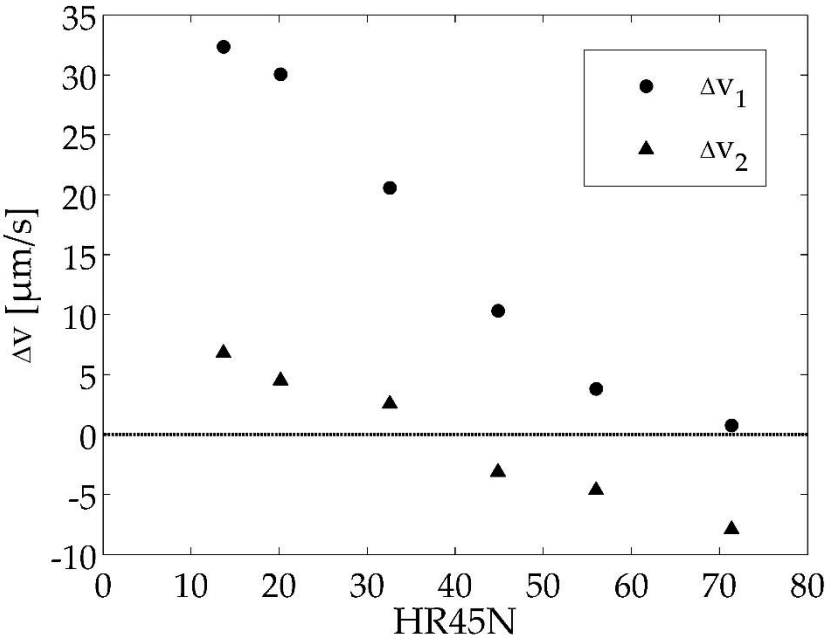

Figure 14: Difference between the measured indentation speed and the assigned indentation speed for different hardness levels

The deviation between the input and output indentation speeds is unique to the indenter and the Rockwell scale. Given the need for precise and repeatable indentation speeds, the speed of the motor must be manipulated based on the hardness of the material and the Rockwell scale to fulfill the criteria set by the standard [38] on the indentation speeds. These modifications are termed here as velocity corrections.

Utilizing hardness reference blocks of different hardness levels, the input indentation speed for both v_1 and v_2 is incremented stepwise and the resulting output indentation speed is recorded. Figure 15 presents the results of this analysis performed for two

https://doi.org/10.7795/110.20250619

sets of input and output indentation speeds. The output to input ratio differs for the indentation speeds v_1 and v_2 but varies linearly for both indentation speeds.

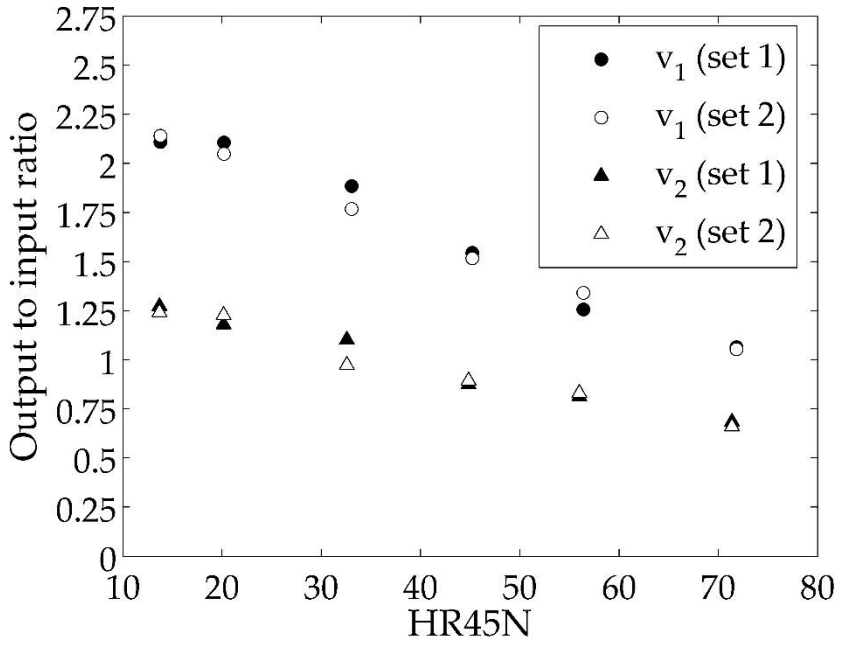

Figure 15: Output to input ratio for different sets of indentation speeds with respect to hardness

As an estimate of the hardness value is made during the preload phase of a Rockwell measurement, it can be used to assign the respective output to input ratios for the indentation speeds v_1 and v_2, respectively, and the motor speed adjusted accordingly. Additionally, the velocity corrections must be determined for each of the Rockwell hardness scales individually.

4.3. Validation of universal characteristic curves

The characteristic curves determined for the Rockwell hardness scale HRC by two independent laboratories, Lab A (project partner) and Lab B (PTB), are presented to validate the concept of universal automation. Considering the machine capabilities of both laboratories, a force threshold of 0.5 N is chosen to detect the contact between the indenter and the material. The measurement of the machine compliance is carried out on 12 hardness reference blocks, with 10 indentations for each of the three test force levels. Irrespective of the choice of the material or hardness, consistent values of machine compliance are measured. The machine compliance for the hardness tester of Lab A is measured to be 75 nm/N. In contrast, a machine compliance of only 9.8 nm/N is measured for the hardness tester of Lab B. The appreciably greater machine compliance for Lab A is attributed to its C-shaped machine frame. Figure 16 visualizes the raw data of the force vs. displacement curves for three levels of test force (HRA in black, HRD in blue and HRC in red) and the force vs. displacement

https://doi.org/10.7795/110.20250619

curves after accounting for the machine compliance of the Lab A. When the test force is close to 1500 N, the contribution of the machine deformation to the total measured indentation depth exceeds 100 µm.

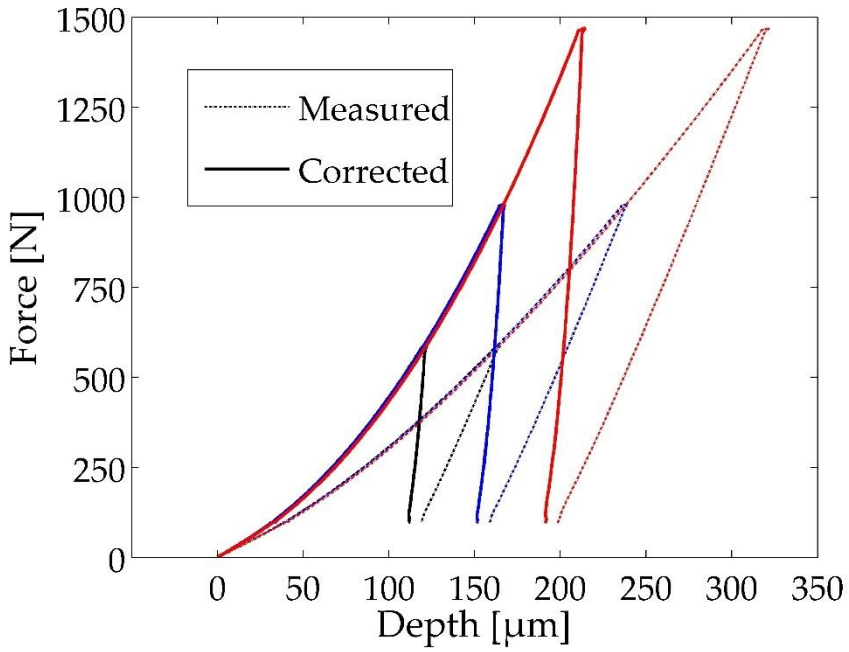

Figure 16: Effect of machine compliance correction on force vs. displacements curves for measurements on Rockwell scale HRA, HRD and HRC

The required Rockwell hardness tests for the establishment of machine-dependent characteristic curves are performed on 15 hardness reference blocks consisting of three industry-typical materials, namely steel, aluminum, and brass. The hardness values of these blocks are chosen in such a way that they span across the hardness range of every Rockwell scale. Unavoidably, the nominal hardness value of a few of these blocks falls below or exceeds the applicable range of some of the Rockwell scales. Hence, data points from hardness values that lie far beyond the applicable range are duly rejected.

Ten hardness measurements are performed on every hardness reference block to obtain a good statistical distribution of the data set and to reduce the influence of hardness outliers. The average of the hardness values and the indentation depths h_0 and h_{max} is exported into the database to automate the calibration process.

The machine-specific functional relationship between the HRC values and the indentation depth h_0 obtained by Lab A and Lab B is shown in Figure 17. The curves from the two labs differ noticeably across the full range of indentation depths. Accounting for the surface detection error and the respective machine compliances, the individual universal characteristic curves for Lab A and Lab B are shown in Figure 18. A clear

https://doi.org/10.7795/110.20250619

improvement in the agreement between the curves is seen. To incorporate this characteristic curve into the database, a logarithmic function can be used. For the Rockwell scales that use a spherical indenter, a linear functional relationship best describes the characteristic curve. Furthermore, the different materials investigated in this study did not yield any substantial differences from the findings presented here.

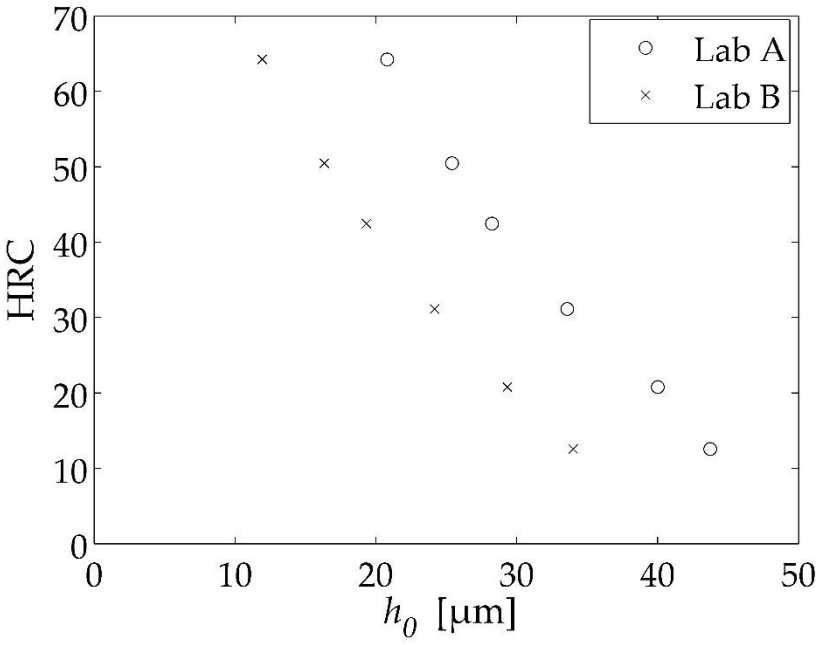

Figure 17: Machine-dependent characteristic curves to estimate the hardness value

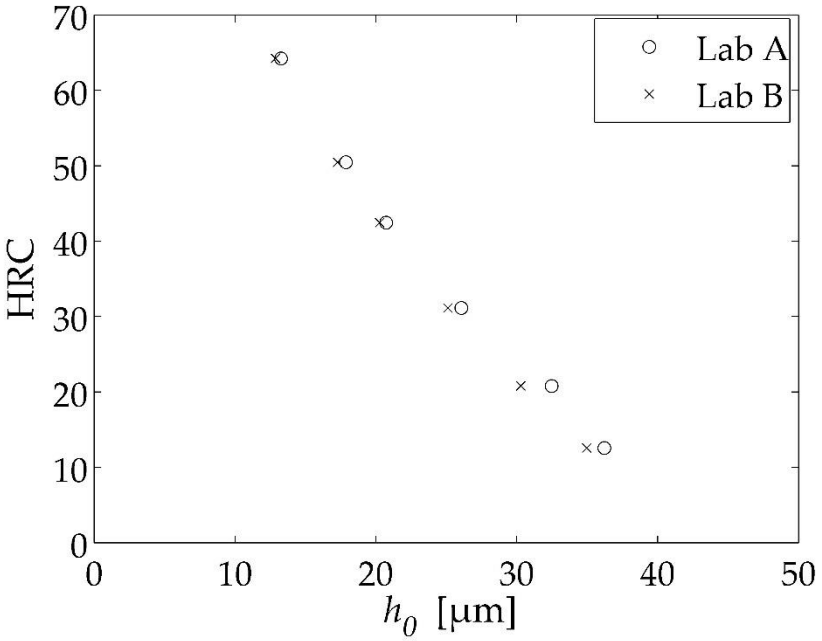

Figure 18: Machine-independent characteristic curves to estimate the hardness value

https://doi.org/10.7795/110.20250619

Likewise, Figure 19 and Figure 20 present the machine-dependent and machine-independent characteristic curves for the estimation of the indentation depth h_{max} from Lab A and Lab B. These universal characteristic curves are also in close agreement, indicating the successful determination of the influencing parameters. A linear function can be used to describe these curves for every Rockwell scale. The results for the machine-dependent and machine-independent characteristic curves for the Rockwell scale HRA and HRD are provided in the Appendix 1 and Appendix 2.

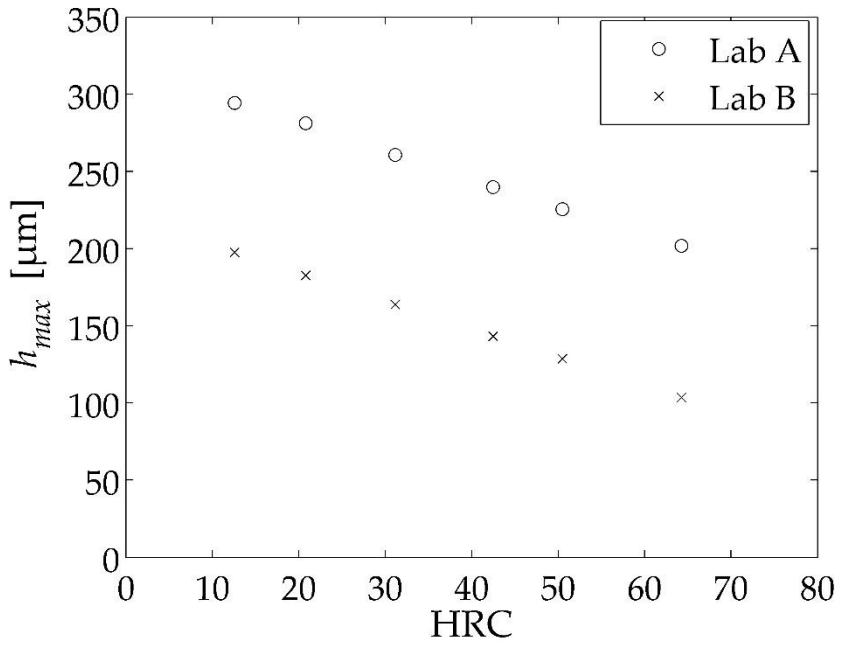

Figure 19: Machine-dependent characteristic curves to estimate the indentation depth h_{max}

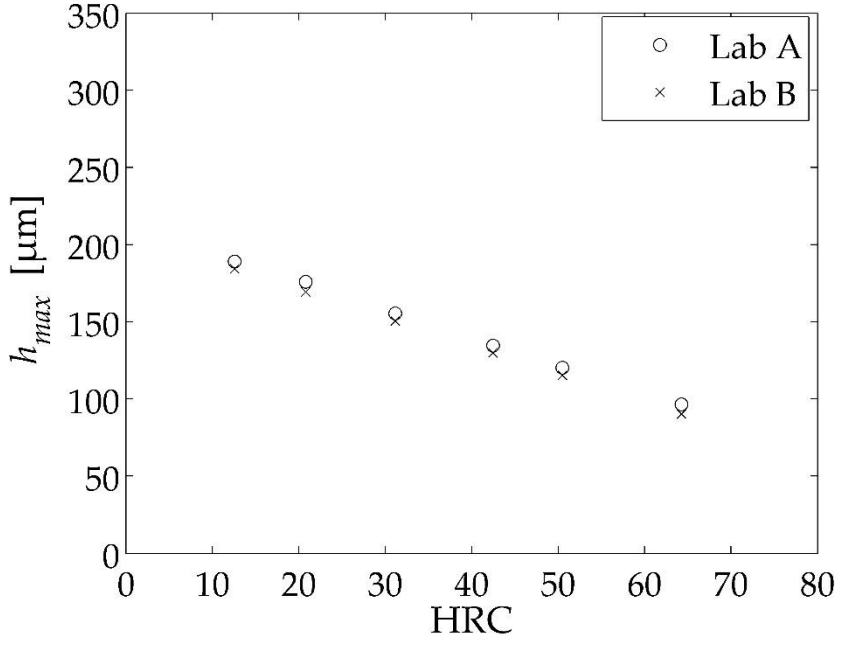

Figure 20: Machine-independent characteristic curves to estimate the indentation depth h_{max}

https://doi.org/10.7795/110.20250619

Similar universal characteristic curves are also obtained for every other standardized Rockwell scale. Given the good agreement between the machine-independent characteristic curves obtained from two independent laboratories that use different hardness testing machines, the universal automation approach can be considered validated. The differences in the universal characteristic curves of the laboratories are minor and could be attributed to the differences in the geometry of the indenter used. According to [34], the indenter geometry is the largest source of uncertainty in Rockwell hardness testing. Hence, the correction of the measured hardness value based on the geometry of the indenter is separately dealt with in the following chapter.

4.4. Implementation

The indentation speeds during the application of the additional test force are measured after the implementation of the automated approach. The results of the hardness and indentation speed measurement for the Rockwell scale HRC are presented in Figure 21.

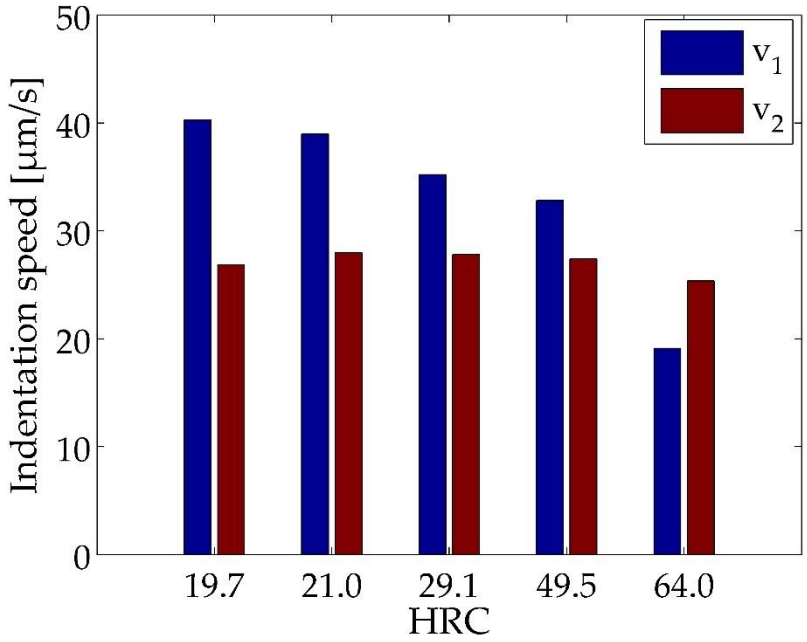

Figure 21: Measured indentation speeds during the application of the additional test force for different hardness levels

Irrespective of the material hardness, a constant final speed of indentation (v_2) of (27 ± 1) µm/s is maintained over the entire range of the HRC scale. The measured indentation speed meets the criteria set by the standard [38]. Naturally, the initial speed of indentation (v_1) depends on the hardness of the material and decreases with the increase in the material hardness.

The implementation and verification of the indentation speeds for Rockwell scales that use a diamond indenter are unproblematic. For Rockwell scales that use a hard metal

https://doi.org/10.7795/110.20250619

spherical indenter, it is noticed that the measured Rockwell value is extremely sensitive to the change in indentation speeds. This effect is exacerbated in combination with lower test forces, such as for the Rockwell scale HR15T. The functional relationship between the hardness value and the indentation depths h_0 and h_{max} changes with a change in the indentation speed. This poses a special challenge in establishing the characteristic curves for the Rockwell scale HR15T.

Another important aspect to consider during the implementation process is the surface roughness of the material. Failure to do so would result in the underestimation or overestimation of the indentation depth h_0. Consequently, the estimation of the hardness, indentation depth h_{max}, and eventually the initial speed of indentation v_1 is directly affected and results in the mismeasurement of the hardness value. Since hardness reference blocks are used in this study and due to the restriction placed by the standard [38] on the roughness value R_a of hardness reference blocks, it can be safely said that the roughness value does not exceed 0.3 µm.

As an inevitable consequence of fixing the final speed of indentation v_2, the undershooting or overshooting of the test force is observed in some cases. For softer materials, the indentation speed v_1 is larger than the indentation speed v_2. This deceleration causes a minimal undershooting of the test force. Similarly, for harder materials, the indentation speed v_1 is smaller than the indentation speed v_2. This accelerates the indenter towards the end of the loading process, causing a slight overshooting of the test force. Both of these circumstances can be avoided by programming a third indentation speed after 99 % of the test force is applied, giving the testing machine enough time to stabilize before coming to a stop.

Finally, it must be reiterated that assuming a linear relationship between the test force and the indentation depth is not accurate. Assuming a linear relationship implies that the value of the constant b in Equation 7 is 1. Thus, the change in the indentation speed from v_1 to v_2 occurs at 80 % of the indentation depth h_2. Considering the value of the constant b to be 2 (quadratic relation), the change would occur at 89 % of the indentation depth h_2. For values of the constant b listed in Table 3, the range for the change in the indentation speed lies between 85 % and 87 % of the indentation depth h_2. Therefore, the discrepancy arising from the incorrect assumption for the relation between the test force and the indentation depth results in the initial indentation speed being sustained for a longer duration than prescribed. This adversely affects the final indentation speed by varying it from the specified value, contingent on the estimated value of the initial indentation speed.

https://doi.org/10.7795/110.20250619

5. Development of Indenter Geometry Correction

The simplicity of the Rockwell hardness definition comes at a cost. This is especially true when the influence of the preliminary load, main load, tip radius or the opening angle of the indenter on the Rockwell hardness test result needs to be investigated. This is a direct consequence of Rockwell hardness being solely defined based on the permanent depth of indentation. On the contrary, other definitions of hardness, such as Vickers or Brinell, include the test force and some indenter geometry parameters, which facilitate the estimation of the measurement uncertainty using Monte Carlo simulations [62–64].

Another important aspect besides the estimation of measurement uncertainty is the correction of the measured hardness values that are obtained through indenters that deviate from the ideal geometry. To shed some light upon this problem, the Rockwell hardness value of hardness reference blocks for five levels of hardness in the HRC scale is measured using three different indenters (see Table 4).

Nominal HRC values	Measured HRC values with			Absolute Difference between PTB indenters	Largest difference between PTB and EDKx
	PTB indenters		EDKx		
	EDK2	EDK3			
20	19.3	19.5	20.9	0.2	1.6
30	30.1	30.6	31.2	0.5	1.1
40	40.4	41.0	42.5	0.6	2.1
50	50.1	50.7	50.5	0.6	0.4
65	63.8	64.1	64.2	0.3	0.4

Table 4: Rockwell hardness scale HRC test results using different indenters

The indenters EDK2 and EDK3 belong to the PTB, whereas the indenter EDKx belongs to a calibration laboratory. The presented result is the average of 5 measurements. A maximum difference of 0.6 HRC units is observed in the results between the PTB indenters and up to 2.1 HRC units between the PTB and the calibration laboratory results.

Although the hardness reference blocks have the same nominal value and originate from the same batch and a single manufacturer, the test pieces were different. Thus, the results between the PTB and the calibration laboratory differ not only due to the

https://doi.org/10.7795/110.20250619

indenter geometry but also due to the test piece, testing machine, testing location, etc. Furthermore, no correction factors have been applied to any of these measurement results. It must be mentioned that it is a common practice in the industry and endorsed by the standard [36] to apply correction factors to reduce the bias or offset from the PTB calibrated hardness values.

The indenter tip radius and the opening angle of the indenters EDK2, EDK3, and EDKx have been calibrated using the HRTS, and the results are shown in the Table 5. No quantitative or qualitative information about the transition zone is available.

Indenter geometry	Indenter name		
	EDK2	EDK3	EDKx
Tip radius	193.2 µm	197.1 µm	195.0 µm
Opening angle	119.99°	120.04°	120.44°

Table 5: Geometric properties of three Rockwell diamond indenters measured by the HRTS with a stylus tip radius of approximately 2 µm

The results presented in the Table 4 can be interpreted based on the geometric properties of the indenters listed in Table 5. Since the tip radius and the opening angle of the indenter EDK3 are larger than those of EDK2, the hardness values measured with the indenter EDK3 are also always larger than those measured with the indenter EDK2. This is because an increase in tip radius or opening angle increases the area of the indenter in contact with the sample. As the applied force on the sample is a predefined constant, the indentation depth reduces consequently. A reduction in indentation depth implies that the measured hardness is larger. Similarly, the measured hardness using EDKx for nominal values of 20 HRC, 30 HRC, and 40 HRC is much larger than the PTB indenters due to the significantly larger opening angle of EDKx. Another important observation is that for harder blocks such as 50 HRC and 65 HRC, the measured value with EDKx is comparable with results of the PTB indenters. This can be explained by the relatively good agreement between the calibrated tip radii values of the indenters. Intuitively, the tip radius has a larger effect on harder materials than the opening angle. For softer materials, the opening angle of the indenter is critical.

Unfortunately, ideal hardness values measured using an ideal indenter do not exist. Hence, there exists a need to correct the presented hardness values based on their deviation from the ideal geometry of a Rockwell indenter. Currently, the method published in [65], which is based on the determination of the indenter area function for a group standard of Rockwell indenters, is used at the PTB. The idea of a group standard

https://doi.org/10.7795/110.20250619

was conceived by R. S. Marriner [66] and F. Petik [17] but realized by D. Schwenk et al. in [67]. Another promising method to correct the measured Rockwell hardness values based on a modelling approach was presented by D. Schwenk et al. in [68]. Since this work is published solely in the German language, it has not attracted international attention. Furthermore, this method has never been compared to other available methods for hardness correction, nor has it been validated.

5.1. Derivation of an equivalent Rockwell hardness number

In this subsection, the derivation of an equivalent Rockwell hardness number is provided. This is followed by the application of the Schwenk's method [68] on the results of Table 4 and a systematic comparison with the group standard method.

The idea behind this method is the modelling of a functional relationship between the Rockwell hardness value (*HR*) and a theoretical permanent depth of indentation (h_{th}) based on empirical and regression analysis. The physical process during a Rockwell hardness test can be described in terms of the ratio of the applied force to the indentation area by the Kick's law of proportional resistances [69]. Thus, two hardness values for the preliminary force and the total force, HR_{F_0} and HR_F respectively, can be determined during a single Rockwell hardness test cycle. If the testing conditions are kept unchanged, these two hardness values would be constants. It can then be assumed that small variations in the indenter geometry or the testing forces alter neither the hardness values nor the stress distribution in the indentation zone. For simplicity, the elastic relaxation of the material after removal of the additional force, the differences in the elastic relaxation of the indentation boundary at different force levels and the pile-up of material is not considered.

Mathematically, the hardness can be expressed using the Equation 18 and Equation 19, where F_0 is the preliminary test force, F is the total test force, A_{F_0} is the indentation area when F_0 is applied and A_F is the indentation area when F is applied.

$$HR_{F_0} = \frac{F_0}{A_{F_0}} \qquad \textbf{Equation 18}$$

$$HR_F = \frac{F}{A_F} \qquad \textbf{Equation 19}$$

From the model, the theoretical permanent depth of indentation is given by the Equation 20, where h_{F_0} is the indentation depth corresponding to the preliminary test force F_0 and h_F is the indentation depth corresponding to the total force F.

https://doi.org/10.7795/110.20250619

$$h_{th} = h_F - h_{F_0}$$ **Equation 20**

Now, consider the 2D profile of an ideal Rockwell diamond indenter as shown in Figure 22. Depending on the hardness of the material being tested, different regions of the indenter come into contact with the material during the application of the preliminary test force and the additional force. The possible scenarios are:

1. Contact only with the spherical region during the application of the preliminary test force and the additional test force. This would be the case if the tested material is extremely hard.
2. Contact with the spherical region during the application of the preliminary test force, whereas a contact with the conical region when the additional test force is applied. This would indicate that the tested material is moderately hard.
3. Contact with the spherical and the conical region during the application of the preliminary test force and the additional test force. This would occur for a relatively soft material.

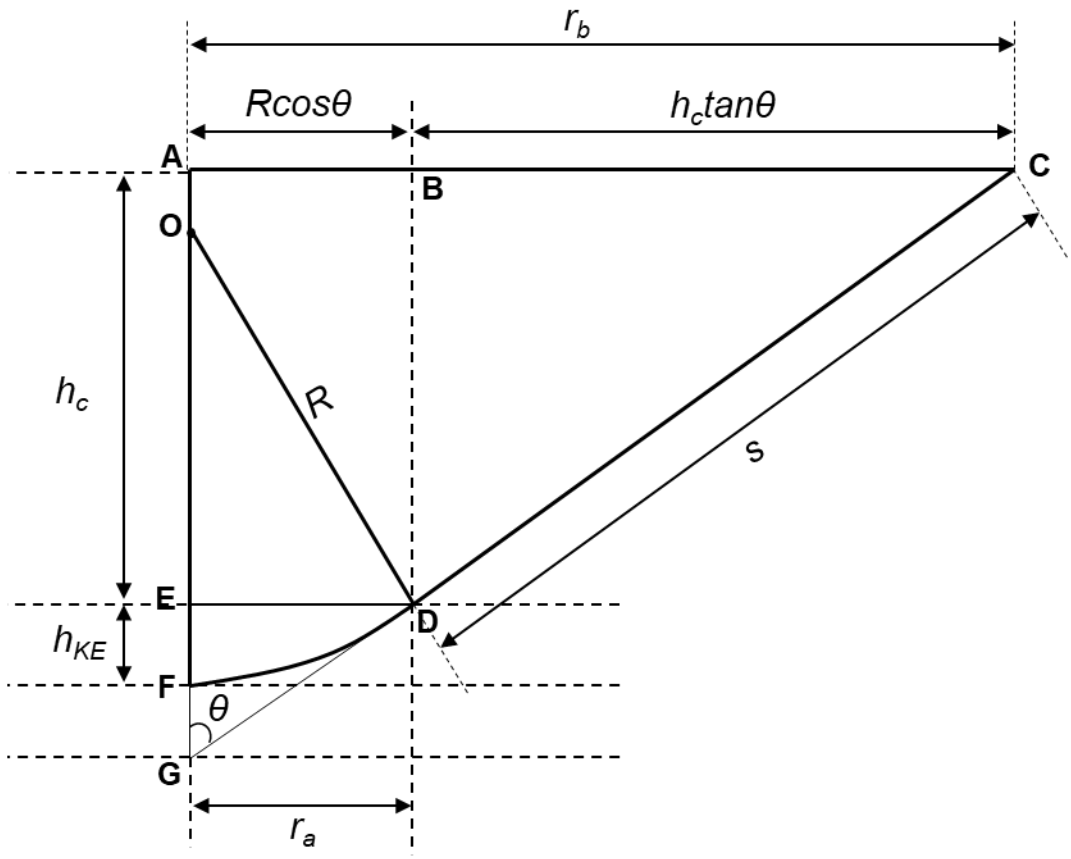

Figure 22: 2D sketch of an ideal Rockwell diamond indenter

https://doi.org/10.7795/110.20250619

Therefore, for Case 1, the theoretical depth of indentation h_{th_1} is given by the Equation 21.

$$h_{th\_1} = h_F - h_{F_0} = \frac{F}{2\pi R \cdot HR_F} - \frac{F_0}{2\pi R \cdot HR_{F_0}} \quad \textbf{Equation 21}$$

The indentation depths in Equation 21 are calculated using the Equation 22 (area of a spherical cap A_K), where h is the indentation depth.

$$A_K = 2\pi Rh \quad \textbf{Equation 22}$$

For Case 2:

The indentation depth at the preliminary force is the same as that as Case 1. However, the indentation depth at the total load is given by the Equation 23, where h_{KE} is the indentation depth until the end of the sphere and h_c is the indentation depth from the beginning of the conical section, as shown in the Figure 22.

$$h_F = h_c + h_{KE} \quad \textbf{Equation 23}$$

From the triangle OED,

$$\sin\theta = \frac{OE}{OD} = \frac{R - h_{KE}}{R} \quad \textbf{Equation 24}$$

Hence,

$$h_{KE} = R(1 - \sin\theta) \quad \textbf{Equation 25}$$

From the section of the conical frustum ABCDE, we calculate h_c.

Area of the conical frustum, A_c is given by the Equation 26, where s is the length of the cone flank and r_a and r_b are the radii of the cross-sections at the beginning and end of the conical region.

https://doi.org/10.7795/110.20250619

$$A_c = \pi s(r_a + r_b) \quad \textbf{Equation 26}$$

From the Figure 22, A_c can be rewritten using Equation 27.

$$A_c = \pi \frac{h_c}{\cos\theta}(R\cos\theta + (R\cos\theta + h_c\tan\theta)) \quad \textbf{Equation 27}$$

Multiplying the terms gives Equation 28.

$$A_c = 2\pi R h_c + \frac{\pi h_c^2 \tan\theta}{\cos\theta} \quad \textbf{Equation 28}$$

This is a quadratic equation in h_c. Thus, it can be expressed as shown in Equation 29 and Equation 30.

$$h_c = \frac{-2\pi R \pm \sqrt{4\pi^2 R^2 + \frac{4\pi A_c \tan\theta}{\cos\theta}}}{\frac{2\pi\tan\theta}{\cos\theta}} \quad \textbf{Equation 29}$$

$$h_c = -\frac{R\cos\theta}{\tan\theta} \pm \sqrt{\left(\frac{R\cos\theta}{\tan\theta}\right)^2 + \frac{A_c\cos\theta}{\pi\tan\theta}} \quad \textbf{Equation 30}$$

Now, the theoretical depth of indentation h_{th_2} is given by the Equation 31.

$$h_{th\_2} = h_F - h_{F_0} = h_c + h_{KE} - \frac{F_0}{2\pi R \cdot HR_{F_0}} \quad \textbf{Equation 31}$$

Using Equation 23, Equation 25 and Equation 30, the theoretical depth of indentation h_{th_2} is given by Equation 32.

$$h_{th\_2} = -\frac{R\cos\theta}{\tan\theta} \pm \sqrt{\left(\frac{R\cos\theta}{\tan\theta}\right)^2 + \frac{A_c\cos\theta}{\pi\tan\theta}} + R(1-\sin\theta) - \frac{F_0}{2\pi R \cdot HR_{F_0}} \quad \textbf{Equation 32}$$

https://doi.org/10.7795/110.20250619

Since A_c is given by Equation 33,

$$A_c = A_F - A_{KE} = \frac{F}{HR_F} - 2\pi R h_{KE} = \frac{F}{HR_F} - 2\pi R^2(1 - \sin\theta) \quad \textbf{Equation 33}$$

Equation 32 can now be rewritten as Equation 34,

$$h_{th\_2} = R\left(1 - \sin\theta - \frac{\cos\theta}{\tan\theta}\right) + \sqrt{\left(\frac{R\cos\theta}{\tan\theta}\right)^2 + \frac{(\frac{F}{HR_F} - 2\pi R^2(1-\sin\theta))\cos\theta}{\pi\tan\theta}} - \frac{F_0}{2\pi R \cdot HR_{F_0}} \quad \textbf{Equation 34}$$

For Case 3:

Both h_F and h_{F_0} are given by the sum of h_{KE} and h_c.

Therefore, the theoretical depth of indentation h_{th_3} is given by the Equation 35.

$$h_{th\_3} = \sqrt{\left(\frac{R\cos\theta}{\tan\theta}\right)^2 + \frac{(\frac{F}{HR_F} - 2\pi R^2(1-\sin\theta))\cos\theta}{\pi\tan\theta}} - \sqrt{\left(\frac{R\cos\theta}{\tan\theta}\right)^2 + \frac{(\frac{F_0}{HR_{F_0}} - 2\pi R^2(1-\sin\theta))\cos\theta}{\pi\tan\theta}} \quad \textbf{Equation 35}$$

The next step is to obtain a functional relationship between the HRC values and HR_{F_0} and HR_F. For this purpose, the entire geometry of the indenters is measured using the HRTS. Both the tip radius and the opening angle are expressed in terms of their measured cross-sectional diameters by fitting a suitable polynomial. Using the same indenters, five indents are made on each of the reference hardness blocks listed in Table 5 with a load of 98.07 N. This is followed by five indents with a load of 1471 N. The holding time at the maximum load was set to be five seconds. After unloading, the diameters of the produced indents are optically measured, and the mean value is calculated. For any given load, if the indentation diameter is smaller than 0.2 mm, it indicates that the contact was only in the spherical region. However, if the indentation

https://doi.org/10.7795/110.20250619

diameter is larger than 0.2 mm, the region of contact extends into the conical region. Subsequently, the indentation area is determined depending upon the region of contact with the indenter, followed by the calculation of the hardness values HR_{F_0} and HR_F. The indentation area for the spherical region is given by the Equation 36, whereas for the combination of the spherical and conical region it is given by the Equation 37, where r_I is the indentation radius in mm.

$$A_I = 2\pi R^2\left(1 - \sqrt{1 - \left(\frac{r_I}{R}\right)^2}\right) \quad \textbf{Equation 36}$$

$$A_I = 2\pi R^2(1 - \sin\theta) + \frac{\pi(r_I^2 - 0.01)}{\sin\theta} \quad \textbf{Equation 37}$$

Both *R* (in mm) and *θ* are obtained from the fitted polynomials expressed in terms of the cross-sectional diameters. Inserting the hardness functions HR_{F_0} and HR_F in terms of HRC in the Equation 21, Equation 34 and Equation 35, the theoretical permanent depth of indentation can be computed as function of HRC value. Since, the determination of the inverse function is not straightforward, a regression analysis is performed. In this way, three equations for the three cases expressing the HRC value in terms of the tip radius, opening angle, preliminary force value, total test force value and the measured HRC value are obtained. With the help of these equations, individual parameters can be varied one at a time or in combinations and their influence on the HRC value can be determined. Likewise, the deviations arising from these parameter variations can be corrected if the true values of the input parameters are known.

In [68], the authors have determined the hardness deviations when the geometric properties and the test forces are set at the extreme ends of the permissible tolerances stated in the standard [37]. Performing this analysis with the data presented in the paper while using the formulae derived in this work, a comparison of the results can be undertaken. Calculating the hardness deviations for the tip radius of 190 µm and 210 µm yields the same results (see Appendix 3). The results of the comparison for the opening angle at 120.35° and 119.65° are shown in Figure 23. The red lines indicate the results in [68], whereas the black lines represent the newly calculated values. It can be seen that the shape of the curves is similar, but there is an offset of about 0.2 HRC between the previously published [68] and newly calculated values in this work. Comparing both these results with the hardness deviations calculated by [68], it can be concluded that the previously published results underestimate the effect of a ± 0.35° variation in the opening angle. The newly calculated deviations from the equations derived in this work agree well with the results published in [70].

https://doi.org/10.7795/110.20250619

It was possible to reproduce the exact results shown in [68] for the variation of the preliminary test force at 99.5 N and 96.6N and the total test force at 1486 N and 1456 N. Therefore, the inconsistency in the calculation seems to be tied to the opening angle.

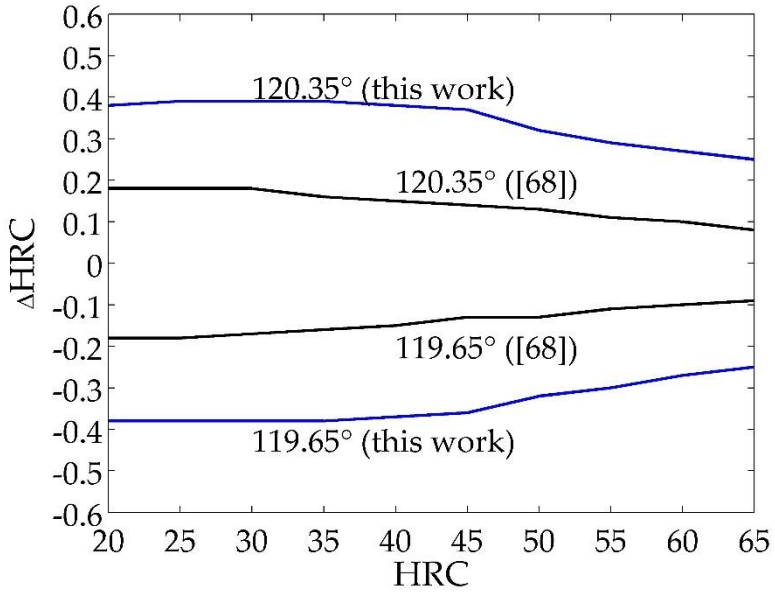

Figure 23: Hardness deviations arising from the deviations in the indenter geometry from the nominal values

Likewise, the combined variations of the opening angle and tip radius are affected, as shown in Figure 24.

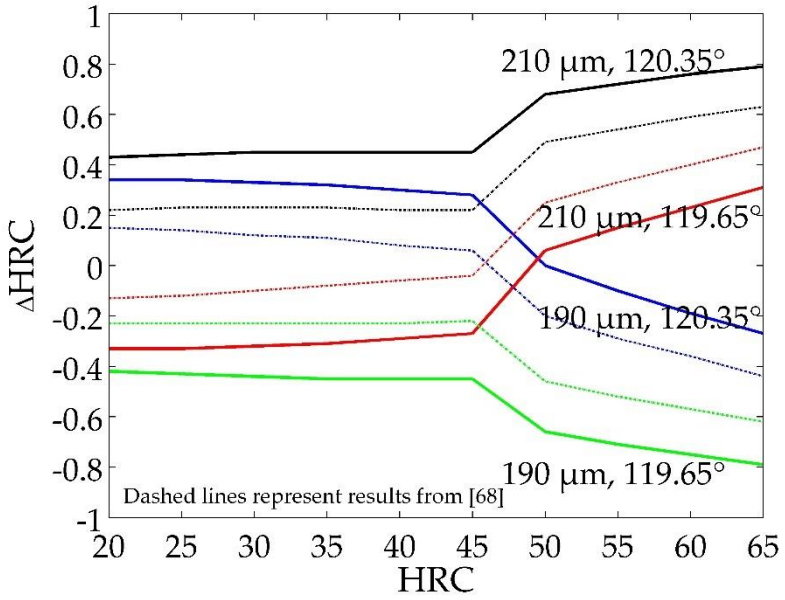

Figure 24: Hardness deviations arising from the deviations in the indenter geometry from the nominal values

https://doi.org/10.7795/110.20250619

The maximum difference increases from 1.2 HRC to 1.6 HRC. The minor difference in the shape of the curve as seen in [68] and that shown here must be due to the differences in the input HRC values in the respective equations. Thus, the formula obtained by the derivation shown in this work is used for the further analysis.

5.2. Comparison of hardness correction methods

Since the geometric parameters of the indenters EDK2, EDK3, and EDKx are known, the hardness deviations from the ideal Rockwell hardness scale HRC can be calculated, assuming the test forces are maintained at the standard defined values. Similarly, the hardness corrections derived from the established group standard of indenters at the PTB for the indenters EDK2 and EDK3 can be computed. The results are presented in Figure 25.

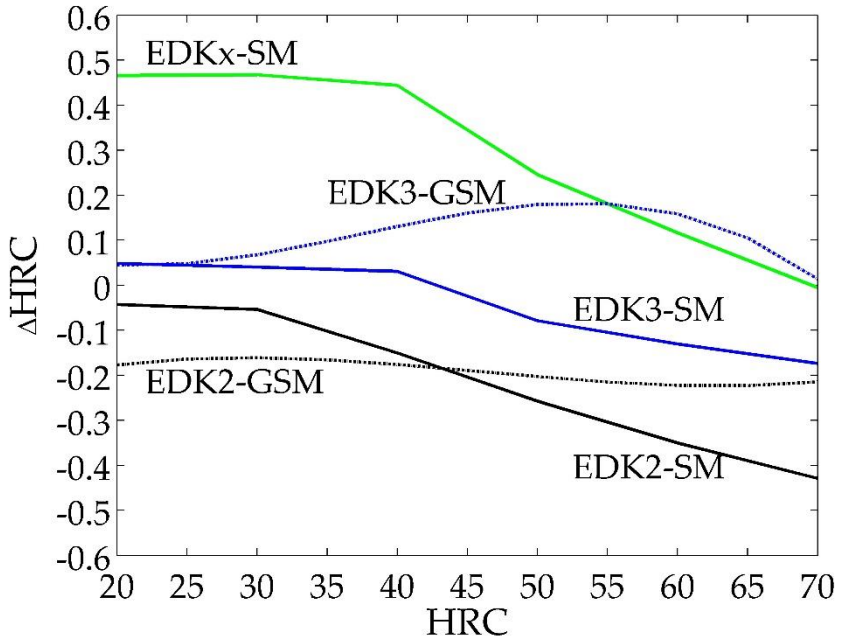

Figure 25: Hardness deviations arising from the deviations in the indenter geometry from the ideal geometry using two methods of correction (GSM: group standard method, SM: Schwenk's method)

As the indenter EDKx does not belong to the group standard, it cannot be corrected using the group standard method (GSM). However, the entire procedure to calculate the hardness deviations using the Schwenk's method (SM) has been performed for it. As a consequence of the opening angle of the indenter EDKx being 0.44° larger than the nominal value, the hardness deviation is also the largest among the three indenters. This deviation is almost constant up until the hardness value of 40 HRC, after which it reduces consistently with the increase in hardness. Generally, when the tip radius is smaller than the nominal value, it is expected that the measured hardness for harder materials would be smaller than the real hardness, which would result in the

https://doi.org/10.7795/110.20250619

hardness deviation being less than zero. However, this is not the case for the indenter EDKx because the positive hardness deviation due to the larger opening angle curtails the negative deviation due to the smaller tip radius. The combined influence of the tip radius and opening angle also explains the larger absolute deviation in hard materials represented by the curve EDK3-SM for the indenter EDK3 than the EDKx, despite its tip radius being 2.1 µm larger. This further indicates that the Case 1, where only the spherical region of the indenter comes in contact with the material during the application of both the test forces, is redundant unless the tip radius and the material hardness are exorbitantly large.

The deviations computed using Schwenk's method for the indenter EDK2 are always below the deviations of EDK3 because both the deviations of the geometric parameters of EDK2 are smaller than that of EDK3. The minimal deviation in the opening angle from the nominal value for the indenters EDK2 and EDK3 leads to a slight negative and positive deviation in softer materials, respectively. With the increase in material hardness, the absolute deviations also increase. In conclusion, the hardness corrections derived from Schwenck's method can be explained in entirety by considering the geometric deviations of the indenter from the ideal shape.

On the other hand, the method of group standard corrects the measured hardness for the indenter EDK2 more or less with a constant value of -0.2 HRC. Given both the geometric properties are smaller than the nominal values, this is acceptable. For the indenter EDK3, the deviations begin with a small positive value, which is in alignment with the slightly larger opening angle of the indenter. At greater hardness, the deviations increase, peaking at 0.2 HRC for a hardness value of 55 HRC, followed by a gradual decrease until around 0 HRC for a hardness value of 70 HRC. This betokens the statistical nature of the GSM correction method, since no correlation with the tip radius of the indenter EDK3, which is about 3 µm smaller than the ideal value, is seen.

The largest discrepancy between the methods is observed to be 0.3 HRC at 60 HRC for the indenter EDK3. Overall, there is a good agreement between the hardness deviation curves of both methods with an average absolute deviation of under 0.14 HRC.

Another way to determine the effectiveness of the Schwenk method is to correct the measured hardness values for the hardness reference blocks shown in Table 4. After correction, if the hardness values obtained from different indenters are the same or at least comparable, the method of correction can be deemed to be successful. The results of this analysis have been presented in Figure 26. For reference, the uncorrected measured value is depicted in gray, and the corrected value according to the group standard method for the PTB indenters EDK2 and EDK3 is represented by black dotted lines. To ease the visualization of the magnitude of correction, the length of the y-axis is set at 2 HRC (except for the hardness reference block with hardness 40 HRC), with a spacing between the major horizontal gridlines set at 0.4 HRC.

https://doi.org/10.7795/110.20250619

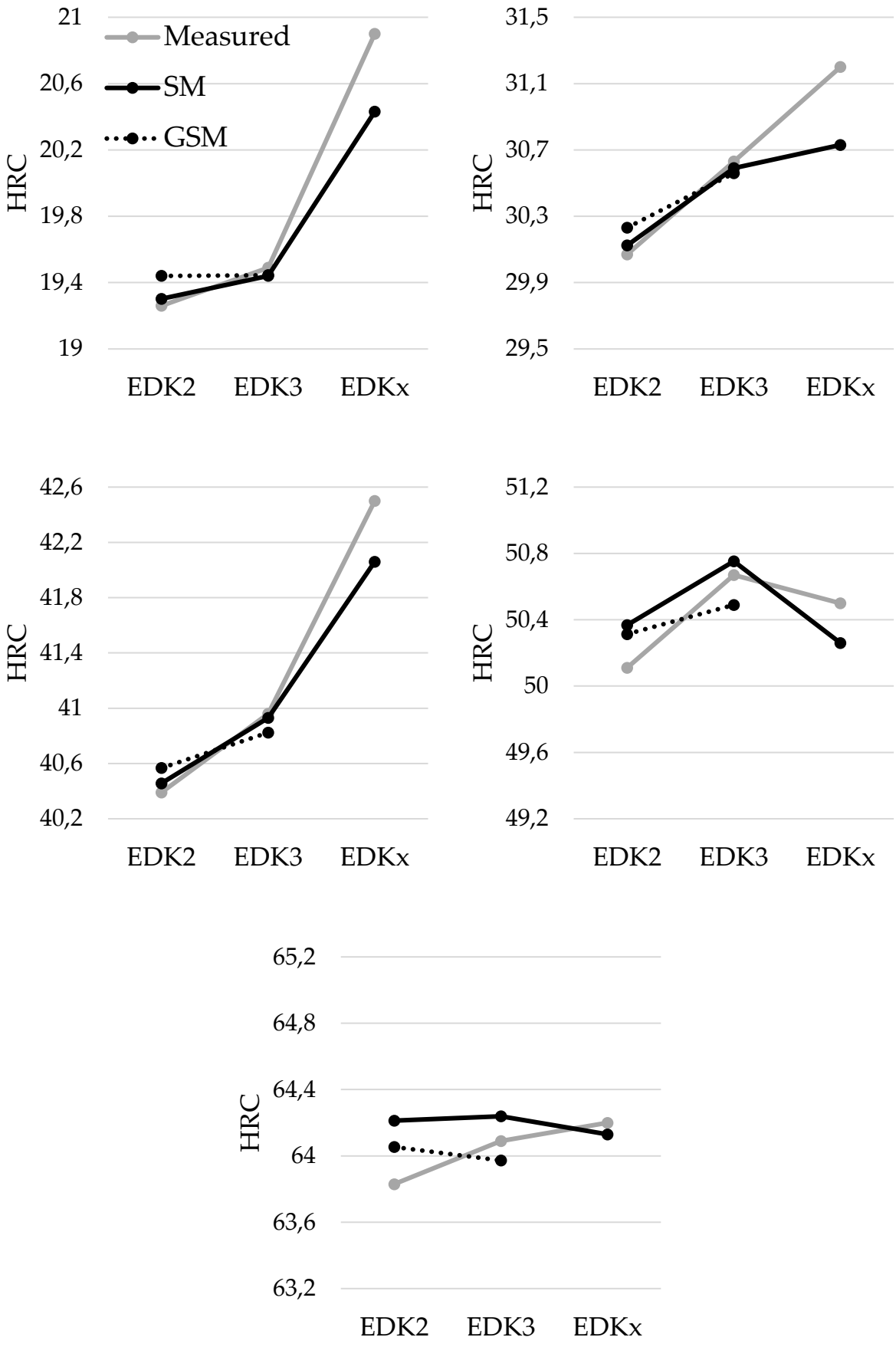

Figure 26: Hardness deviations arising from the deviations in the indenter geometry from the nominal values (gray: measured values, black line: corrected values using Schwenk method, black dotted line: corrected values using group standard method)

https://doi.org/10.7795/110.20250619

Firstly, it is clear that the application of any of the two correction methods improves the harmonization of the test results. In the case of the indenter EDKx, the corrected results move towards the PTB results for 20 HRC, 30 HRC, and 40 HRC hardness reference blocks, thereby reducing the large gap between the measured hardness values. Unfortunately, this reduction does not appear to be sufficient. As mentioned previously, the measurements were performed on different hardness reference blocks having the same nominal value. This, along with the differences in the measuring instrument, could justify the remainder in the hardness deviation. Nonetheless, an excellent agreement after the corrections is seen for the 65 HRC block. This could be understood in light of the skewed effect variations in test cycle parameters such as hold time have on softer materials. Additionally, the hardness of harder materials tends to be more stable over long periods of time. They also have lower non-uniformity of hardness across their surface and are far less prone to hardening with the increase in the number of indentations on them [71]. Perhaps the most plausible explanation for the higher variation in softer hardness reference blocks is the sensitivity of the Schwenk's method towards the input value of the opening angle and the accuracy of its measurement.

Nevertheless, the standard deviation of the corrected hardness values for the combination of the three indenters is lower than the uncorrected hardness values for every test block. Also, the average of the largest difference for every test block between a PTB indenter and EDKx reduces by thirty percent.

Considering the PTB indenters solely, the average of the absolute difference for all the blocks reduces from 0.44 HRC to 0.30 HRC after the application of Schwenk's method, whereas it reduces to 0.17 HRC when the group standard method is applied. The best agreement between the corrected hardness values is obtained for the hardest block followed by the softest block for the Schwenk's method and vice versa for the group standard method. The performance of both methods is mediocre for medium hardness blocks. This could be ascribed to the lack of knowledge about the geometry of the transition zone. In addition, it is difficult to determine if the tested material belongs to the previously mentioned Case 2 or Case 3, which eventually leads to the mismatch of the corrected values.

In essence, Schwenk's method's greatest strength is the direct relation to the geometry of the indenter. The direction of correction can always be justified based on the physics of indentation. Furthermore, this method could be used for the determination of sensitivity coefficients for the estimation of measurement uncertainty according to GUM. A Monte-Carlo simulation can also be performed using the derived equations for the estimation of the measurement uncertainty. It could further be used to create a virtual device. Moreover, this modelling approach can be applied to other Rockwell hardness scales that use a spheroconical diamond indenter.

On the downside, this method is extremely cumbersome and requires laborious hardness measurements along with the topography measurements of the indenter and measurements of the diameter of the indentation. Although unlikely, changes in the

https://doi.org/10.7795/110.20250619

indenter shape would require the entire procedure to be repeated. Another drawback of this method is that it does not include the material properties of the indenter nor the sample. Other influencing factors on the HRC results, such as the indentation velocity or the holding time during the application of force, are also not considered in this method.

https://doi.org/10.7795/110.20250619

6. Calibration of the Spherical Tip Radius of Rockwell Hardness Diamond Indenters

This chapter deals with the calibration of the diamond spherical tip of Rockwell hardness testing indenters using confocal laser scanning microscopy. In the previous chapter, it has been shown that the geometric deviation of an indenter results in deviations in the calculated hardness values. The geometric deviation is also typically the largest contributor to the measurement uncertainty in hardness testing [72–74]. Some NMIs claim as much as 50 % of the total measurement uncertainty in Rockwell hardness testing arising from the uncertainty in the calibration of the radius of the Rockwell hardness diamond indenter [75]. For this reason, the relevant standards for the various hardness tests clearly define the indenter geometry and the permissible tolerances for deviations from the ideal shape, which are generally due to manufacturing difficulties or limitations, damage, or wear during daily usage. Thus, it is important to ensure that the geometric properties of the indenter are within the permissible tolerances and equally important to correct these minor deviations from the ideal shape so that they do not lead to mismeasurement of the hardness value.

A procedure known as tip area calibration is used in IIT to take into consideration the non-ideal shape of an indenter [7]. This is made possible since instrumented indentation hardness is defined in terms of the test force and the projected area of contact. Nevertheless, such calibrations are not possible in the case of Rockwell hardness testing, as no geometric parameters are present in its definition. Numerous studies have employed empirical approaches [68], finite element methods [76], regression analysis [77] or a group standard of indenters [65] to get around this issue. Regardless, as demonstrated in the previous chapter, each of these methods relies on knowing the true radius of the indenter in order to account for the hardness deviations.

Indenter calibration can be accomplished via a variety of measuring instruments, as detailed by Germak et al. [78]. Li et al. [79] developed a custom-made, non-imaging optical device that uses confocal position sensing to measure the tip radius. The radius in this system is calibrated by measuring the relative shift of two confocal curves. Germak et al. [80] investigated the feasibility of calibrating the tip radius using a commercial confocal laser scanning microscope (CLSM) by evaluating the 2D axial profile sections of indenters. This approach shows great promise because it extracts the complete 3D geometry of the indenter in a simple and quick manner, reducing the overall calibration cost of an indenter. Additionally, a CLSM is a multifaceted instrument and can be utilized for other calibration tasks, making it a good return on investment for calibration laboratories in comparison to a dedicated instrument that can only measure the indenter’s radius.

Despite its advantages, a detailed study investigating the factors affecting a CLSM measurement must be undertaken, followed by the establishment of a traceability chain to the primary standards and the determination of the measurement uncertainty. Only then can reliable radii calibrations be performed with it.

https://doi.org/10.7795/110.20250619

6.1. Description of the measurand and the measuring instrument

The measurement of the regular Rockwell hardness value for the scales HRA, HRD, and HRC and the superficial Rockwell hardness value for the scales HR15N, HR30N, and HR45N is performed using a spheroconical diamond indenter. The standard [36] states that this indenter should have a tip radius of 200 µm and an opening angle of 120°. Figure 27 (a) illustrates the geometry of such an indenter, with the spherical region highlighted in red and the conical region highlighted in blue. For an ideal indenter, the blend point at which both these regions meet is located at a height of 26.8 µm from the apex of the indenter tip. An image of an indenter lying down and another indenter in an indenter holder, along with a coin for scale, is shown in Figure 27 (b).

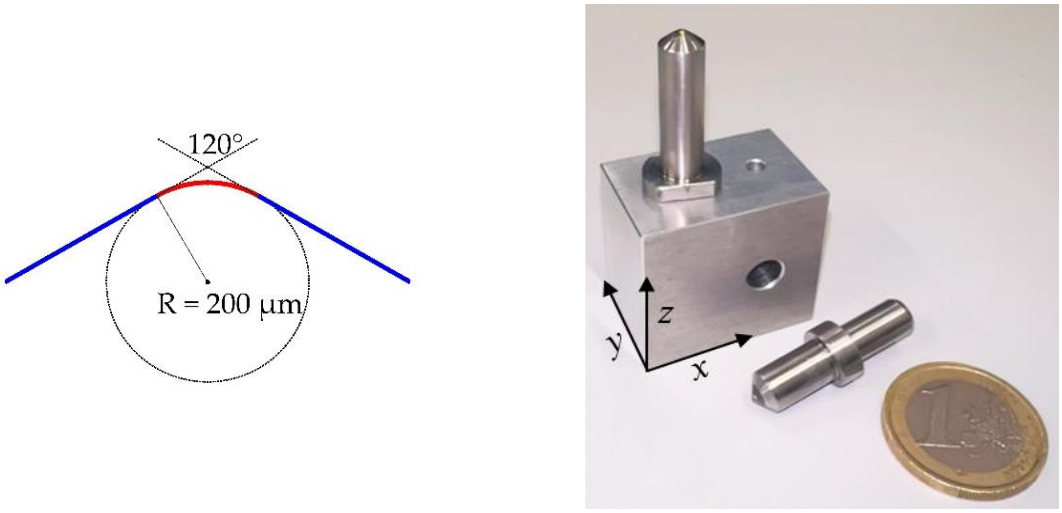

(a) (b)

Figure 27: (a) Front view of an ideal Rockwell diamond indenter geometry; (b) Image of an indenter lying down and an indenter in a holder

The standard [37] mandates that an indirect verification and a direct calibration of the indenter be carried out before performing hardness measurements with it. It is specified that the spherical and conical diamond surfaces must be defect-free and polished to a depth of 300 µm from the tip apex. A smooth transition from the sphere to the cone at the tangent is necessary and required.

Based on the application of the indenter, the tolerances vary. If the indenter is used for calibrating a hardness reference block, the mean radius must be within 195 µm and 205 µm and every single measurement of the radius must be within 200 µm ± 7 µm. For industrial or everyday use, the radius can range between 190 µm and 210 µm and every value must be within 200 µm ± 15 µm. Both calibration grade and working grade indenters should have a local deviation of the profile from the true radius of no more than 2 µm. In addition, it is necessary to perform hardness tests on hardness reference

https://doi.org/10.7795/110.20250619

blocks and compare the results with those obtained using calibration grade indenters to indirectly verify the performance of working grade indenters.

In this work, used Rockwell diamond indenters abbreviated as EDK (e.g. EDK1, EDK2, EDK3, etc.) are analyzed using an industrial CLSM that is commercially available and called CLSM-1. The indenter to be measured is placed inside an indenter holder (see Figure 27 (b)) and then cleaned thoroughly. Then, the indenter holder along with the indenter is placed on the *x-y* stage of the microscope. Using the camera function, it is seen if the surface is free from dirt and other contaminations. This is followed by the centering of the measurement object. During the calibration of an indenter, 8 measurements are generally performed. This is followed by rotating the measurand by 90°and performing 8 more measurements. The 8th measurement is chosen for the calculation of the tip radius.

The CLSM-1 instrument is housed inside an isolation chamber and the chamber sits on a passively damped pneumatic table, thereby minimizing the influence of environmental noise. The temperature in the laboratory in which the instrument is placed is (21.1 ± 0.2) °C. The operational principle of the instrument can be summarized as follows. The CLSM-1 takes several intensity images in equally spaced vertical focus steps. To generate an image for each z-focal position, a laser beam with a wavelength of λ = (405 ± 5) nm is scanned across the surface pixel by pixel. Two fixed pinholes along the beam provide confocality. At the receiver plane, only the "in-focus light path" produces the strongest peak. The height mathematically assigned to each pixel is derived from the intensity distribution per pixel across the vertical stack.

For most of the measurements, unless stated otherwise, a 50x objective lens with a numerical aperture (A_N) of 0.95 is used with a zoom factor of 1x. This guarantees that the entire spherical tip of the Rockwell diamond indenter and a small portion of the conical region are captured in a single measurement, eliminating the need for stitching of images. The number of pixels in the captured images is 1024 x 1024, which amounts to an image size of 256 µm x 256 µm, with a spatial sampling of 0.25 µm in both x- and y-axis. In this configuration, the height of the indenter from the tip is approximately 70 µm.

The vertical resolution of the instrument is below 10 nm. With a fine scanning measurement mode, a vertical stack distance of 60 nm is achieved, and a total of roughly 1.1 million data points are extracted per z-scan in about 7 minutes. The maximum detectable slope as stated by the manufacturer is 85 °. However, the maximum measurable slope of the 50x objective lens without selective intensity adjustment has been determined by [81, 95] to be 60°. Theoretically, in the case of a Rockwell indenter, the tilt angle of the surface varies from 0° at the tip apex up to 30° at the transition region to the cone (see Figure 27 (a)). These surface slopes are well within the measuring capacity of the instrument CLSM-1.

In addition to the color data and the 3D height data, the CLSM-1 also generates a combined 3D intensity image. Figures 28(a) and Figure 28 (b) illustrate the intensity

https://doi.org/10.7795/110.20250619

images of two Rockwell indenters, EDK4 and EDK5. The black marks observed in the images may be indicative of one or more of the following factors: the presence of dirt particles on the surface, defects resulting from abrasion, minor cracks in the diamond, or an absence of reliable surface data points in that region due to mismeasurement.

From the intensity images, the spherical and conical regions can be distinguished on the basis of the color contrast. It is of particular significance that the notable disparity in the characteristics, as exemplified by the near-spherical shape of the indenter in Figure 28 (a) and the four distinct edges on the indenter in Figure 28 (b), serves as a compelling indicator of the considerable difference between different indenters. This difference could be attributed to the orientation of the crystal axes during the mounting of the diamond into the indenter and the overall manufacturing and polishing process of the diamond indenter. It can be reasonably assumed that even if all other variables during a Rockwell hardness measurement are maintained, the measured hardness value would differ if these two indenters were employed [82].

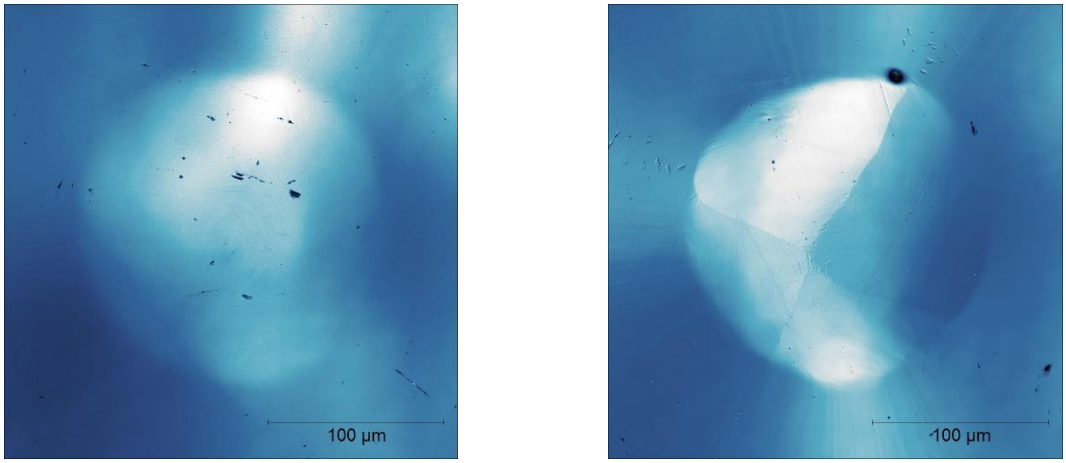

(a) (b)

Figure 28: (a) Intensity image of indenter EDK4; (b) Unexpected edge-like features on the intensity image of indenter EDK5

6.2. Spherical fit

The poor traceability in characterizing indenters stems not only from the type of measuring instrument used but also from the way the extracted data is evaluated [83]. Mathematically, there are multiple ways in which the radius can be determined. The standard [37, 38] does not explicitly prescribe a method to follow. In this work, a superior yet simple method to evaluate the measurement data of a Rockwell indenter topography is proposed.

The evaluation of the measured data of the geometry of an indenter, be it a point cloud of 3D coordinates or a 2D profile, is generally carried out by fitting a circle to singular

https://doi.org/10.7795/110.20250619

profiles to obtain the radius value. This procedure is carried out at four or eight equally spaced angles (0°, 22.5°, and so forth) in accordance with the specific application of the indenter (e.g.: working-grade or calibration-grade). In the novel approach presented here, the complete 3D point cloud of the indenter topography in the spherical region is employed for the calculation of the radius. Therefore, the measured radius is a better representative of the spherical tip of an indenter.

Beginning from the tip apex (h = 0 µm), the measurement data is evaluated in incremental cross-sections along the height axis (z-axis) until the blend point. The data from each section is fitted stepwise with a sphere to determine the center and the respective 3D cap radius. Figure 29 provides a schematic representation of this process. The collection of the radii from each section then yields an effective 3D radius plot with respect to the height h (R-h curve).

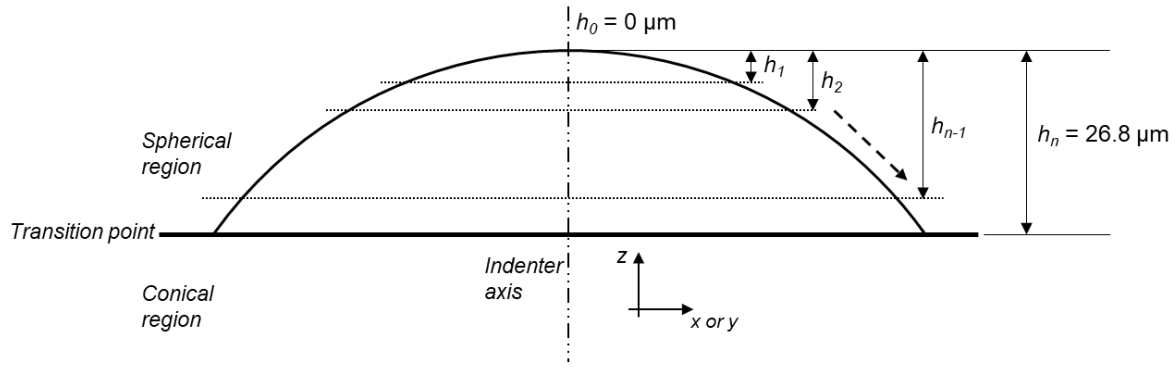

Figure 29: Proposed method of evaluating the 3D radius with respect to the height of the measured 3D spherical cap

During the sequential fitting process, the center of the fitted spheres is subject to shift due to the optical aberrations of the instrument and due to the quality of the measured sphere (deviation from the ideal sphere topography). These shifts are recorded and serve as an indicator that can be used to estimate the measurement uncertainty.

This procedure has been carried out for the indenters EDK1, EDK2, and EDK3, and the resulting R-h curves are presented in Figure 30. The nominal value of 200 µm and the location of the theoretical blend point are indicated on the graph. The R-h curves for three additional indenters (EDK6, EDK7, and EDK8) along with their intensity images are provided in the Appendix 4 and Appendix 5, respectively.

Similar to intensity images shown in Figure 28 (a) and Figure 28 (b), Figure 30 provides a compelling illustration of the distinct geometric characteristics exhibited by the indenters. At the outset of the R-h curve, the fitted 3D radii for the indenters EDK1 and EDK2 are less than the standard requirement of 200 µm. In the case of the indenter EDK3, the fitted radii in the vicinity of the indenter tip apex are observed to exceed the nominal value. This suggests that the indenter EDK3 has a flatter tip in comparison to EDK1 and EDK2, which could be considered to be relatively sharper. The calculated

https://doi.org/10.7795/110.20250619

radii are found to be comparable between heights of 15 µm and 26.8 µm. Heights exceeding 26.8 µm are excluded as they lie in the region of the cone. In the case of nonideal indenters, the blend point is subject to variation, contingent on the true radius and true opening angle of the indenter in question. Heights below 3 µm have not been included in this analysis, given that the indenter surface at this height is in close proximity to the vertical axis and the available data points are insufficient for a reliable spherical fit.

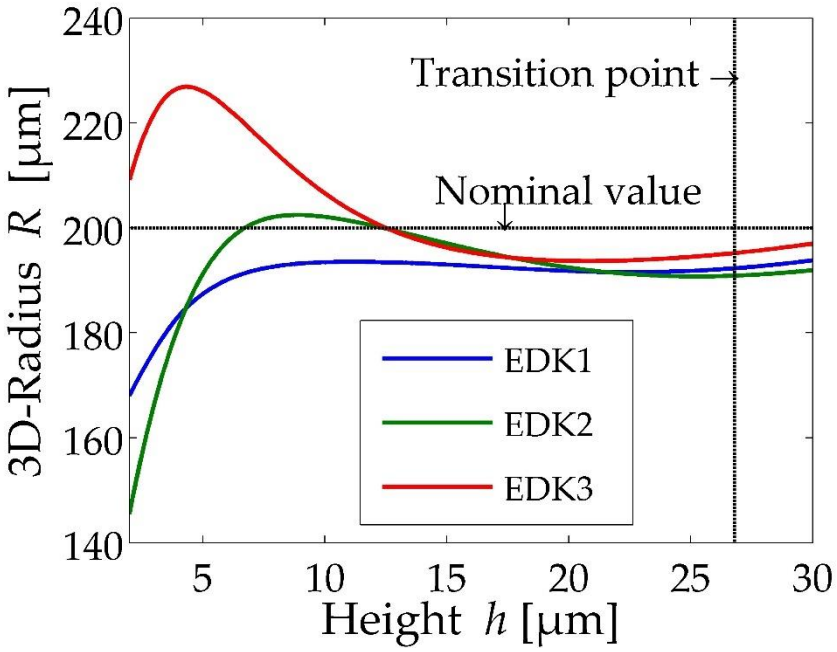

Figure 30: 3D radius vs. height for EDK1, EDK2, and EDK3

The principle of least-squares minimization, in which the residuals between the fit and the data are minimized, is typically the method of choice for fitting a sphere to a 3D data set [84]. Although methods such as minimum zone sphere, maximum inscribed sphere, and minimum circumscribed sphere do exist, they are not the focus of this work and therefore will not be discussed further. In this study, a particular form of linearization is employed in place of non-linear least squares techniques. Following is a brief derivation of the evaluation.

In a Cartesian coordinate system, a sphere of radius *R* centered at (x_c, y_c, z_c), with data points on its surface at coordinates *(x, y, z)* is given by the Equation 38.

$$(x - x_c)^2 + (y - y_c)^2 + (z - z_c)^2 = R^2 \qquad \textbf{Equation 38}$$

Following a topography measurement, the coordinates *x*, *y*, and *z* are known. Regrouping and expanding the above equation gives Equation 39.

https://doi.org/10.7795/110.20250619

$$(x_c^2 + y_c^2 + z_c^2 - R^2) - 2xx_c - 2yy_c - 2zz_c = -(x^2 + y^2 + z^2) \quad \textbf{Equation 39}$$

Let $d = x_c^2 + y_c^2 + z_c^2 - R^2$ and $B = -(x^2 + y^2 + z^2)$.

Equation 39 can be simplified, as shown below in Equation 40.

$$-2xx_c - 2yy_c - 2zz_c + d = B \quad \textbf{Equation 40}$$

In matrix form, this equation can be denoted using Equation 41.

$$\begin{bmatrix} -2x & -2y & -2z & 1 \end{bmatrix} \begin{bmatrix} x_c \\ y_c \\ z_c \\ d \end{bmatrix} = B \quad \textbf{Equation 41}$$

Equation 41 is of the form $AX = B$, and can be solved as a set of linear equations for every data point to determine the center and radius of the sphere. A minimum of four data points is required to apply this method of fit. A comprehensive account of this linearization method can be found in [85]. This technique is most frequently employed to estimate the initial parameters for algorithms such as the Levenberg-Marquardt or Gauss-Newton algorithms. The use of an iterative method is precluded by the considerable number of data points associated with each sphere fit, as well as the number of fits that emerge from incremental stepwise evaluation increasing the computational time substantially. Furthermore, consistent results are obtained by the linearization method and in contrast to an iterative approach do not vary based on the number of iterations or the input value of the initial fit parameters. Nonetheless, to select the most appropriate algorithm in the instance of an indenter, a comprehensive investigation is still essential. An initial investigation demonstrated that the outcomes of this method are satisfactory and comparable to those obtained through iterative methods.

Moreover, this algorithm has been tested for artificially generated data sets of an ideal sphere of radii 200 µm with data points ranging from a thousand to a million. For every data set, the fit determines the exact radius value of 200 µm. In view of the potential for CLSM-1 measurement data to include some degree of noise, synthetic noise is incorporated into the data set of an ideal sphere with the software Gwyddion [86]. Figure 31 shows the close-up of a 2D profile of an ideal sphere with the addition of the noise signals using a gaussian distribution with root mean square (RMS) values of 0.1 µm, 0.5 µm and 1 µm.

https://doi.org/10.7795/110.20250619

Taking the same approach as that detailed to obtain an R-h curve, followed by the subtraction of the ideal radius value of 200 µm from the fitted radii, generates a deviation plot over the height of the sphere. The deviation of the fitted radius is a mere 1 µm, even when the noise has an RMS value of 5 µm, which is a very promising result. The deviation decreases to 0.1 µm when the noise has an RMS value of 2.5 µm. The variance for lower RMS values of noise is in the nanometer range.

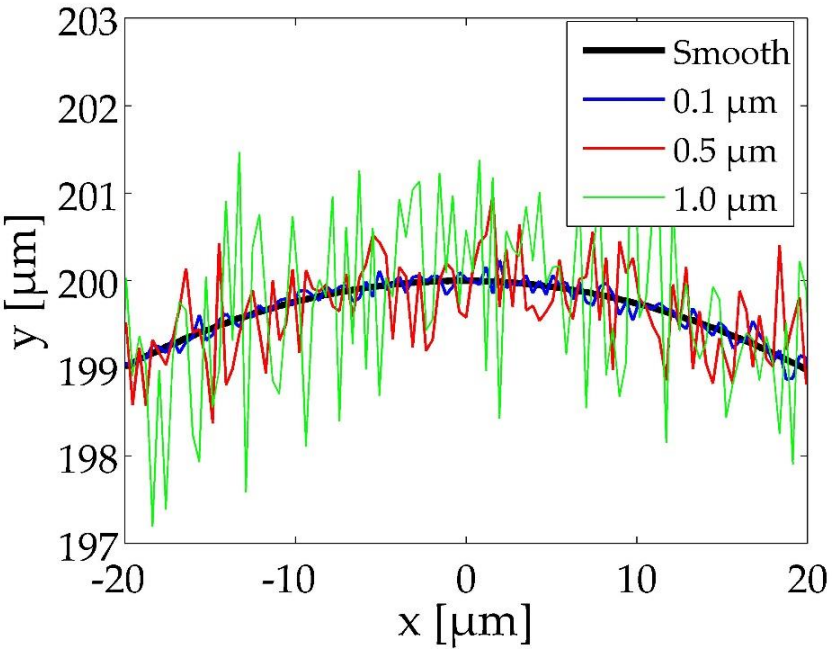

Figure 31: Close-up of a 2D profile of a hemisphere of radius 200 µm with synthetic noise (black: 2D profile without noise, blue: noise of 0.1 µm, red: noise of 0.5 µm, green: noise of 1.0 µm)

Given that the Rockwell indenter's transition point lies below 30 µm, a more detailed examination of the radii deviation in this height range is provided in Figure 32. The fit is found to be effective up to an RMS noise level of 0.1 µm. A minor deviation of approximately 0.5 µm is observed at the outset of this curve, which then dies down above a height of 10 µm.

https://doi.org/10.7795/110.20250619

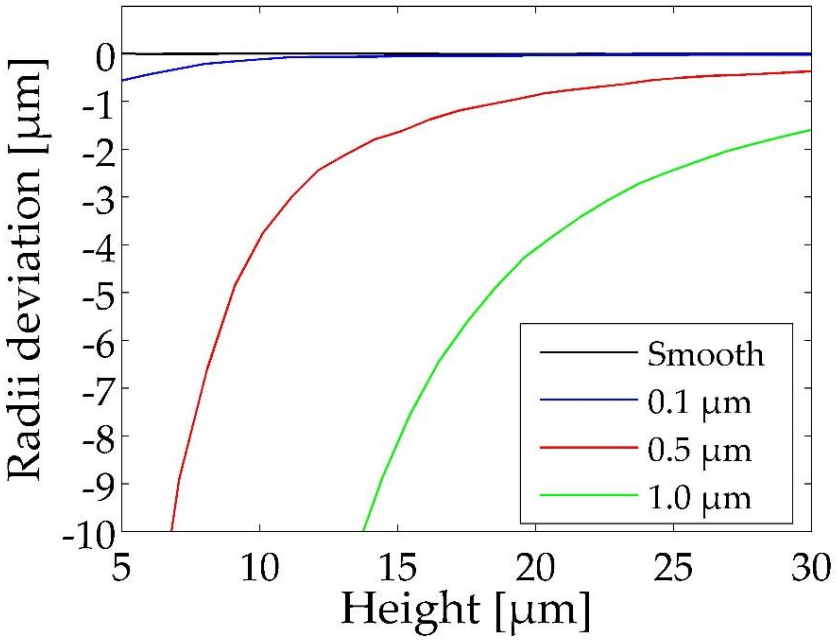

Figure 32: Radii deviation vs. height plot for noisy data

For noisy data beyond an RMS value of 0.1 µm, the fitted radii exhibit a convergence to the true radius value with increasing height. However, deviations up to 0.5 µm at smaller heights are observed. It is important to note that such significant discrepancies amounting to tens of micrometers arising due to the combination of noise and fitting algorithm can be misleading when comparing results obtained through different measurement instruments. One possible way to mitigate the impact of noisy data is to employ filtering techniques. On the negative side, this increases the number of post-processing steps. Therefore, it has been deliberately excluded in this work.

Moreover, user experience indicates that CLSM-1 images of smooth surfaces sometimes show randomly positioned singular points above the surface, such as that shown in Figure 33 (a). These outliers result from erroneous data acquisition as opposed to instrument noise. It is recommended that this is left untreated because the abundance of data points eventually diminishes the influence of these singular points on the fit. However, it is essential to ensure that the highest point of the measurement data is on the surface of the measurand and not above it, as is the case illustrated in Figure 33 (b). This is critical, as the chosen algorithm commences the fit from the highest point of the data. Other moderately noisy images can be treated with a median filter, which did not affect the fitted radius.

https://doi.org/10.7795/110.20250619

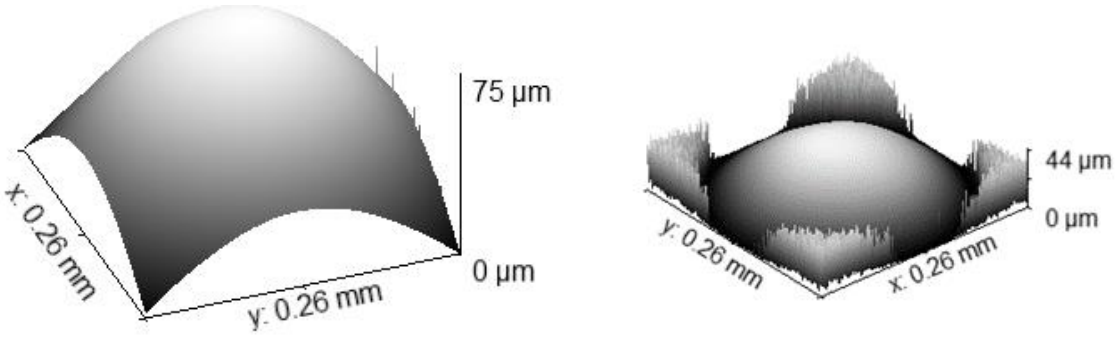

(a) (b)

Figure 33: (a) CLSM-1 height image with singular points over its surface; (b) CLSM-1 height image with noisy edges

6.3. Evaluating a 2D profile vs. 3D point cloud

To enable a systematic comparison between the conventional method of evaluation and the method proposed in this work, eight distinctive and equidistant axial 2D profiles from the CLSM-1 measurement data of three indenters (EDK1, EDK2, and EDK3) are extracted. Figure 34 depicts an image of indenter EDK2 with its 2D profiles. A circle is fitted to each of these profiles for the individual indenters by considering the height data from the indenter tip apex until the blend point (h = 26.8 µm). Similar height data is used to perform a 3D sphere fit on the same measurement data. The results of fitted radii, the mean, and the standard deviation are presented in Table 6.

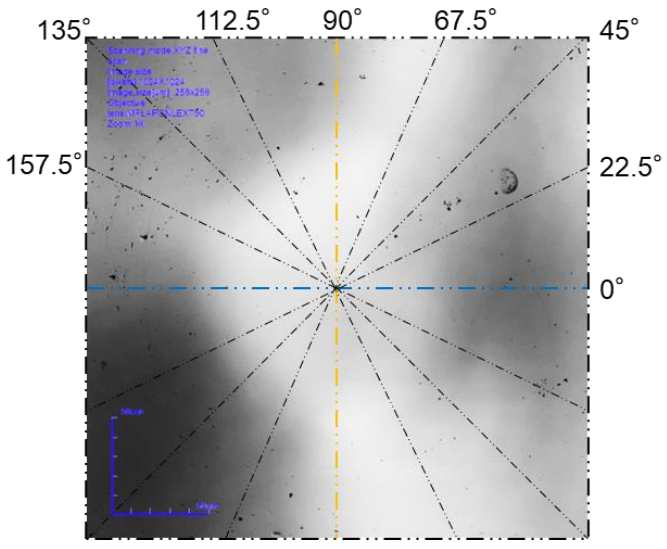

Figure 34: 2D profile-based conventional method of measuring the radius of a Rockwell diamond indenter

https://doi.org/10.7795/110.20250619

Indenters / Profiles	EDK1	EDK2	EDK3
0°	190.51	189.22	195.33
22.5°	192.67	186.20	197.23
45°	192.22	188.43	196.80
67.5°	189.28	193.02	193.86
90°	188.43	191.85	193.39
112.5°	190.95	190.12	194.97
135°	192.20	191.49	198.13
157.5°	191.35	194.66	196.07
Mean of 2D-Radius	**190.95**	**190.62**	**195.72**
Standard deviation of 2D-Radius	1.49	2.69	1.65
3D-Radius	**192.30**	**190.89**	**195.22**

Table 6: 2D radius evaluation of profiles of three indenters in comparison to 3D radii (radii values are in µm)

The 2D mean radius values for EDK1 and EDK2 are 1.35 µm and 0.27 µm smaller than the true 3D radius, respectively, while EDK3 shows a value that is 0.5 µm greater. A discrepancy of 1 µm in the radius measurement can alter the probability of an indenter meeting or failing the criteria of a calibration grade indenter by 10%. Therefore, it can be inferred that 8 profiles are not always sufficient to obtain an accurate estimation of the true radius of the spherical tip. This effect could become more pronounced for working grade indenters, given that the mean value is based on only 4 profiles.

This effect can be clearly seen for the two orthogonal profiles (0° and 90°) of the indenter EDK2 (see Figure 35). It can be observed that there is a notable discrepancy between the top section of the 0° profile and the 90° profile, which ultimately leads to the difference of 2.6 µm in the fitted radii. The residuals of the fit are within the permitted local deviation limit of 2 µm. The magnitude of the form errors for indenters EDK1 and EDK3 are also of similar order.

https://doi.org/10.7795/110.20250619

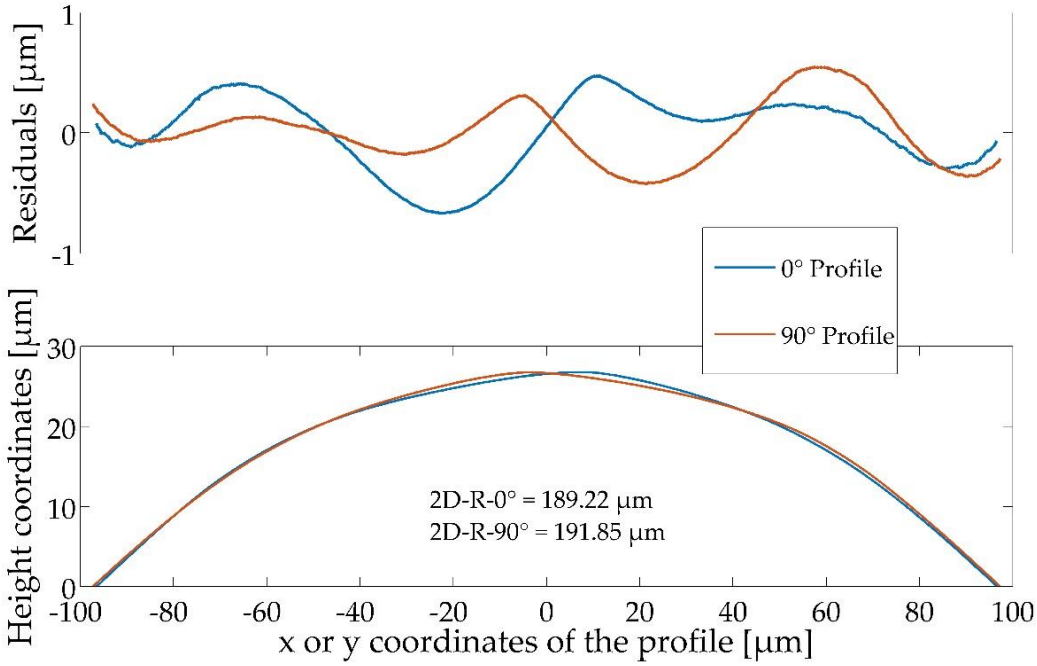

Figure 35: 0° and 90° profiles of indenter EDK2 and the residuals of the circle fit

Along with the Rockwell indenters, a well-polished ruby sphere is also measured with the instrument CLSM-1 and evaluated in a similar fashion to the indenter to compare the form errors. The 2D profiles and the residuals are shown in Figure 36. The residual plot for both the 0° and 90° profiles is nearly flat, with only a few minor spikes likely caused by surface irregularities.

In Mohs scale, diamond has a hardness of 10, whereas ruby a value of 9. However, this does not justify the stark contrast in the peaks and valleys as seen in Figure 35 and Figure 36, implying the indenters need to be polished better. To highlight the possibility of a better finished product, a diamond spheroconical indenter, which is used to perform nanoindentation, is analyzed in a similar fashion. This indenter has a nominal radius of 100 µm and an opening angle of 120°. Figure 37 shows the 2D profile of this indenter and the residuals of the fit.

https://doi.org/10.7795/110.20250619

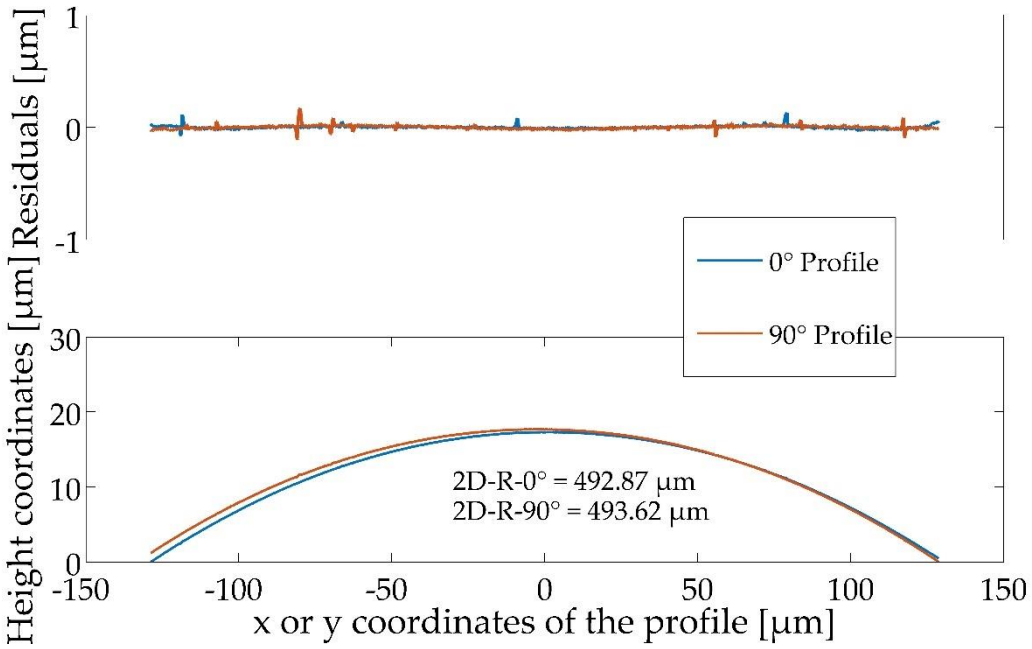

Figure 36: 0° and 90° profiles of a calibrated sphere and the residuals of the circle fit

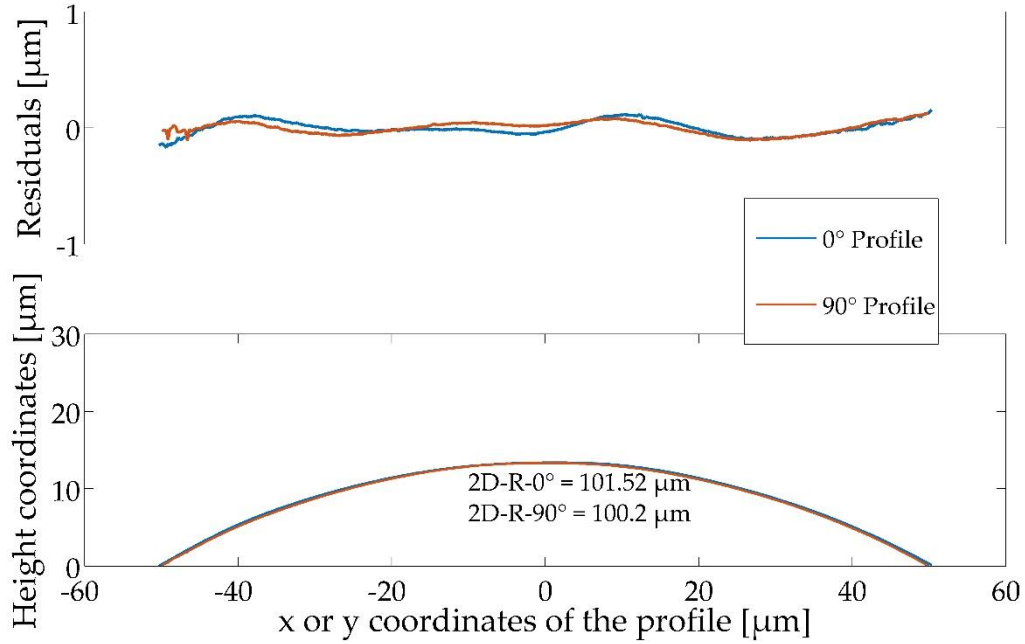

Figure 37: 0° and 90° profiles of a spheroconical diamond indenter used to perform nanoindentations and the residuals of the circle fit

The residuals shown in Figure 37 exhibit minimal variation, with peaks and valleys within 0.2 µm, indicating superior polishing of this indenter. Although a smaller indenter is more difficult to manufacture, the overall form deviation of the indenter used to perform nanoindentations is approximately five times smaller than that observed for the

https://doi.org/10.7795/110.20250619

indenter EDK2. Consequently, it can be stated that the local deviation from the true radius permitted by the standard for Rockwell indenters is significantly larger than the attainable local deviation. Restricting this tolerance would enhance the overall comparability of a Rockwell hardness test.

An important aspect to consider during the extraction of the 2D profiles is the determination of the highest point on the surface. During a CLSM measurement, the image is centered with the help of the largest fully measurable diameter of the geometry within the respective field of view of the objective lens. In an ideal geometry, the midpoint of the image would be the highest point on the surface. However, here it was often observed that the highest point of the geometry is at an offset from the image center. Therefore, the 2D profiles need to be extracted through this point and not the image center. It must also be stated that it is assumed that the tip of the indenter is in line with the vertical axis of the indenter.

6.4. Window size effect

The results of both the conventional method of evaluation and the proposed method of evaluation in the previous section take into consideration a height of 26.8 µm from the tip apex of the indenter which corresponds to a cross-sectional diameter of 200 µm in an ideal indenter. However, the standard [38] states that the region between the cross-sectional diameter of 180 µm and 220 µm should not be considered for both the radius and the angle measurement to avoid including the blending region. The permissible window sizes for the evaluation of the radii are ± 40 µm, ± 60 µm or ± 80 µm. The selection of the window size is at the discretion of the calibration agency. The corresponding heights of the indenters from the tip apex at these window sizes assuming an ideal spheroconical geometry are approximately 4.0 µm, 9.2 µm and 16.7 µm respectively. Figure 38 exhibits the window sizes and their respective heights.

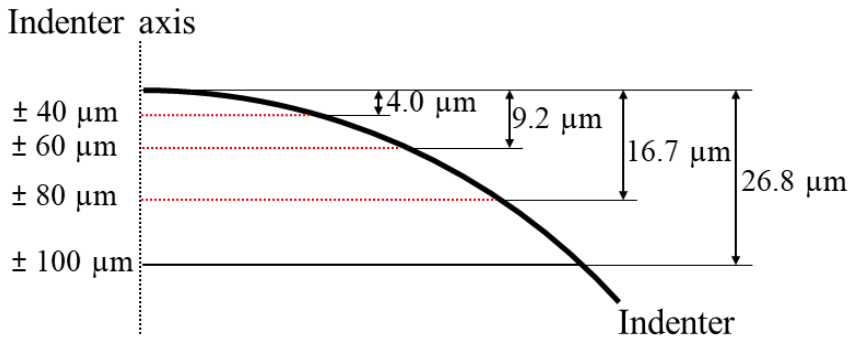

Figure 38: Schematic representation of the window sizes for radii evaluation and the respective indenter heights

The effect of the choice of the window size on the calibration of the radius is reviewed by applying the proposed 3D point cloud evaluation method on the indenters EDK4 and EDK5. Figure 39 presents the R-h curves for the aforementioned indenters. The

https://doi.org/10.7795/110.20250619

red lines in the figure represent the heights of the window sizes, whereas the transition zone or blending region as defined by the standard [37] is shaded grey. As with the intensity images, the contrasting shapes of the indenters are readily apparent upon initial observation of the R-h curves, particularly at lower heights. The radius of the indenter EDK4 near the tip apex is much larger than that of the indenter EDK5, reinforcing the sharpness of the indenter EDK5 as seen in the intensity images. With progressing height, the radii of the indenters intersect at window sizes ± 60 µm and ± 80 µm and are close to the perfect radius value of 200 µm. Hence, it is highly plausible that both of these indenters would be calibrated to have the same radii value, despite the stark differences in their geometric shapes. Least to say, this finding is very odd and unlikely to be serendipitous. Inevitably, the comparability of the measurement results suffers because the focus is solely on the conformity to the standard.

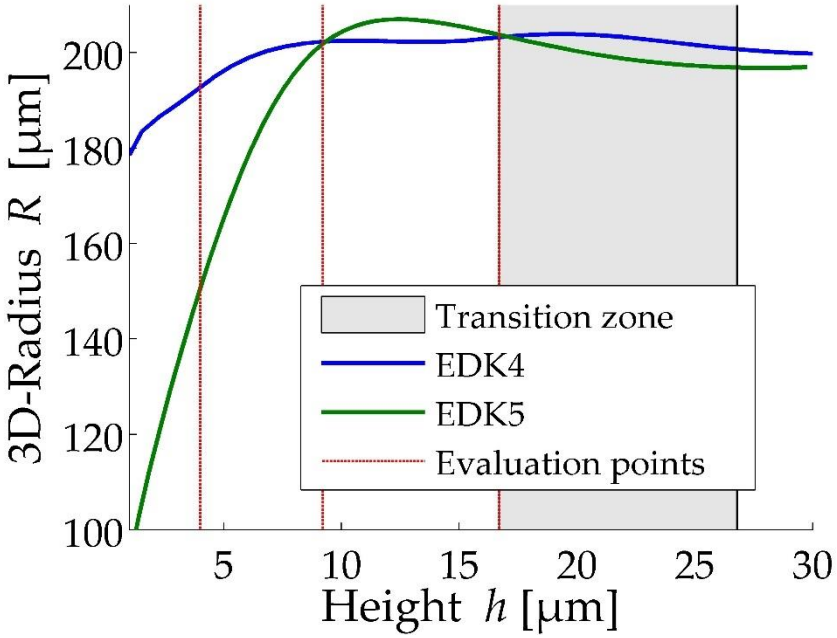

Figure 39: 3D radius vs. height curves for two different indenters

Previous studies [82, 87, 88] have demonstrated that indenters with the same tip radius and opening angle value may yield disparate hardness measurements when form errors such as those observed here are present. Thus, it is more suitable to calibrate the radius over a range of heights, and the window size used for the evaluation needs to be explicitly mentioned in the calibration certificate. Moreover, emphasis should be placed on the behavior of the radius between the window sizes and not just at its value at the window sizes. Additionally, window sizes greater than ± 90 µm may also be considered, as the radii at these heights have been observed to be stable with no discontinuities being observed in the R-h curves.

There are many advantages to analyzing the topography of the spherical region using an R-h curve. Firstly, the development of the indenter radius from the time of contact

https://doi.org/10.7795/110.20250619

during an indentation process up until its completion can be elucidated with greater precision, rather than restricting the spherical region of the indenter to a single value of radius, as is the case with the majority of the calibration certificates currently. Secondly, a deeper understanding of the spherical region can be gained, encompassing aspects such as the tip sharpness or bluntness and the type of diamond crystal used. Finally, enumerating the methods through which the evaluation has been carried out assists and encourages comparability of results. Unfortunately, the details pertaining to the type of fit, the evaluation algorithm, or the window size are rarely found in the literature. This is to the detriment of the wider material testing community.

6.5. Comparison of radii obtained from tactile and optical method

Thus far in this study, the measurement data obtained from the CLSM-1 instrument have been taken at face value. In this section, a systematic comparison between the measurement results of CLSM-1 and a traceable stylus instrument is undertaken. The reference measurements for the verification are given by the high-resolution topographic scanner (HRTS). A frequent comparison and verification of the performance of tactile instruments is carried out using various material measures, such as roughness standards, depth-setting standards, and calibrated spheres. This increases the metrological credibility of the reference measurement used in this study.

In light of the variations in the operational principles of CLSM-1 and the reference measurement from HRTS, a conscious initiative has been undertaken to enhance the comparability of the measurements. To guarantee that the diamond indenters remain unaltered in terms of their geometry and volume, no hardness tests are conducted prior to and between their topographical measurements. To prevent sample tilt, the same indenter holder is utilized for both CLSM-1 and HRTS measurements. The indenters and the indenter holder are stored in the laboratory for an adequate period of time before performing the measurements to ensure a temperature equilibrium in the test samples.

A raster scanning style with the same pixel size, measurement area, and sampling distance is selected for both instruments unless otherwise specified. The most crucial step is the erosion of the stylus tip of the HRTS from the raw data, which is achieved by using the known geometric properties of the stylus tip. Only after this process is complete can the two measurement results be compared.

The first set of measurements is performed on the indenters EDK1, EDK2, and EDK3. The R-h curves obtained from CLSM-1 and HRTS measurements using the proposed 3D point cloud-based method are presented in Figure 40. Upon cursory examination, the overall shape of the R-h curves for the respective indenters from the two measurement methods appears to be similar for the entire height range.

https://doi.org/10.7795/110.20250619

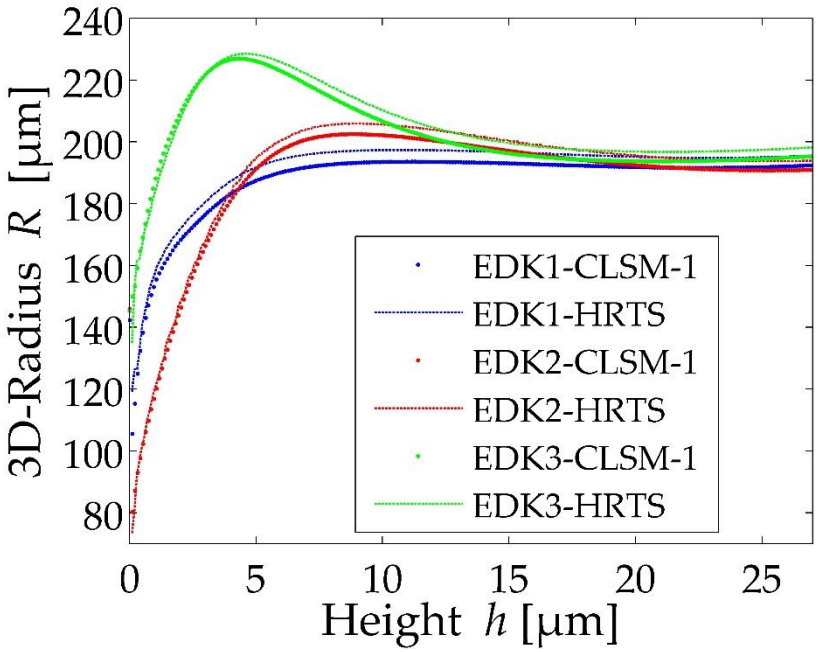

Figure 40: R-h curves for indenters EDK1, EDK2 and EDK3 obtained from HRTS and CLSM-1 measurements

However, upon closer inspection, it becomes manifest that the CLSM-1 and HRTS results are offset from each other. In the vicinity of the indenter apex, no discernible distinction is evident between the observed measurement outcomes. At larger heights, it becomes evident that the radii measured by CLSM-1 are consistently smaller in magnitude than those determined by HRTS.

To facilitate the absolute subtraction of the measured radii obtained from the two measurement instruments at the same heights, the evaluation program is modified. The stepwise fitting of the point cloud data obtained from CLSM-1 is performed by utilizing the array of heights at which the HRTS evaluate the 3D radii. The outcome of this procedure results in a deviation plot of the measured radii with respect to the indenter height, as shown in Figure 41.

The deviations for the three indenters are irregular until they reach a height of 6 µm, exhibiting no discernible trend. Beyond a height of 6 µm, the deviations appear to stabilize and converge. The variation in deviation for each indenter also reduces beyond this height. Additionally, a slight upward trend in the deviations with progressing height is observed. It is noteworthy that the CLSM-1 measures the radii for each indenter to be approximately 3 µm smaller than the reference HRTS at heights where the indenter is conventionally calibrated.

Further observations from Figure 41 indicate a large deviation in the radii of indenter EDK3 at lower heights. This may be attributed to the indenter EDK3 possessing a flatter tip in comparison to the other two indenters. It is also observed that the deviation plot of the indenter EDK2 is not a smooth curve. This is due to the mismatch of the

https://doi.org/10.7795/110.20250619

number of data points in the measurement data of the HRTS and CLSM-1. The distance between the data points in *x* and *y* directions for this indenter is 1 µm for the HRTS measurement and 0.25 µm for the CLSM-1 measurement, consequently resulting in the sawtooth pattern on the R-h curve.

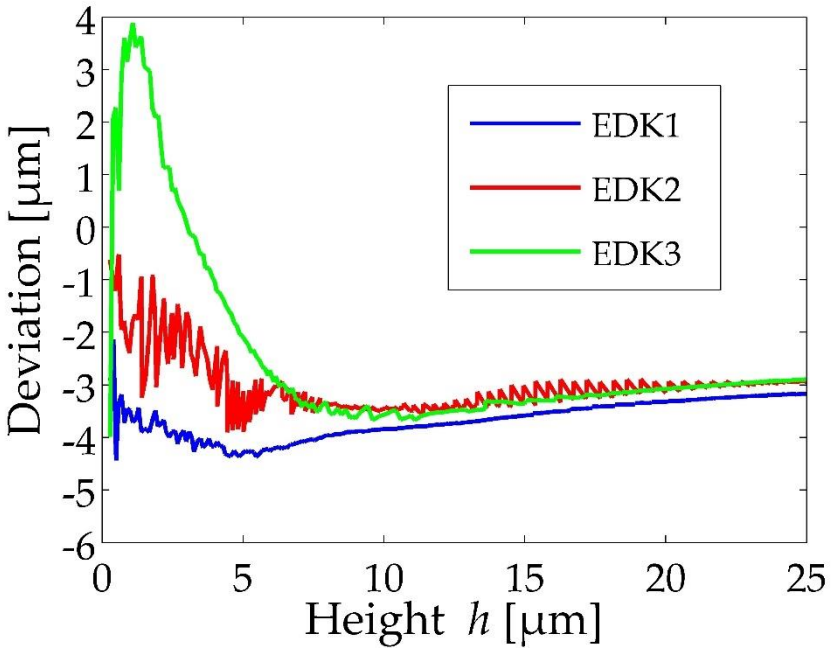

Figure 41: Deviation of the 3D-radii measured using CLSM-1 from the reference instrument HRTS for indenters EDK1, EDK2 and EDK3

The deviation of the measured radii using CLSM-1 from the reference value is significant and must be accounted for. Based on the similar trend observed for each of the indenters in the deviation curves, it is hypothesized that the cause of the deviation is due to an offset error resulting from the form measurement of the CLSM-1. The minor differences in the observed trends of the deviation curves could be arising from the different geometric properties of the indenters.

To test this hypothesis, calibrated high quality spheres with radii of 150 µm and 500 µm are measured using the CLSM-1 instrument. The difference between the measured radii and the nominal values at a height of 25 µm from the tip apex is found to be 1.7 µm and 7.5 µm respectively. The deviation is proportional to the size of the measured sphere. The larger the radius of the sphere, the greater the deviation in the measured radii.

A review of the literature reveals that confocal microscopes are generally prone to erroneous measurements when measuring objects such as spheres, whose surface slopes change constantly across the field of view [89]. By performing topographic measurements on spheres of varying radii using a 20x objective lens of a confocal microscope, a constant offset of 1.22 % from the reference value is reported by [90]. Conversely, the results obtained from CLSM-1 are lower than the reference values and

https://doi.org/10.7795/110.20250619

moreover exhibit a size-dependent deviation. Given the significance, the influence of the size of the measurand is studied in detail in the following subsection.

In an attempt to investigate the differences between the reference HRTS and the CLSM-1 measurements, the following analysis is performed. Firstly, the HRTS data of the indenter EDK1 is resampled in a way that it matches the CLSM-1 data set. Then, using the features on the indenter, the CLSM-1 data is rotated and mirrored. To undertake a sub-pixel position adjustment, a cross-correlation algorithm is implemented, followed by the point-by-point subtraction of the data points of the two measurements. A visualization of the arithmetic difference of the images is provided in Figure 42 along with the height difference of a singular horizontal profile.

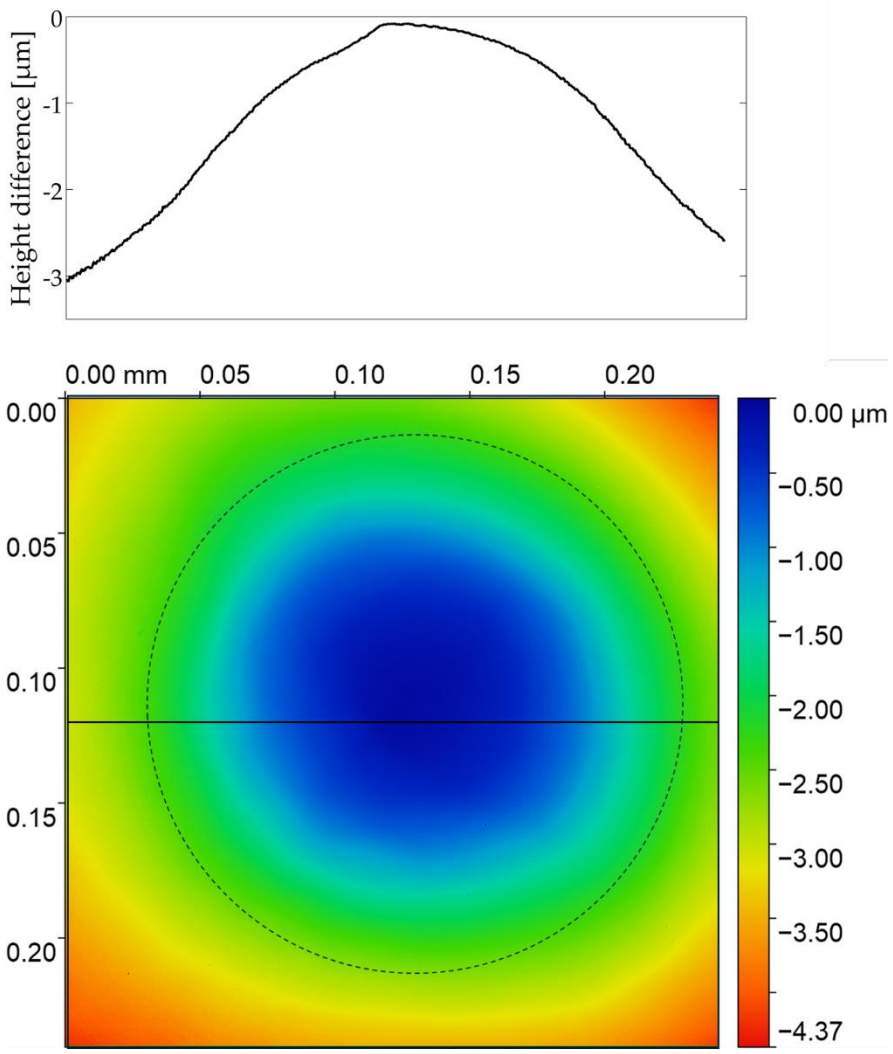

Figure 42: Height deviation plot across the surface and a height difference plot for an individual profile between the CLSM-1 and HRTS measurements for the indenter EDK1

Indicated by the blue color in Figure 42, the least amount of error in the height measurement of the CLSM-1 is observed at the center of the image, which corresponds to the tip apex of the indenter. The dashed circle in the figure outlines the approximate

https://doi.org/10.7795/110.20250619

location of the spherical region of the indenter EDK1. The flow of the color gradient is smooth and outwardly from the center to the boundaries of the image in a concentric circular pattern, indicating that the error increases as the local surface slope increases. Thus, it can be assumed that the deviation in the measured radius by CLSM-1 pertains to the error in the height measurement caused by optical aberration in the instrument.

To gain a deeper understanding of the observed deviation, three additional commercially available confocal microscopes (CM) at the PTB are used to extract the topography of the indenter EDK2 and measure its radius. The respective 50x objective lens of each CM is used to perform the measurements.

The instrument CLSM-2 is from the same manufacturer as the instrument CLSM-1, but they are different models. The numerical aperture of the instruments CLSM-1 and CLSM-2 is 0.95, whereas the instruments CM-3 and CM-4 have a numerical aperture of 0.8 for their 50x objective lenses. The instrument CM-3 is a spinning disc CM. On the other hand, the operation principle of the instrument CM-4 is based on structured light illumination. Before the commencement of the measurements, it is ensured that the instruments are operational and in a basic calibrated state with regards to the lateral and vertical axes. The deviation of the computed radii from the reference values of the HRTS as a function of the height is plotted in Figure 43 (see Appendix 6 for the results of indenters EDK1, EDK2, and EDK3 using CLSM-1 and CM-3). It is evident that each instrument measures the radii differently at different heights compared to the reference value. The similar shape of all the deviation curves could be ascribed to the reference measurement from HRTS.

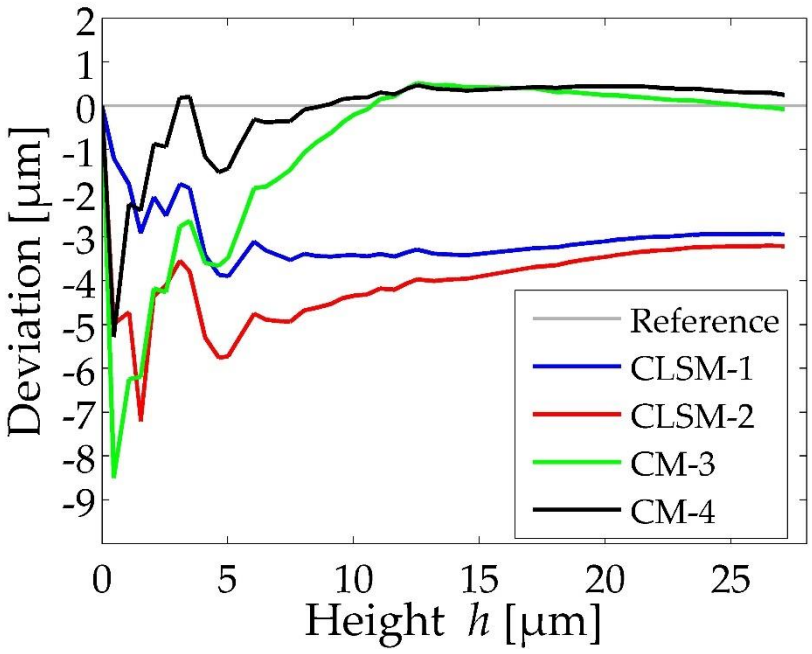

Figure 43: Deviation plot of the measured radii from the reference instrument HRTS using different confocal microscopes

https://doi.org/10.7795/110.20250619

Deviations from the tip apex up to a height of 5 µm are distributed randomly and do not follow a discernible pattern. Beyond a height of 5 µm, the deviations flatten out and approach a fairly constant value for all instruments. The radii measured by CM-3 exhibit both the largest and least absolute deviations from the reference values at heights proximate to the indenter tip apex and the blend point, respectively. This may be attributed to the acquisition of the indenter topography with 50% fewer pixels in comparison to the other instruments, which could subsequently result in a change in height data within every pixel.

Furthermore, it is anticipated that the deviation curves obtained from the instruments CLSM-1 and CLSM-2 would be very similar since they are of the same make. Although the deviations are in close proximity to each other, their deviation curves do not intersect. The dissimilarity between the two could be attributed to the distinct aberration of the instruments, as evidenced by the scanning of marginally different *x* and *y* positions and the scanning of facing and averted surfaces.

Since this work focuses on applied metrology, further investigations are restricted to the correction of the deviation from the reference value by studying the factors affecting the CLSM-1 measurement exclusively and creating a measurement uncertainty budget. The determination of the physical cause behind the deviation is beyond the scope of this study. The method of correction of the deviation for CLSM-1 can be easily transferred to other instruments. While the underlying causes of the deviation have been discussed here, they remain inconclusive due to the diverse operational principles inherent to a CM. Moreover, the intricate inner workings of commercial instruments, which often involve proprietary technologies, render them challenging to fully comprehend.

6.6. Factors affecting confocal microscope measurements

To investigate the sources of error in the CLSM-1 measurement of the tip radius of the Rockwell hardness diamond indenter and to explore the limits and capabilities of the CLSM-1, further measurements and analyses are carried out. Henceforth, the instrument CLSM-1 is referred to as CLSM. In addition to Rockwell diamond indenters, optically smooth precision spheres made of ruby are used as measurands to investigate certain factors affecting the CLSM. The reasoning behind this is that indenters inherently possess form deviations, which could lead to exaggeration or underestimation of the factors under investigation. Naturally, the acquired knowledge about the factors is transferrable to Rockwell diamond indenters.

The ruby spheres used in this study are mounted on a shaft and embedded into a sample holder. Figure 44 shows an image of one of these samples designated as PTB2. From left to right, the spheres are arranged in descending order of size. The nominal radii of the spheres are 1000 µm, 500 µm, 350 µm, 250 µm, 200 µm, 150 µm, 125 µm and 60 µm. The nomenclature assigned to each of the spheres in this study is based on their nominal diameter (e.g.: D2000, D1000, and so forth).

https://doi.org/10.7795/110.20250619

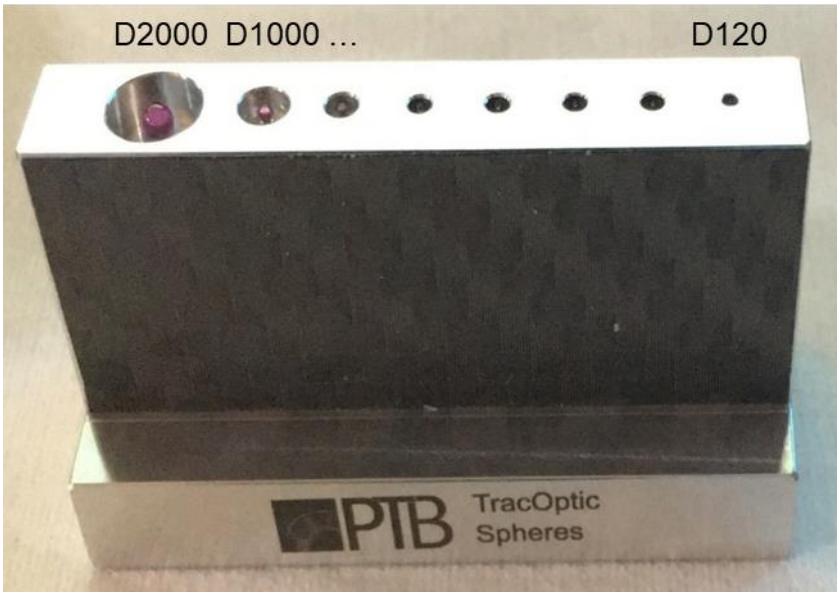

Figure 44: Image of the sample PTB2 containing ruby spheres of varying radii

6.6.1. Instrument calibration

Basic calibration of any instrument is paramount to obtaining meaningful and comparable results. Typically, individual axes are calibrated using lateral and height standards to correct for geometric errors. The lateral calibration of the CLSM is carried out with the help of a lithographic cross-grid and a 3D landmark-based calibration standard called the Ritter pyramid [91]. This 3D pyramidal calibration artefact consists of multiple reference marks on the x-y plane and on the stepped pyramids. All three axes can be calibrated simultaneously by the optical detection of these markers in a single measurement. Furthermore, this artefact facilitates the correction of shearing between the coordinate axes. Both the flatness and the residual flatness error for the CLSM instrument have also been accounted for [92].

The calibration of the Ritter pyramid itself is undertaken using PTB's metrological large-range AFM (Met. LR-AFM). This instrument has three laser interferometers for the measurement of position along each axis. Through the calibration of the optical frequency of these interferometers with the frequency standards of the PTB, the traceability to the definition of a meter is established [93].

A comprehensive uncertainty budget for the reference structure is unavailable and is still under active research. Besides this method, various other ways to calibrate a CLSM exist and have been described in [94].

6.6.2. Objective lens

Most optical instruments come with multiple objective lenses. Some that are fixed on a revolving nosepiece that can be changed with a click of a button, and some that need to be manually screwed into position. Likewise, the CLSM used in this study can acquire images in different magnifications. The numerical aperture, working distance,

https://doi.org/10.7795/110.20250619

magnification, size of the measurand, and optical aberrations are a few factors that must be considered before choosing an objective lens. For Rockwell hardness diamond indenters, the maximum height of the indenter that can be captured within the field of view by the objective lens is also decisive.

Neglecting the surface slopes arising due to roughness on the indenter, the surface slope of the Rockwell indenter at a macroscopic level varies from 0° at the tip apex up to 30° at the transition point. Therefore, a numerical aperture greater than 0.5 (sin 30°) is required for the acquisition of the surface topography of the indenter. The objective lenses available at the CLSM's disposal are listed in Table 7, along with the numerical aperture and the field of view. With the exception of the 10x objective lens, the remaining objective lenses have a numerical aperture greater than 0.5.

Objective lens	Numerical aperture	Field of view
10x	0.3	1.28 mm x 1.28 mm
20x	0.6	640 µm x 640 µm
50x	0.95	256 µm x 256 µm
100x	0.95	128 µm x 128 µm

Table 7: The objective lenses of the CLSM with their numerical apertures and fields of view

Given the field of view of the 100x objective lens, the maximum measurable height for an ideal Rockwell hardness diamond indenter is 21.65 µm. Restricting the cross-sectional diameters of the indenter to be completely within the field of view, the evaluable height is a mere 10.52 µm. This is inadequate to characterize the entire spherical region of the indenter. Therefore, only the 20x and 50x objective lenses can be considered.

In [95], Gao et al. recommend the criterion given in Equation 42 to characterize measurable local slopes using spheres of diameter *D*, where x_{FOV} is the length of the field of the view along the x-axis and A_N is the numerical aperture of the objective lens.

$$\frac{1}{3} x_{FOV} \leq D \cdot A_N \leq x_{FOV} \qquad \textbf{Equation 42}$$

For the indenter's case, the 20x objective lens satisfies this criterion. The 3D representations of the surface of the indenter EDK2 using the height data as acquired by the 20x and 50x objective lenses are shown in Figure 45. With its larger field of view, the

https://doi.org/10.7795/110.20250619

20x objective lens captures a much larger portion of the indenter, extending well into the conical region.

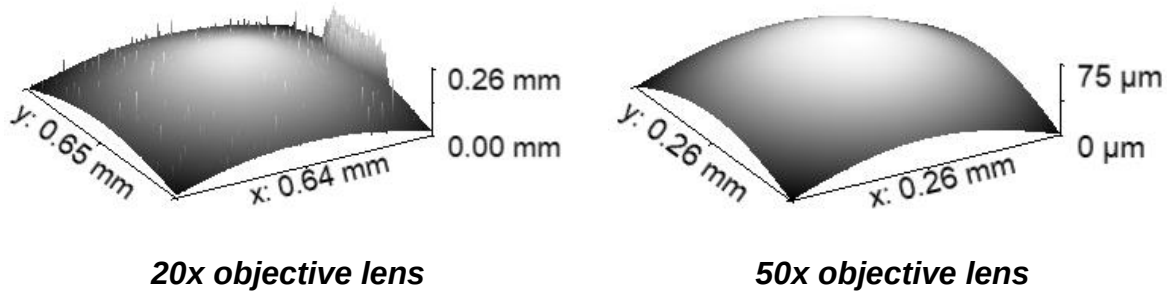

20x objective lens ***50x objective lens***

Figure 45: 3D surface depiction of the indenter EDK2 as captured by the 20x and 50x objective lenses of the CLSM

A smooth surface is obtained using the 50x objective lens, whereas disturbances on the surface are seen in the image captured by the 20x objective lens. This is due to the inevitable presence of form deviations and microscopic roughness on the surface of a real indenter. As the local slopes across the indenter surface exceed the theoretical capability of the maximum measurable slope of a 20x objective lens, which is limited to 36.87°, such measurement artefacts are seen in the image.

Therefore, the use of a 50x objective lens for the purposes of calibrating the tip radius of a Rockwell hardness diamond indenter is justified. Additionally, much better resolution of the spherical region of the indenter can be achieved using the 50x objective lens due to the smaller pixel size in comparison to the 20x objective lens.

Generally, it is assumed that the performance of a microscopic objective is the most accurate when the sample to be measured is centrally located in the field of view. The performance reduces and the capabilities of an objective lens cannot be fully utilized at the borders along the field of view. However, if the centrally located sample is much smaller than the field of view, the accuracy of the captured image is also negatively affected because of the increased pixel size to measurable radius ratio [95]. To accommodate these two opposing characteristics of objective lenses, the field of view could be reduced and the different sections of the captured image of a measurand be digitally stitched. Since stitching is a time-consuming process and introduces additional errors into the measurement, it has not been carried out in this work.

To characterize the effect that an objective lens has on the acquired point cloud of a spherical sample and the overall R-h curve, three spheres (D120, D400 and D2000) from the PTB2 sample are chosen. Since the sphere D400 has the same nominal radius as the spherical region of a Rockwell indenter, the results of this investigation are transferrable to the Rockwell indenter. The spheres D120 and D2000 are chosen to study the effects for the smallest and largest available sphere.

https://doi.org/10.7795/110.20250619

The portion of the spheres within the fields of view of the 20x, 50x, and 100x objective lenses are shown in Figure 46. Only small portions around the apex of the D2000 sphere (in yellow) fit within the field of view of the three lenses, but not the entire sphere (see Appendix 7). The D120 sphere (in purple) fits entirely within the field of view of all the three objective lenses but does not significantly occupy the field of view of the 20x objective lens (see Appendix 8).

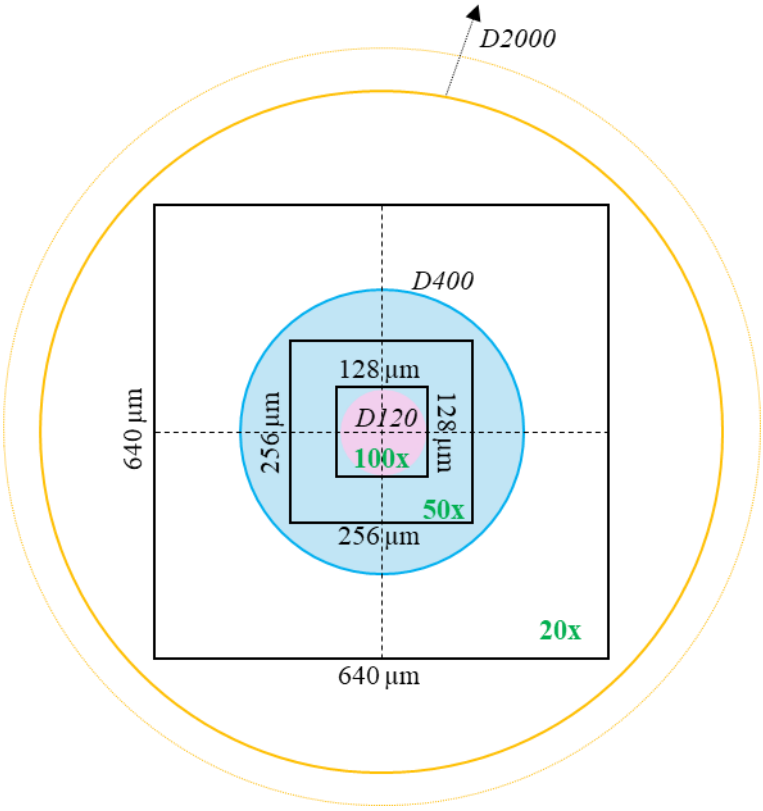

Figure 46: Sketch of ruby spheres (D120, D400, D2000) within the fields of view of the 20x, 50x and 100x objective lenses of the CLSM

The results of the measurements on the D400 sphere are presented using R-h curves in Figure 47. The black dotted line in the figure represents the nominal radius of 200 µm. For every objective lens, the calculated radii vary by about ± 5 µm from the nominal value depending upon the height of evaluation. Amongst the three, the 100x objective lens measures the largest radii. Furthermore, its radii values are consistently larger than the nominal value. Despite the height of the evaluation not being restricted to equal cross-sectional diameters in the field of view, no discontinuity is seen in the R-h curve.

Further, the 50x objective lens always measures a smaller radius than the nominal value, with the exception being at the start of the curve. At lower heights, the 20x objective lens measures the radii smaller than the nominal value but converges to it with increasing height. The R-h curves for the 50x and 100x objective lenses run parallel to

https://doi.org/10.7795/110.20250619

each other and are similar in shape. This could be due to the same numerical aperture of the two objective lenses. However, the pixel density of the 100x objective lens is higher than that of the 50x objective lens. A lower pixel density results in the smoothening of surface artifacts, which could explain the offset between the two R-h curves. A further plausible explanation for the offset could be the differences in the optical paths of the objective lenses.

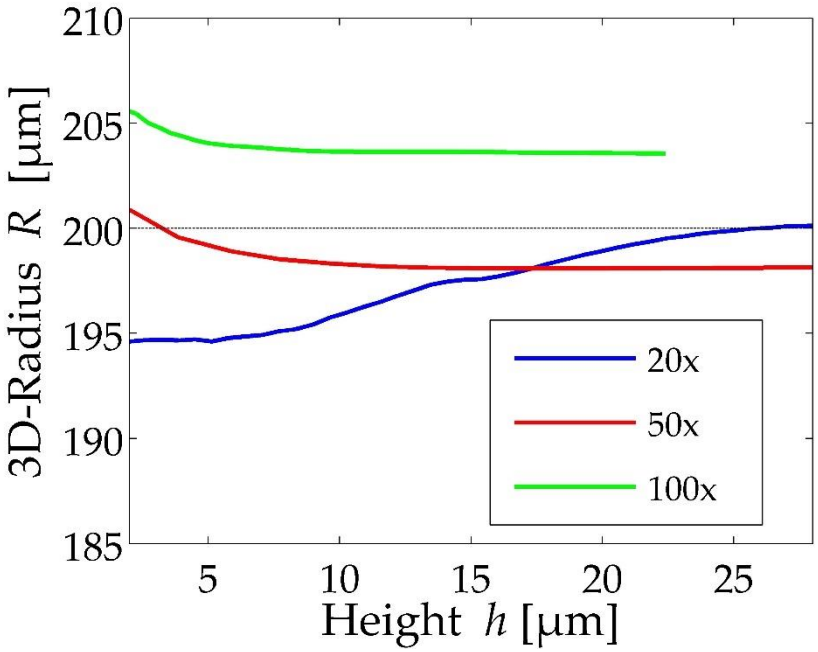

Figure 47: R-h curves for different objective lenses of the CLSM obtained through measurements on the D400 sphere

It must be pointed out that the 3D surface of the D400 sphere captured by the 20x objective lens did not contain disturbances and measurement artefacts, such as those seen in the image of a Rockwell indenter in Figure 45. This reinforces the understanding that the presence of form errors and roughness influence the measurement capability of an objective lens. Nevertheless, since the D400 sphere doesn't fully occupy the field of view of the 20x objective lens, noise around the sphere is seen in its captured image. Additional post-processing is thus required, which reduces the evaluable height for the calculation of the radius.

The R-h curves for the sphere D120 are shown in Figure 48. Both 50x and 100x objective lenses measure the radii larger than the nominal value of 60 µm. Given the size of the D120 sphere, cropping of the captured image from the 50x and 100x objective lenses is required, whereas an image filled with noise is obtained with the 20x objective lens. Therefore, the R-h curve for the 20x objective lens is not available. At a height of 35 µm from the apex, a radius of 63.4 µm and 64.6 µm are obtained for 50x and 100x objective lenses, respectively.

https://doi.org/10.7795/110.20250619

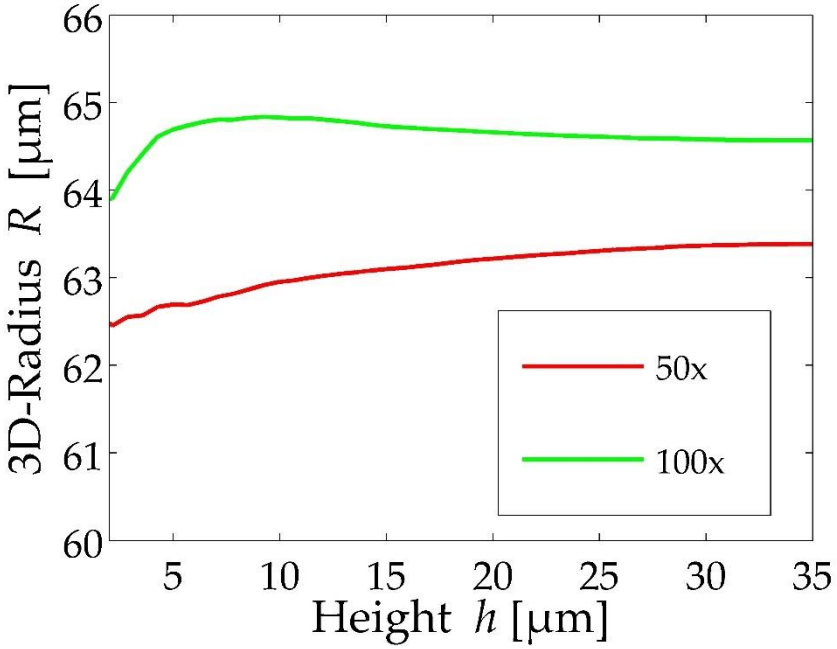

Figure 48: R-h curves for 50x and 100x objective lenses of the CLSM obtained through measurements on the D120 sphere

The R-h curves for the D2000 sphere are shown in Figure 49. Like the other two spheres, the radius of the D2000 sphere measured by the 100x objective lens is larger than the nominal value and also larger than that obtained with the 50x objective lens. Zooming into the R-h curve of the 100x objective lens, a stable radius between the heights of 2 µm and the maximum evaluable height of 4 µm is seen. The shape of the R-h curves for the 50x and 20x objective lenses resembles the R-h curves of the D400 sphere for their respective lenses. The minor disturbances present in the captured image with the 20x objective lens are treated with a median filter. No tangible difference is seen in the shape of the R-h curve after its application.

Along with the slope measuring capability of a 50x objective lens and given the overall shape of the R-h curve, its use is more feasible for the calibration of the tip radius of a Rockwell indenter over a range of heights using a correction factor. When a single radius value at the transition point (h = 26.8 µm) needs to be calibrated, the 20x objective lens could be considered.

In summary, the differences in the measured radii for the objective lenses are most likely due to their individual aberrations, which vary based on the distribution of light at the point of focus, the lateral position of the sphere inside the field of view, and the partial surface slopes and their orientations.

https://doi.org/10.7795/110.20250619

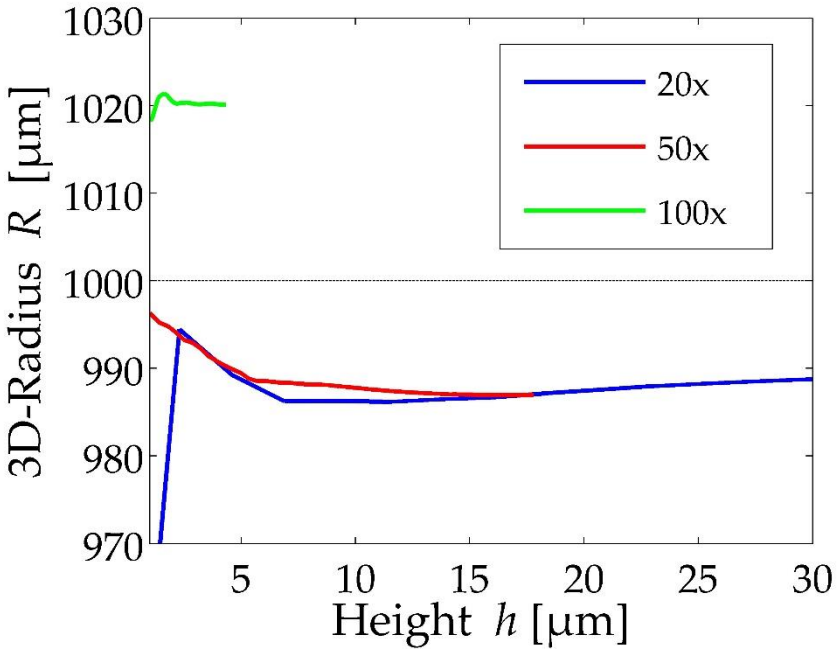

Figure 49: R-h curves for different objective lenses of the CLSM obtained through measurements on the D2000 sphere

6.6.3. Reproducibility and repeatability

Multiple repetitions of a CLSM measurement one after the other for a given sample and at the same position on the sample using a 50x objective lens do not show any significant variation in the calculated radii results. Typically, a measurement begins after positioning the indenter under the CLSM. During the course of this study, each measurement is repeated on an average about eight times. This is followed by rotating the sample holder by 90° in the x-y plane and performing eight more measurements. Table 8 presents the mean and standard deviation of the calculated radii for the eight measurements on the indenters EDK1, EDK2, and EDK3 and evaluated at a height of 26.8 µm from the tip apex of the indenters.

Indenters	Mean [µm]	Standard deviation [µm]
EDK1	192.19	0.11
EDK2	190.80	0.11
EDK3	195.20	0.05

Table 8: Statistics of 3D evaluation of three indenters measured by CLSM with 50x objective

https://doi.org/10.7795/110.20250619

The low standard deviation indicates that the results are precise. A randomly chosen magnified section of the R-h curve for the indenter EDK2 is shown in Figure 50 for the eight repeated measurements. The order of the measurement has been indicated on the right side of the figure. A clear rise in the radii can be seen in the first six measurements. The results appear to stabilize and converge after the sixth measurement. This could mean that a thermal equilibrium had not been reached in the CLSM instrument before the start of the series of measurements. The maximum increase of 0.3 µm in the calculated radius between any two repeated measurements cannot be assigned to the volumetric expansion of the diamond indenter. Given the linear thermal expansion of diamond at room temperature is 0.7 x 10^{-6} K^{-1} [96], an increase in temperature of about 2000 °C is required to attain a 0.3 µm increase in the radius. Therefore, the increase in radius seen in the R-h curve can be claimed to be thermal drift of the measurement instrument.

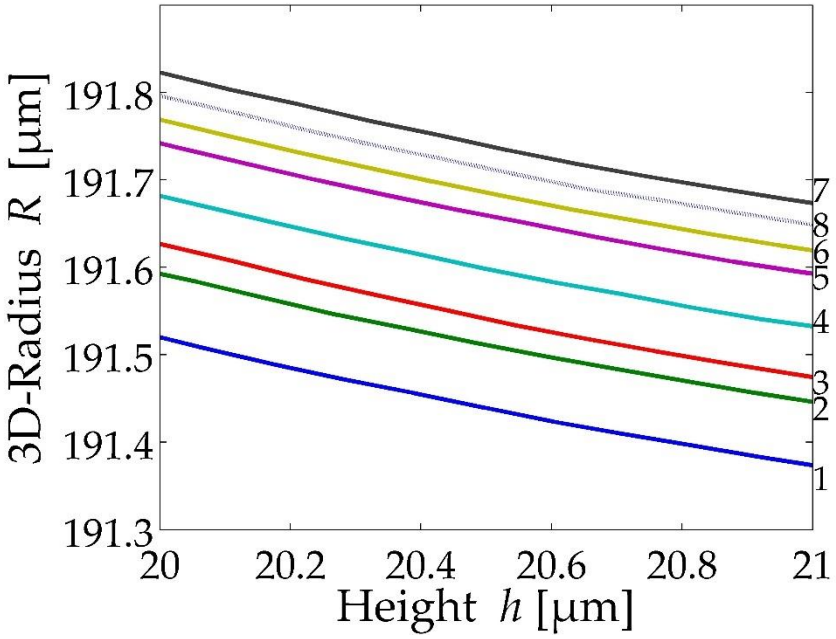

Figure 50: A zoomed-in section of the R-h curve for eight measurements on the indenter EDK2 measured by CLSM with 50x objective

The extent and impact of the thermally induced drift on the measurement have also been investigated. This is performed using a D400 sphere. The CLSM instrument is turned off for more than five hours prior to the beginning of this investigation to ensure that the heat from the system has entirely dissipated. The series of measurements are performed overnight and take a total of 13 hours, with each measurement taking roughly 12 minutes. A 50x objective lens is used, and a height of approximately 100 µm from the apex is measured. The stage drift in *x* and *y* is determined using target tracking. Marks on the surface of the sphere as seen on the intensity image are used as fiduciary markers.

https://doi.org/10.7795/110.20250619

The stage drift in the *x* and *y* directions with respect to the measurement number is shown in Figure 51. Between the first and second measurements, a stage drift of about 800 nm is recorded in both the *x* and *y* directions. Subsequently, the amount of drift between the measurements consistently reduces. From the seventh measurement onwards, the drift between measurements is less than 250 nm. Considering the entire measurement series, the largest drift recorded in the *x* and *y* directions is 4.2 µm and 3.5 µm, respectively. The drift rate in the *x* direction stabilizes much later in comparison to the stage drift in the *y* direction, which is relatively constant from the tenth measurement onward.

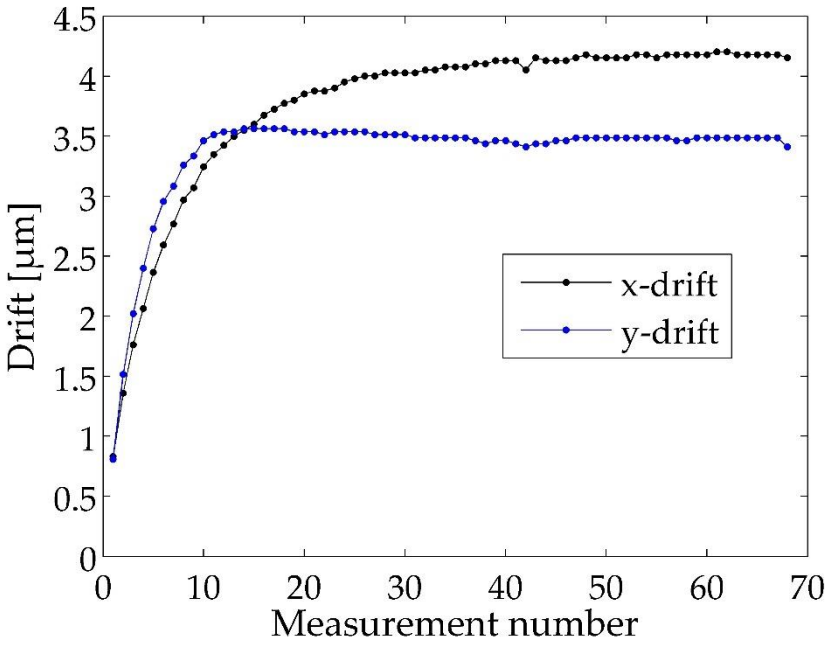

Figure 51: Stage drift in the CLSM instrument along the x and y directions

Analyzing the R-h curves obtained from these 69 measurements, it is noticed that the radius grows with the increase in the number of measurements. A trend similar to that seen in Figure 50 is noticed. Post the fortieth measurement, the maximum difference in the calculated radius between any two measurements is below 0.1 µm.

Although these results are important for form measurements, they do not play a decisive role in the calibration of the radius of the Rockwell hardness diamond indenter. This is because it is ensured that the instrument has reached a thermal equilibrium before performing important measurements. Additionally, a translational shift in the position of the indenter during the measurement in the order of a few micrometers does not affect the 3D evaluation since the algorithm searches for the highest point on the indenter and evaluates the radii accordingly.

To investigate the reproducibility of the CLSM instrument, some measurements on the Rockwell hardness diamond indenters have been performed after a period of about 2.5 years. A deviation of 0.5 µm in radius from heights of 7 µm from the apex onwards

https://doi.org/10.7795/110.20250619

is observed in the R-h curves of the previously measured and newly measured data, although the measurement conditions, sample preparation and evaluation procedure have been kept unchanged. In the meantime, the indenter had been used for calibrating hardness reference blocks. Nevertheless, a deviation of 0.5 µm cannot be due to the deformation of the diamond, given its robustness. Physical damage such as breakage, cracks, etc. would be visible in the intensity image and in the shapes of the R-h curves. The CLSM had been repaired due to a collision with a measurand. This could explain the deviation in the results and signify the importance of recalibration. Post recalibration, no significant differences in the R-h curves were observed.

In conclusion, the results obtained from the CLSM have been proven to be precise. However, the comparison of these obtained results with a traceable tactile instrument indicates a systematic deviation and challenges the accuracy of the results.

6.6.4. Sample cleaning

Cleaning indenters in and of itself is a challenging task, and no one size fits all formula exists in the literature. In this study, the cleaning is undertaken as follows. Firstly, compressed carbon dioxide is blown over the surface to knock off large dirt particles along with other solid contaminants. This is followed by cleaning the indenter with a combination of ethyl alcohol and isopropanol solutions using a microfiber cloth. Finally, the indenter is pressed multiple times by hand into an acrylic sheet. After inspecting the indenter using the intensity image of the CLSM, it can be concluded if the surface is sufficiently clean or not. Typical reasons that require the repetition of the cleaning cycle include the presence of dust corns, cloth fibers, and smudge marks from the evaporation of alcohol. Figure 52 shows the intensity images of an indenter before and after cleaning. The dirt tracks on the uncleaned indenter originate from the pushing of dirt by the stylus tip during the tactile measurement. Inspecting the R-h curves for both these measurements reveals that the cleaning of the indenter does not play a crucial role in the calibration of the radius of the indenter. Nevertheless, it still belongs to good practice to undertake it, as the surface otherwise does not accurately represent the true surface of the indenter.

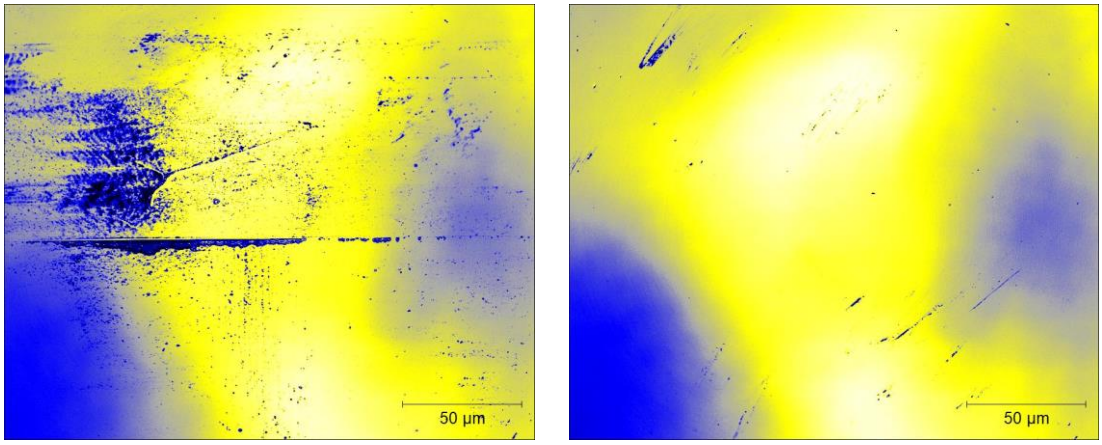

Figure 52: Intensity images of an uncleaned and cleaned indenter

https://doi.org/10.7795/110.20250619

6.6.5. Sample orientation and tilt

Rotating the indenter by 90° in the x-y plane and comparing the resulting R-h curves, it can be observed that the results are consistent. Thus, the orientation of the indenter during its radius calibration is irrelevant. This result also implies that the lateral calibration in *x* and *y* of the CLSM is apt.

Furthermore, the influence of sample tilt is investigated by tilting the indenter by 1° increments up to 4°. The resulting R-h curves are shown in Figure 53. Up to a height of 12 µm from the indenter apex, the fitted radii differ significantly from one another. This is due to the shifting of the tip of the indenter. Thereafter, the curves converge and begin to diverge again at heights greater than 20 µm. Taking a closer look at the radii near the blend point, for every degree of tilt, the radius increases by 0.1 µm, 0.5 µm, 1 µm, and 2 µm, respectively. The apparent flattening of the indenter tip, as indicated by the increase in the radius at the beginning of the R-h curve, is due to the displacement of the highest point on the indenter and the eventual unsymmetric distribution of the transition region of the indenter in the acquired CLSM image.

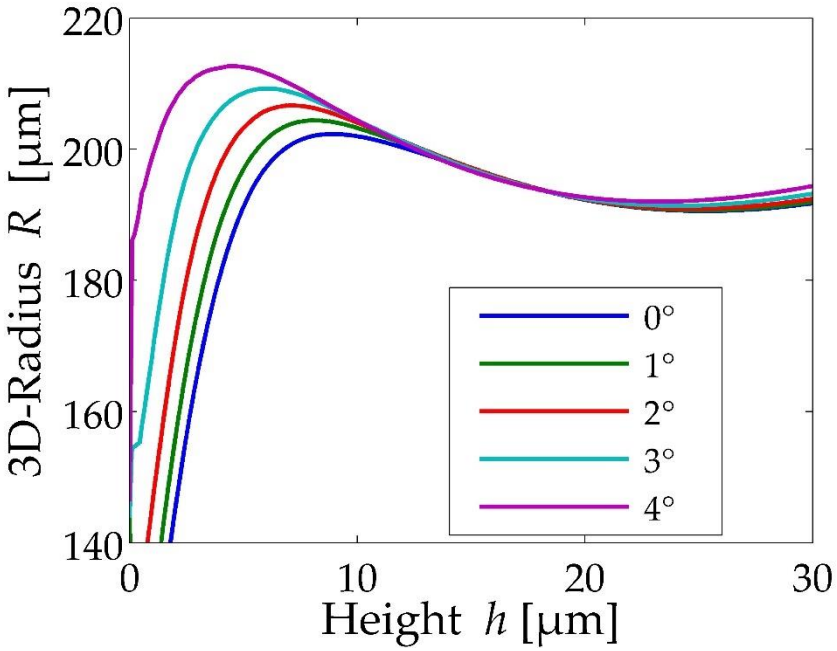

Figure 53: Effect of sample tilt on the R-h curve of an indenter

For this analysis, it has been assumed that the indenter axis is perfectly aligned with respect to the axis of the indenter holder. During the manufacturing of the diamond indenter, perfect alignment of the indenter in its holder is difficult to achieve. Hence, the standard [38] restricts the inclination of the axis normal to the mounting surface to be within 0.3°. From the above analysis, it can be said that this is a good threshold, as 1° tilt amounts to an increase in only 0.1 µm in radius value. Nevertheless, the stress fields in the material and the overall indentation process could differ due to a tilt of 1°. This requires further investigations.

https://doi.org/10.7795/110.20250619

6.6.6. Type of material and surface roughness

During this study, materials such as diamond, ruby, and sapphire have been measured using the CLSM. The radii of all the materials could be measured without any difficulties. To ensure that the true 3D surface of the measurand is captured and not optical reflection artefacts, the diamond indenter is coated with 80 nm of pure gold using a sputtering device. This is performed since diamond is a transparent material known to exhibit total internal reflection. A coating of 80 nm is chosen as this is sufficient to completely opacify the indenter and not alter its geometric shape significantly [97]. Figure 54 (a) shows the intensity image of the gold coated indenter EDK2. A large particle of dust can also be seen in this image. Figure 54 (b) presents the R-h curves of the coated and uncoated indenter, along with the R-h curve of the gold coated indenter with the dust particle on it.

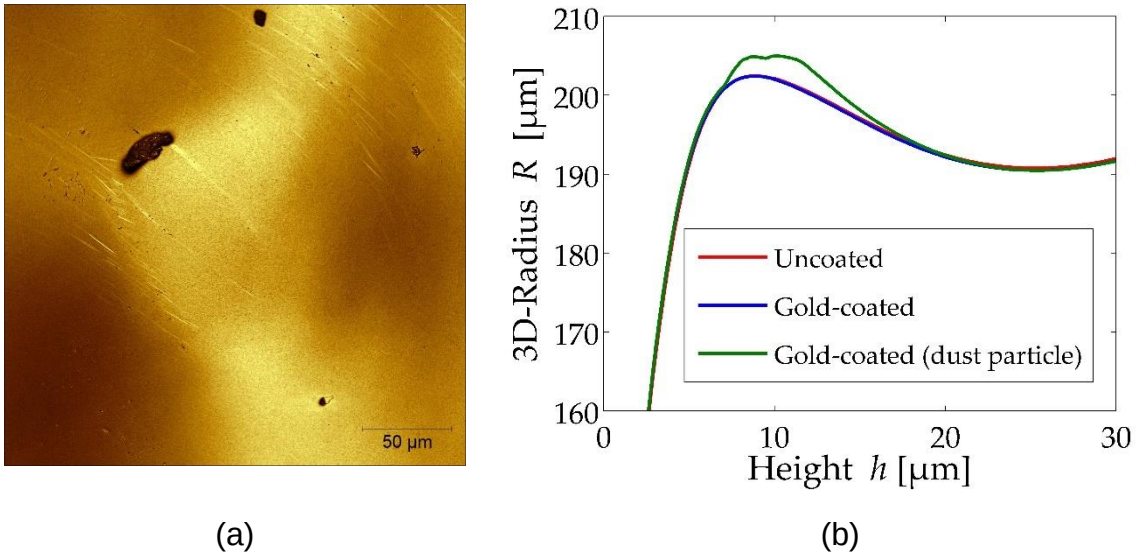

(a) (b)

Figure 54: (a) Contamination on the indenter; (b) Effect of sample coating on the radius vs. height plot

The R-h curves of the coated and uncoated indenter overlap almost perfectly. The curve representing the dust particle deviates from the other two at heights between 8 µm and 18 µm, which is exactly where the dust particle sits. Further along the height axis, the radii converge again due to the vast number of data points. This further illustrates the advantage of a 3D point cloud evaluation of an indenter in comparison to a 2D profile evaluation. Assuming a 2D profile is extracted over the dust particle and a conventional 2D evaluation is performed, a good indenter would fail to meet the criteria of the standard relating to permissible form error.

It is interesting to note that the fitted radius for the coated indenter is greater than the uncoated indenter only at smaller heights. This could be due to the uneven sputtering of gold on the surface of the indenter. A deviation of around 0.2 µm is recorded near

https://doi.org/10.7795/110.20250619

the heights at which the indenter is generally calibrated. Thus, it can be concluded that a diamond indenter need not be coated and can be measured using a CLSM without worrying about its transparency.

The presence of surface roughness on an indenter adversely affects hardness measurements. This fact is corroborated by the standard [37], yet no form of quality control measure is proposed therein. The standard for IIT [25] suggests that the average roughness (R_a) value be under 1/20th of the indentation depth, also known as the 5 % rule. Adopting this into Rockwell hardness testing, where the indenter is polished for indentation depths up to 300 µm, results in a tolerable R_a value of 15 µm. A study conducted within the PTB on a generic Rockwell diamond indenter measured a mean R_a value of 10 nm with a standard deviation of 1.1 nm and an *RMS* value of 12 nm. This measurement is based on 40 linear profiles extracted from the conical region of the indenter.

Since surface roughness affects the evaluation procedure in a similar fashion to instrument noise, it can be said that its effect is minimal on the fitting procedure. However, care must be taken that the combined influence of the surface roughness and the instrument noise does not hamper the evaluation process.

6.6.7. Sample size and shape

In the previous sections, it was alluded to the fact that the discrepancy between the tactile and optical measurement must be stemming from the shape of the measurand. In this subsection, a more detailed examination of the various sample shapes is conducted. Measurement samples such as depth-setting standards are measured and calibrated on a regular basis using the CLSM. Furthermore, dimensional measurements of nano-pillars etched on silicon wafers have also been measured [98]. In addition, capacitive displacement sensors with etched gold and aluminum have been characterized using the CLSM and validated using a metrological AFM [99]. These are a few among various other calibration procedures that are undertaken using the CLSM. A common factor among these samples is that they are 2-D coordinate measurements coupled with height information. More importantly, they are flat areal surfaces. None of these samples have posed a problem to the CLSM.

Pyramid-shaped hardness testing indenters such as Vickers and Berkovich indenters are excellent choices for flat surfaces with a slope. As a test for the capability of the CLSM for measuring slopes, a Berkovich indenter is examined. The primary use of this indenter is in the determination of nanohardness in GPa units. Hence, the projected contact area is the primary quantity of interest. Prior to the evaluation of the instrument indentation testing data, indenter tip area calibration is performed. This accounts for the non-ideal shape of the indenter. Figure 55 presents the tip area function of an indenter VB124 measured using three different measurement methods. The state-of-the art or the reference measurement in this case is the AFM. This is followed by the indirect determination of the tip area function using multiple indents on a fused quartz

https://doi.org/10.7795/110.20250619

sample with known mechanical properties. For reference, the ideal tip area function is also plotted. Regardless, the true tip area function will always be greater than the ideal function due to tip rounding.

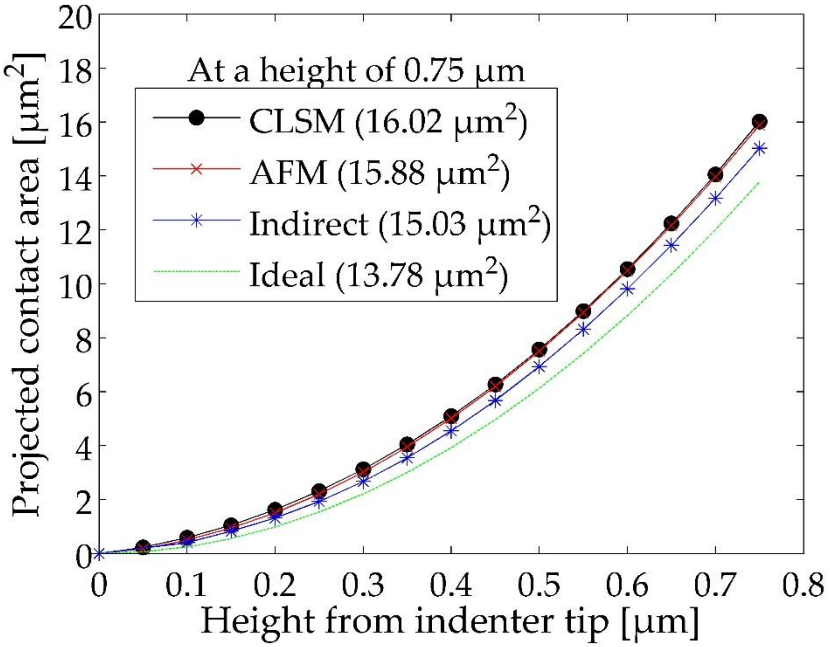

Figure 55: Tip area calibration of a Berkovich indenter (VB124) using direct measurement method (AFM and CLSM) and indirect measurement method

An excellent agreement between the results of the AFM reference measurement and the CLSM is seen. The difference in the projected contact area at a height of 0.75 µm is a mere 0.14 µm² (< 1 %). Since the elastic radial displacements have not been considered, the indirect calibration differs from the direct reference calibration method. The absolute percentage deviation of the indirect calibration at the same height with respect to the reference value is approximately 5 %.

Applying a spherical fit to the 28 data points of the CLSM from the tip apex of the indenter until a height of 10 nm, a radius of 440 nm is obtained. Likewise, for 61 data points from the tip apex until a height of 21 nm, a radius of 498 nm is obtained. With increasing height, the radii increase linearly. The determination of the height of transition from the rounded tip onto the pyramid is not trivial. To estimate a consolidated value for the tip radius, the Bei-Pharr method can be used [100]. The Bei-Pharr method expresses the tip area function of the indenter using a quadratic and a linear term with respect to height. From the constants of the equation, the tip radius and an equivalent cone angle can be calculated. The radius calculated using the Bei-Pharr method is 484 nm, which is comparable to the two fitted radii obtained from the spherical fit.

The corresponding radius value for the reference measurement using the Bei-Pharr method is 412 nm. The radius calculated using CLSM is 17.5 % larger than that calculated using the reference measurement. Per contra, the projected contact area at

https://doi.org/10.7795/110.20250619

0.75 µm is just 0.9 % larger for the CLSM in comparison to the reference value. This disparity can be justified on the basis of the negligible size of the tip rounding in comparison to the overall area of the indenter at a height of 0.75 µm. Thus, it can be said that flat surfaces and slanted surfaces could be measured with sufficient accuracy and precision using the CLSM. Nonetheless, further research using additional measurement objects is still required to confirm these findings.

However, on spherical surfaces such as the indenter tip of the Rockwell hardness diamond indenter, the slope changes continuously over the surface, starting from 0° at the tip apex until 30° at the transition point (for an ideal indenter). Therefore, the spheres from the sample PTB2 are measured using the CLSM and compared with the reference values obtained from PTB's nano-measuring machine (NMM) using a stylus sensor with a 2 µm spherical radius with an opening angle of 90°.

The reference measurement results obtained from the NMM contain the dilated point cloud data. Since the type of scan for the NMM and CLSM is different (radial scan and grid scan respectively), a deviation plot has not been presented. However, the deviation between the fitted radii as a function of height from the tip apex of the sphere can be compared. It must be noted that the heights at which the radii can be measured and compared depend upon the measurement capability of the instrument and the restrictions due to the sample size and shape. This includes factors such as noisy edges in the CLSM image due to steep slopes, field of view of 50x objective lens, mechanical difficulties, etc. Therefore, the presented results only show the radii at heights where both the instruments can measure completely and reliably.

The point clouds obtained from both the instruments are fitted with a sphere, and the percentage deviation of the CLSM radius from the reference radii value is shown in Figure 56. Prior to interpreting the results in the figure, it must be mentioned that for all the spheres the CLSM results are close to but not the exact nominal values specified by the manufacturer with no exceptions. On the contrary, the NMM results match the nominal values almost exactly except for the spheres D400 and D120. This is rather unfortunate, since D400 is the sphere that resembles the ideal shape of the Rockwell indenter tip. The radius of D400 as determined by the NMM is 192.8 µm, which is around 7.2 µm smaller than the nominal value. After thorough investigation of the raw data and the fitting algorithm, the deviation between the NMM and the nominal value is attributed to the surface quality of the measured sphere. Since the measured surface exhibits form deviations coupled with a few defects, the evaluated results are impacted profoundly in the case of the NMM measurement. Hence, the results of D400 and D120 are not presented in Figure 56. The quality of the spheres has been inspected using intensity images obtained from the CLSM, and it can be confirmed that the quality of D400 and D120 do in fact differ significantly from the other spheres in the PTB2 sample.

https://doi.org/10.7795/110.20250619

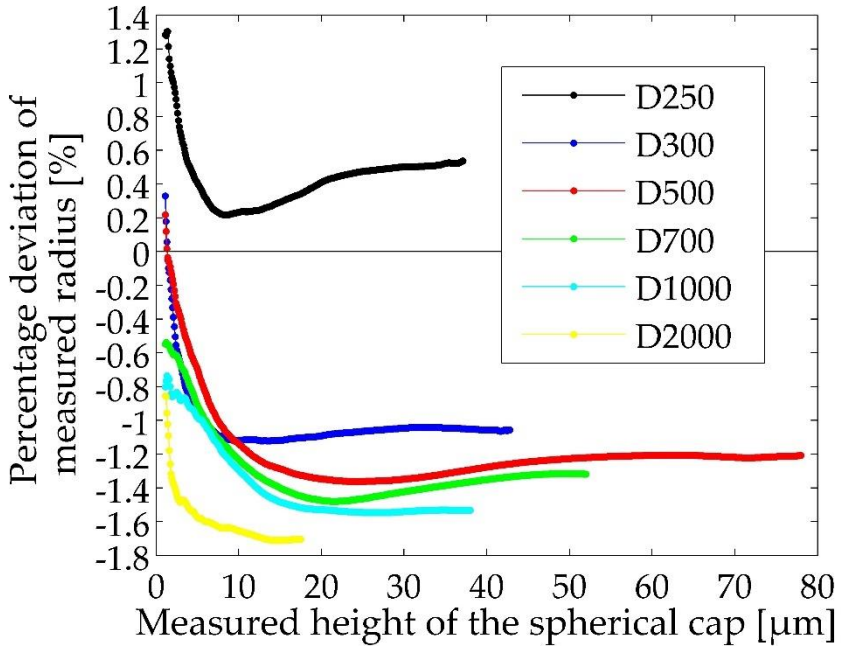

Figure 56: Percentage deviation of the fitted radii for the spheres in the sample PTB2 with respect to the height of the sphere

The results of the comparison for the remainder of the spheres are counterintuitive. Typically, the least amount of error is expected for the largest sphere D2000 because less than 2 % of the surface area of its hemisphere is captured within the field of view of the objective lens. Hence, the surface slopes in this segment of the sphere are gentle and well below 10°. However, the largest amount of percentage deviation from the tactile measurements of -1.7 % is observed for the D2000 sphere. One possible explanation for this could be the spherical fit on the measured point cloud data. Since a smaller portion of the sphere is available for the fit, the uncertainty associated with the fitted radius is larger. Nevertheless, the same fitting procedure is used for both the reference measurement and the CLSM measurement. Given the reference measurement captures the sphere's topography at much greater heights, the fitted radii must be significantly different at greater heights if the largest amount of percentage deviation in the D2000 sphere is to be attributed to the fitting procedure. This is however not the case. The fitted radii of the reference measurements at greater heights are comparable to those at lower heights, and the center of the fitted sphere is also consistent over the height. Therefore, the spherical fit is most likely not the cause for the largest amount of percentage deviation in the D2000 sphere.

Furthermore, with the decreasing size of the sphere, the absolute deviation decreases gradually. The shape of the deviation curves is similar for all the spheres. When the height increases, a steep increase in the absolute percentage deviation is observed, which is followed by a fairly constant absolute deviation. For some spheres, a further change in the shape of the deviation curve is observed between the height at which the cross-sectional diameters of the sphere are the same and the theoretical maximum

https://doi.org/10.7795/110.20250619

measurable height. This could be due to both the position of the sphere in the field of view and the larger surface slopes in this region of the sphere.

Principally, the radius of every sphere is measured smaller than the reference with the CLSM except for the sphere D250. Although the shape of the curve for this sphere is like the others, it lies separated from the rest of the curves. Assuming the nominal value of the sphere D120 to be accurate, a positive deviation larger than five percent is calculated for the difference between the CLSM and the nominal value. The complete reversal of the deviation trend for spheres with radii smaller than 125 µm is peculiar, especially because at lower heights the differences in the surface slope for the spheres D300 and D250 are not so drastic. Perhaps spheres that do not fully occupy the field of view of the 50x objective lens trigger the reversal of the deviation trend.

A summary of the results evaluated at a height of 30 µm (except for D2000) from the pole of the spheres has been presented in Table 9 along with the nominal radii R_n, the reference value of the radii R_r, and the measured radii using the CLSM R_{CLSM}. The theoretical height at which the cross-sectional diameters of the spheres have the same length is given by h_s, whereas the theoretical surface slope at the height h_s is listed under θ.

Sample name	R_n [µm]	R_r [µm]	R_{CLSM} [µm]	h_s [µm]	θ_{max}
D2000	1000	1000.5	983.7	8.2	7.5°
D1000	500	500.1	492.6	16.7	15°
D700	350	350.1	345.0	24.2	22°
D500	250	250.0	246.5	35.3	31°
D400	200	-	197.2	46.3	40°
D300	150	150.5	148.9	71.8	60°
D250	125	124.0	124.6	125	90°
D120	60	-	63.4	60	90°

Table 9: Measurement values of spheres of varying radii evaluated at height of 30 µm

The percentage deviation of the measured radii using CLSM from the reference radii values for spheres with radii greater than 125 µm is plotted in Figure 57. Along with these results, the results of measurement of spheres from the literature [90] are shown in the figure. In [90], the authors state that the percentage deviation is a constant offset

https://doi.org/10.7795/110.20250619

of +1.2 %. However, it can be seen that the absolute percentage deviations increase with the increase in the size of the sphere for both sets of measurements. Despite this observation being counterintuitive, the fact that two independent sets of measurements using different measuring instruments come to the same conclusion is an indication of its correctness.

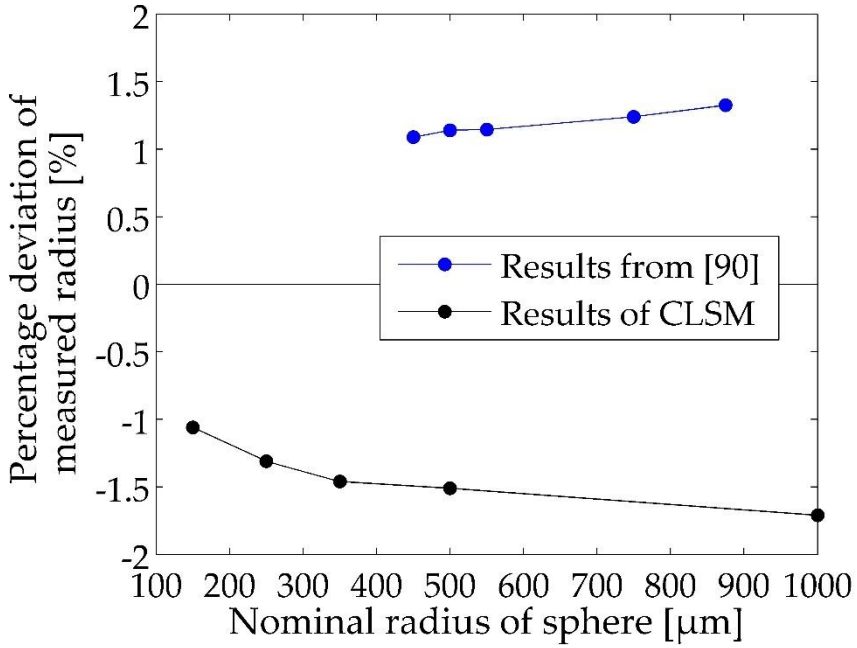

Figure 57: Plot of percentage deviation in measured radii for spheres of varying radii with respect to its size

6.7. Correction of the indenter radius measured using CLSM

It is evident that a number of factors contribute to the overall discrepancy in the measured radii obtained from the CLSM, such as the surface slope of the measurand, the rate of change of surface slope, the precision of the tip dilation process in tactile measurements, the surface roughness of the measurand, the position of the measurand in the field of view, and numerous additional factors. A simple recalibration of the *z*-axis would be ineffective and also impede the measurement of objects with different shapes. If spheres whose nominal radii are known a priori are to be measured with the CLSM, the obtained values can be corrected using the results shown in Figure 57. However, in the case of an unknown object with a combination of different geometric features, this is not a viable option. One illustrative example is that of an object with a rough surface, which may be conceptualized as a combination of discrete convex and concave spherical caps of varying sizes.

Given the large magnitude of the deviation in the measured radii between the CLSM and the reference tactile measurement for a Rockwell diamond indenter, it is incumbent upon the calibration agency to correct it, prior to undertaking official calibration work with the CLSM. Multiple strategies to correct this error could be considered. The

https://doi.org/10.7795/110.20250619

simplest of which is to measure a large number of Rockwell diamond indenters with the CLSM, followed by performing traceable reference measurements on it. The quality of the obtained topography from the CLSM in comparison to the topography obtained from the reference measurement, and in general, the performance of the CLSM in measuring the form of an indenter is ignored. The focus is placed solely on the end result, which is the fitted radius at a height of 26.8 µm from the tip apex of the indenter obtained from both the measurement instruments. The data points of the measured and the reference values can be plotted on a scatter plot as shown in Figure 58, which considers the measurement of six indenters (EDK1, EDK2, EDK3, EDK6, EDK7, and EDK8). Fitting a line through the data helps establish a relationship between the measured value and the traceable reference values, which can be used to correct the systematic errors.

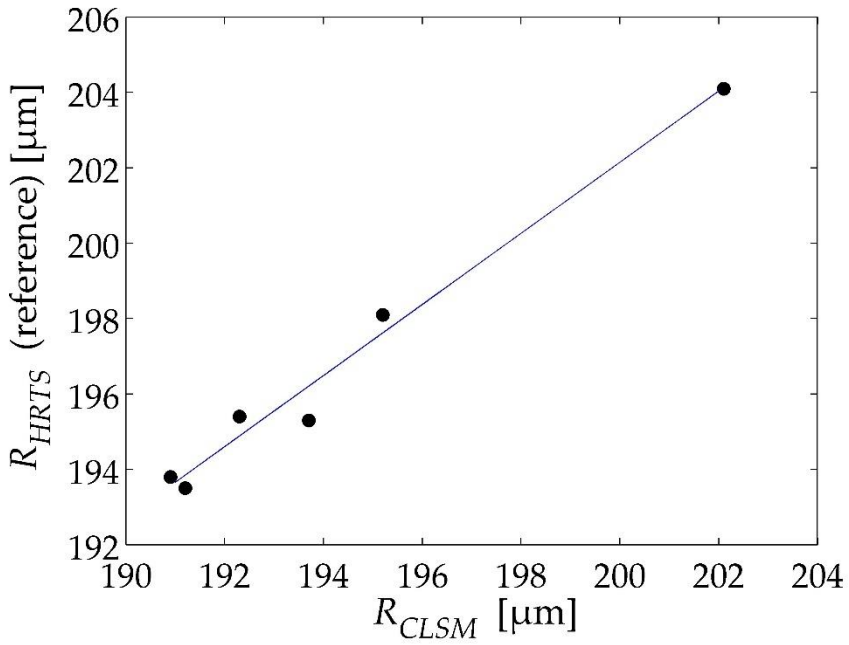

Figure 58: Linear regression correction method for indenter tip radii measured using the CLSM

Irrespective of the trustworthiness of the reference values, a major drawback of this method is its dependence on the geometry of the indenter. In case a set of indenters with skewed geometric properties are used to determine the calibration factor, a fixed bias persists in every future calibration. The application of this method resulted in the reduction of the absolute average percentage deviation of the measured radii from the reference value from 1.3 % to 0.2 %.

To eliminate the effect of the variation in the indenter shape from its ideal shape and also to rule out the effect of skewness of the geometric properties of the indenter on the linear calibration factor, the D400 sphere is measured using a traceable tactile coordinate measuring machine (CMM). Following a successful calibration, the D400 sphere can be used as a transfer standard.

https://doi.org/10.7795/110.20250619

The calibrated diameter for the D400 sphere is 399.91 µm ± 0.50 µm. This is obtained by performing three measurements on the surface of the sphere from the pole to the equator, with each measurement comprising of 32 data points. The topography of the upper hemisphere of the D400 sphere is acquired with a sphere of diameter 125 µm and a probing force of 1 mN.

The transfer standard is then measured using the CLSM with a 50x objective lens. Evaluating the CLSM measurement data at a height of 27 µm from the apex of the sphere gives a radius of 197.13 µm. Considering the data points from the CMM only till a height of 27 µm yields a corresponding reference radius of 199.38 µm. Therefore, the correction factor that must be incorporated for the CLSM when measuring a sphere with a radius of 200 µm is 1.13 %. Applying this correction factor to the 6 aforementioned Rockwell diamond indenters, the absolute average percentage deviation of the measured radii using CLSM from the reference value of HRTS reduces to 0.3 %. The slight increase in the percentage deviation in comparison to the linear calibration method is most likely due to differences in the reference measurements. Although it is assumed in this work that the tactile reference measurements are equivalent, there will certainly be minor discrepancies between them.

The advantage of using a transfer standard is the establishment of a robust traceability chain for the calibration of the Rockwell indenter tip radius. Implementation of this method is straightforward, and it can easily be performed even by a novice user. Furthermore, the correction factor assigned to the D400 sphere closely aligns with the mean of the correction factors for the spheres D300 and D500 as obtained from NMM, which is 1.19 %. This provides a degree of validation for the correction method. The drawback of this approach is that it assumes that the indenter exhibits an ideal geometry, similar to the calibrated sphere. Nonetheless, it is safe to assume that the variation of the radius of a Rockwell diamond indenter with respect to the height would be well within ± 50 µm of the nominal value.

Methods such as fitting the data set of errors associated with the surface slope and position within the field of view with a neural network also show good results [90]. Notwithstanding the benefits, this method may not be the most suitable from a metrological perspective. Self-calibration techniques such as the random ball test have also been applied to calibrate slope-dependent errors in optical measurements [101]. Since the spherical region is only a small portion of the indenter tip, the application of this method is not feasible, especially due to the physical constraints in rotating an indenter in every axis. However, the transfer standard (sphere D400) could be calibrated with such a method.

6.8. Estimation of measurement uncertainty

Before proceeding with the estimation of the measurement uncertainty, it is important to clearly define the measurand, measuring instrument, and the measurement conditions. The object being measured is a Rockwell hardness diamond indenter and the

https://doi.org/10.7795/110.20250619

region of interest is the spherical tip of the indenter. The 3D radius evaluated at a height of 27 µm from the tip apex is the measurand. The measurement is performed using the CLSM with a 50x objective lens, which has a numerical aperture of 0.95. The zoom factor is set at 1x.

The largest standard deviation of the measured 3D radius as stated in Table 8 is 0.11 µm. The uncertainty associated with the variation in the measured value is given by the Equation 43, where *s* is the standard deviation and *n* is the number of measurements.

$$u = s/\sqrt{n} \qquad \textbf{Equation 43}$$

Assuming a twofold uncertainty which follows a *t*-distribution, an uncertainty value of 0.08 µm is obtained.

The second source of uncertainty is the resolution of the instrument. This source follows a rectangular probability distribution. The manufacturer of the instrument states that the resolution in any given axis is 10 nm. Due to the surface of the indenter being extracted in three dimensions, a threefold uncertainty is assumed. Therefore, the estimated uncertainty value is 0.02 µm.

The third source of uncertainty is from the transfer standard used to calibrate the measuring instrument. As described in the previous subsection, the transfer standard is a sphere with an uncertainty of 0.5 µm in its diameter. The same value of uncertainty is assumed for the radius and for its evaluation at a height of 27 µm from the apex. Assigning a normal distribution to this source of uncertainty, a standard uncertainty value of 0.25 µm is obtained.

Due to the deviation of the measured radius between the CLSM and the reference tactile measurement, a correction factor must be applied to obtain the best estimate of the measurand. For a sphere of radius 200 µm, the correction factor is 1.13 %. The uncertainty associated with this is assumed to be 0.5 µm, which follows a rectangular probability distribution.

The final source of uncertainty that is considered in this study is the uncertainty associated with the tilting of the measured object during a measurement. Assuming a maximum tilt of 1°, the increase in radius has been shown to be 0.1 µm. Since no further information is known, a rectangular distribution is assigned to this source.

The sensitivity coefficients are assumed to be 1 for all the considered sources. To determine the effective degrees of freedom, the Welch-Satterthwaite equation [102] can be used as follows:

https://doi.org/10.7795/110.20250619

$$\nu_{effective} = \frac{u_c^4(y)}{\sum \frac{u_i^4(y)}{\nu_i}} = \frac{0.40^4}{\frac{0.08^4}{7} + 0 + 0 + 0 + \frac{0.06^4}{7}} = 3323$$

An appropriate coverage factor for a t-distribution with effective degrees of freedom larger than 100 and a confidence interval of 95 % is 2. Therefore, the expanded measurement uncertainty for the 3D radius of a Rockwell hardness diamond indenter measured using the CLSM is 0.80 µm. The measurement uncertainty budget is presented in Table 10.

Uncertainty source	Standard uncertainty $u(x_i)$	Sensitivity coefficient c_i	Contribution to combined standard uncertainty $u_i(y)$	Degrees of freedom ν_i
Average of repeated value	0.08 µm	1	0.08 µm	7
Instrument resolution	0.01 µm	1	0.01 µm	Inf
Transfer standard	0.25 µm	1	0.25 µm	Inf
Correction factor	0.3 µm	1	0.3 µm	Inf
Sample tilt	0.06 µm	1	0.06 µm	7
	Combined standard uncertainty $u_c(y)$			0.40 µm
	k-factor (95 % level of confidence)			2
	Expanded uncertainty *U*			0.80 µm

Table 10: Measurement uncertainty budget for the measurement of the 3D radius of the spherical tip of a Rockwell hardness diamond indenter using the CLSM with a 50x objective lens

https://doi.org/10.7795/110.20250619

7. Measurement Uncertainty Budget for Rockwell Hardness

In this section, the existing and improved measurement uncertainty budgets for Rockwell hardness scale HRC are presented. Naturally, the measurement uncertainty calculations are transferable to other scales with the proper consideration of the sensitivity coefficients. For better resolution of the hardness levels, the scale HRC is subdivided into three groups:

- Soft (20 HRC to 25 HRC)
- Medium (40 HRC to 45 HRC)
- Hard (60 HRC to 65 HRC)

The sensitivity coefficients are obtained from [103] and listed in Table 11.

Uncertainty source	Symbol	Unit	Sensitivity coefficients		
			Soft	Medium	Hard
Preliminary test force	F_0	N	0.12	0.07	0.05
Total test force	F	N	-0.04	-0.03	-0.02
Indenter cone angle	θ	°	1.6	0.8	0.4
Indenter radius	R	µm	0.015	0.03	0.05
Indentation depth	h	µm	-0.5	-0.5	-0.5
Indentation velocity	v	µm s^{-1}	-0.02	0	0.03
Preliminary force duration	t_0	s	0.01	0.005	0.004
Total force duration	t	s	-0.07	-0.04	-0.03

Table 11: The sensitivity coefficients of the sources of uncertainty

The uncertainty budgets for the existing and for the improved HRC measurements are presented in Table 12 and Table 13, respectively. The respective units for the estimated values in the tables are the same as those listed in Table 11. In light of the work carried out, the uncertainty contributions of the indenter radius, indentation speed and holding times have been reduced. For soft and medium-hardness materials, the reduction in measurement uncertainty is 0.06 HRC, whereas for hard materials the reduction is 0.2 HRC. This indicates that the improvement in the calibration of the tip radius is successful. It must be mentioned that the dispersion due to the inhomogeneity of the hardness of the material is not included in this budget. Furthermore, the uncertainty of

https://doi.org/10.7795/110.20250619

the average of repeated hardness measurements is omitted, as this is specific to every hardness reference block. In conclusion, the new measurement uncertainty of Rockwell hardness testing for HRC at PTB is 0.2 HRC. This, however, must be validated through comparison measurements and a subsequent corresponding Calibration and Measurement Capability (CMC) entry.

Sources	Estimated value	Standard uncertainty $u(x_i)$	Uncertainty contribution $u_i(y)$		
			Soft (20 HRC – 25 HRC)	Medium (40 HRC – 45 HRC)	Hard (60 HRC – 65 HRC)
F_0	0.2	0.12	1.4×10^{-2}	8.1×10^{-3}	5.8×10^{-3}
F	1.5	0.87	3.5×10^{-2}	2.6×10^{-2}	1.7×10^{-2}
θ	0.1	0.06	9.2×10^{-2}	4.6×10^{-2}	2.3×10^{-2}
R	4	2.31	3.5×10^{-2}	6.9×10^{-2}	1.2×10^{-1}
h	0.05	0.03	1.4×10^{-2}	1.4×10^{-2}	1.4×10^{-2}
v	5	2.89	5.8×10^{-2}	0.0×10^{0}	8.7×10^{-2}
t_0	1.5	0.87	8.7×10^{-3}	4.3×10^{-3}	3.5×10^{-3}
t	1	0.58	4.0×10^{-2}	2.3×10^{-2}	1.7×10^{-2}
Combined standard uncertainty $u_c(y)$			0.13	0.09	0.15
Expanded uncertainty U			0.26	0.18	0.30

Table 12: Current measurement uncertainty budget for Rockwell hardness HRC

https://doi.org/10.7795/110.20250619

Sources	Estimated value	Standard uncertainty $u(x_i)$	Uncertainty contribution $u_i(y)$		
			Soft (20 HRC – 25 HRC)	Medium (40 HRC – 45 HRC)	Hard (60 HRC – 65 HRC)
F_0	0.2	0.12	1.4×10^{-2}	8.1×10^{-3}	5.8×10^{-3}
F	1.0	0.58	2.3×10^{-2}	1.7×10^{-2}	1.2×10^{-2}
θ	0.1	0.06	9.2×10^{-2}	4.6×10^{-2}	2.3×10^{-2}
R	1	0.58	8.7×10^{-3}	1.7×10^{-2}	2.9×10^{-2}
h	0.05	0.03	1.4×10^{-2}	1.4×10^{-2}	1.4×10^{-2}
v	1	0.58	1.2×10^{-2}	0.0×10^{0}	1.7×10^{-2}
t_0	0.5	0.29	2.9×10^{-3}	1.4×10^{-3}	1.2×10^{-3}
t	0.2	0.12	8.1×10^{-3}	4.6×10^{-3}	3.5×10^{-3}
Combined standard uncertainty $u_c(y)$			0.10	0.06	0.05
Expanded uncertainty U			0.20	0.12	0.10

Table 13: Measurement uncertainty budget for Rockwell hardness HRC after improvements

https://doi.org/10.7795/110.20250619

8. Future Work and Conclusion

In alignment with the overarching aims and objectives of this research work, three main aspects of Rockwell hardness testing have been identified and addressed. Firstly, a universal automated approach for calibrating Rockwell hardness reference blocks has been introduced. This calibration method has been shown to be user-friendly, time and cost-efficient, and it importantly advances the development of a unified Rockwell hardness scale by strictly adhering to the internationally accepted measurement recommendations. Key parameters influencing the universal characteristic curves that are required for the automation have been identified, and methods for their determination have been proposed. Interlaboratory comparisons demonstrated that this technique is compatible with any computerized Rockwell hardness testing machine. Future efforts pertaining to this work must be concentrated on improving the characteristic curves for Rockwell scales, which use a spherical indenter and lower test forces.

Secondly, the correction of measured Rockwell hardness values as a function of the indenter's geometry considering the hardness level of the material is investigated. A handful number of correction methods exist. An improvement on one such empirical method has been undertaken, and it has been compared to the statistical based correction method (group standard method) that is currently in use. The results of the comparison are satisfactory. Additionally, the efficacy of the modified empirical method is verified by implementing it on three different indenters. The method has been demonstrably effective in correcting the deviations in hardness values of soft and hard materials. However, the extent of correction is inadequate in cases of medium-hardness materials. It has also been identified that accurate geometric properties need to be inserted into the correction functions to get reliable hardness corrections. Future work in this regard must focus on incorporating the properties of the blending region into the derivation. Moreover, an iterative approach to correct the hardness values based on the inclusion of the radii and opening angle as a function of the indenter's height could yield better correction results. Improvements in the definition of this method would also facilitate the estimation of measurement uncertainty of Rockwell hardness testing using a Monte-Carlo simulation.

Finally, an exhaustive study has been conducted to enhance the calibration of the tip radius of a Rockwell diamond hardness indenter. In light of the high volume of calibration requests and the pivotal role the indenter tip radius plays in the Rockwell scale, it is imperative that a harmonious balance between calibration cost and metrological quality be attained. This is equally applicable to the selection of the measurement instrument and the method of evaluation of the acquired measurement data. Given the circumstances, a confocal laser scanning microscope (CLSM) has been chosen as the primary measuring instrument. This is due to the instrument's fast measurement capability, acquisition of the entire surface topography and its non-contact mode of measurement.

https://doi.org/10.7795/110.20250619

A systematic comparison of the measurement data and the measured radius value of indenters between CLSM and well-established, traceable tactile instruments reveals a substantial disagreement. This discrepancy persists despite the CLSM having been calibrated. The source of the discrepancy between the measurement results has been identified as the shape of the measurand. It has been demonstrated that measurands whose surface slope varies within the field of view of the objective lens result in a distortion of the extracted point cloud data, which subsequently introduces a deviation in the measured radius value. The percentage deviation between the measured radii obtained from the CLSM (50x objective lens) and the tactile methods for spheres of different sizes has been quantified. It has been shown for the very first time that the error is proportional to the size of the sphere.

For the purpose of calibrating the radius of a Rockwell diamond indenter, a calibration strategy has been presented that utilizes a transfer standard (grade 3 ruby sphere with a radius of 200 µm). In addition to the determination of the correction factor for the CLSM, the factors that influence the measured radius value from a CLSM have been studied. Crucially, the amount of error depends on the type of confocal microscope and the chosen objective lens, in some cases exceeding 3 µm. The remainder of the factors have been investigated for a specific CLSM and objective lens. Utilizing the quantification of these factors, a measurement uncertainty budget specifically for the Rockwell diamond indenter is created. From this point moving forward, the radius of a Rockwell diamond indenter can be calibrated with an uncertainty of 0.8 µm, which amounts to a four-fold improvement.

A novel method of evaluation of the radius measurement data of the Rockwell diamond indenter has been proposed. This method capitalizes on the 3D point cloud data extracted by the CLSM and calculates a 3D radius in contrast to the conventional 2D radius based on the average of individual radii of 2D profiles. It has been substantiated that a 3D radius is a better representation of the spherical region than a 2D radius. In addition, this method of evaluation is used to describe the spherical region of the Rockwell diamond indenter in terms of the 3D radius as a function of the height (R-h curve).

With the help of R-h curves, the overall shape of the Rockwell diamond indenter can be compared in a single observation. It has been revealed that the spherical region of Rockwell diamond indenters can exhibit remarkable dissimilarities and yet be calibrated with the same radius value. This indicates that the quality of the Rockwell diamond indenters must be improved and also that the standards must elaborate on the evaluation procedure of the radius calibration, such as the height of evaluation. Both of these are prerequisites for fostering overall measurement comparability.

Much work has gone into the research of the characterization of the indenter tip radius. The characterization and measurement of the opening angle of the Rockwell indenter is recommended for future work. Utilizing the results from this work, the measurement uncertainty of Rockwell hardness testing at the PTB for the HRC scale has been reduced from 0.3 HRC to 0.2.

https://doi.org/10.7795/110.20250619

9. List of References

[1] Cambridge dictionary *Cambridge University Press & Assessment* Online [accessed 02 May 2024] (https://dictionary.cambridge.org/dictionary/english/hardness)

[2] Meyer M A D T 1951 *Some aspects of the hardness of metals* (The Hague: Excelsiors Foto-Offset)

[3] Mott B W 1956 *Die Mikrohärteprüfung* (translated und published by Karl F. Frank, Stuttgart: Berliner Union)

[4] Herrmann K 2011 *Hardness testing: principles and applications* (Ohio: ASM International, Materials Park)

[5] Walley S M 2012 Historical origins of indentation hardness testing *Materials Science and Technology* **28** 1028–44

[6] Sneddon I N 1965 The relation between load and penetration in the axisymmetric Boussinesq problem for a punch of arbitrary profile *International Journal of Engineering Science* **3** 47–57

[7] Oliver W C and Pharr G M 1992 An improved technique for determining hardness and elastic modulus using load and displacement sensing indentation experiments *Journal of Materials Research* **7** 1564–83

[8] Fischer-Cripps A C 2004 *Nanoindentation Second Edition* (New York: Springer)

[9] Maier-Kiener V, Lawrence S K and Merle B 2022 30 Years of Oliver–Pharr: Then, Now and the Future of Nanoindentation *JOM* **74** 2177–8

[10] Gogolinskii K V, Syasko V A, Umanskii A S, Nikazov A A and Bobkova T I 2019 Mechanical properties measurements with portable hardness testers: advantages, limitations, prospects *Journal of Physics: Conference Series* **1384** 012012

[11] Vaško A, Sovík J and Sedliačková Z 2019 Accuracy of Portable Hardness Testers *Manufacturing Technology* **19** 886–90

[12] Broitman E 2016 Indentation Hardness Measurements at Macro-, Micro-, and Nanoscale: A Critical Overview *Tribology Letters* **65**

https://doi.org/10.7795/110.20250619

[13] John V 1992 *Testing of materials* (London: Macmillan)

[14] Schmitt R and Dietrich E 2023 *Handbuch Messtechnik in der industriellen Produktion* (Carl Hanser Verlag GmbH Co KG)

[15] DIN EN ISO 6506-1:2014 Metallic materials – Brinell hardness test – Part 1: Test method

[16] DIN EN ISO 6507-1:2018 Metallic materials – Vickers hardness test – Part 1: Test method

[17] Petik F 1991 The Unification of Hardness Measurement *Bureau International de Metrologie Legale (OIML) Paris*

[18] VanLandingham M R 2003 Review of instrumented indentation *Journal of Research of the National Institute of Standards and Technology* **108** 249

[19] Qian L, Li M, Zhou Z, Yang H and Shi X 2005 Comparison of nano-indentation hardness to microhardness *Surface and Coatings Technology* **195** 264–71

[20] Menčík J 2006 Determination of mechanical properties by instrumented indentation *Meccanica* **42** 19–29

[21] Hay J 2009 Introduction to instrumented indentation testing *Experimental Techniques* **33** 66–72

[22] Mahoney D D and Mann A B 2019 Nanoindentation analysis methods examined with finite element simulations *International Journal of Materials Research* **110** 91–100

[23] Hay J L and Pharr G M 2000 Instrumented Indentation Testing *ASM International eBooks* 232–43

[24] DIN EN ISO 14577-1:2015 Metallic materials – Instrumented indentation test for hardness and materials parameters – Part 1: Test method

[25] Gadelrab K R, Bonilla F A and Chiesa M 2012 Densification modeling of fused silica under nanoindentation *Journal of Non-crystalline Solids* **358** 392–8

https://doi.org/10.7795/110.20250619

[26] Rockwell H M and Rockwell S P 1919 Hardness-Tester *United States Patent Office* Patent No. 1294171

[27] Wilson C H 1926 Penetrator for testing penetration hardness *United States Patent Office* Patent No. 1571310

[28] Lysaght V E 1949 *Indentation Hardness Testing* Wilson Mechanical Instruments Co. (New York: Reinhold Publishing Corporation)

[29] Chandler H 1999 *Hardness testing Second Edition* (USA: ASM International)

[30] Mitchell D, Ma L, Low S and Fink J 2006 Effects of Steel and Tungsten Carbide Ball Indenters on Rockwell Hardness Measurements *Journal of Testing and Evaluation* **34** 100048

[31] Skliarov V, Zalohin M and Dovzhenko J 2017 FEM simulation and experimental measurement of hardness by the Superficial Rockwell HRT scale using the steel and tungsten carbide spherical indenters *Proceedings of SPIE* **10165**

[32] Sundararajan G and Roy M 2001 Hardness Testing *Encyclopedia of Materials: Science and Technology* 3728–36

[33] Fidelus J D, Germak A and Origlia C 2021 Bilateral comparison in Rockwell C hardness scale between INRiM and GUM *Measurement: Sensors* **18** 100360

[34] Low S R 2001 *Rockwell hardness measurement of metallic materials* (Gaithersburg: National Institute of Standards And Technology)

[35] CCM Working Group on Hardness (CCM-WGH) [accessed 21 May 2024] (https://www.bipm.org/en/committees/cc/ccm/wg/ccm-wgh)

[36] DIN EN ISO 6508:2015-1 Metallic materials – Rockwell hardness test – Part 1: Test method

[37] DIN EN ISO 6508:2015-2 Metallic materials – Rockwell hardness test – Part 2: Verification and calibration of testing machines and indenters

https://doi.org/10.7795/110.20250619

[38] DIN EN ISO 6508:2015-3 Metallic materials – Rockwell hardness test – Part 3: Calibration of reference blocks

[39] Barbato G, Brondino G and Galetto M 2003 Force calibration of instrumented hardness testers *Proceedings XVII IMEKO World Congress, Metrology in the 3rd Millennium (Dubrovnik, Croatia)*

[40] Sanjid M A and Sharma R 2024 A novel method for the calibration of the displacement encoder of the Rockwell hardness tester *MAPAN-Journal of Metrology Society of India*

[41] Petik F 1989 Hardness standard equipment *Bureau International de Metrologie Legale (OIML) Paris*

[42] Thomsen-Schmidt P 2011 Characterization of a traceable profiler instrument for areal roughness measurement *Measurement Science and Technology* **22** 094019–9

[43] Dai G, Pohlenz F, Xu M, Koenders L, Danzebrink H U and Wilkening G 2006 Accurate and traceable measurement of nano- and microstructures *Measurement Science and Technology* **17** 545–52

[44] Dai G, Zhu F and Fluegge J 2015 High-speed metrological large range AFM Measurement Science and Technology **26** 095402–2

[45] Jusko O, Gerwien N, Hagedorn D, Härtig F, Heyne H P, Langner U, Löffler F, Metschke S, Neugebauer M and Reimann H 2010 Final manufacturing and measurement of satellite proof masses for the MICROSCOPE project *Proceedings of SPIE* **7544** pp. 108–117

[46] Dai G, Neugebauer M, Stein M, Bütefisch S and Neuschaefer-Rube U 2016 Overview of 3D micro- and nanocoordinate metrology at PTB *Applied Sciences* **6** 257–7

[47] Leach R 2016 *Fundamental principles of engineering nanometrology* (Elsevier Science Ltd.)

https://doi.org/10.7795/110.20250619

[48] Song J F, Low S, Pitchure D, Germak A, DeSogus S, Polzin T, Yang H Q, Ishida H and Barbato G 1997 Establishing a world-wide unified Rockwell hardness scale with metrological traceability *Metrologia* **34** 331–42

[49] Sawa T 2018 Current state of Rockwell hardness in the world *Journal of Physics: Conference Series* **1065** 062003

[50] Sawa T 2020 Research on dispersion in indenter and reference block for Rockwell hardness test *ACTA IMEKO* **9** 221

[51] Desogus S, Germak A, Origlia C and Barbato G 2006 Performance tests for qualifying metrological Rockwell indenters *XVIII IMEKO World Congress Metrology for a sustainable development (Rio de Janeiro, Brazil)*

[52] Grziwotz D, Brand U, Menelao F and Schilling M 2017 Automation of the Rockwell standard measuring machine of the PTB *IMEKO 23rd TC3, 13th TC5 and 4th TC22 International Conference (Helsinki, Finland)*

[53] He L and Zhang F 2011 The Rockwell hardness primary national machine according to the new international definition *Proceedings of SPIE* **8321** 83211I-1

[54] Kuzu C, Pelit E, Doğan Ç, Okur A T, Meral İ, Yandayan T and Kazmanlı K 2015 A new design and automation of Rockwell hardness standard machine *XXI IMEKO World Congress "Measurement in Research and Industry" (Prague, Czech Republic)*

[55] Loubet J L, Georges J M, Meille G, Blau P J and Lawn B R 1986 Microindentation techniques in materials science and engineering *ASTM STP* **889** 72-89

[56] Hainsworth S V, Chandler H W and Page T F 1996 Analysis of nanoindentation load-displacement loading curves Journal of Materials Research **11** 1987–95

[57] Brand U, Beckert E, Beutler A, Dai G, Stelzer C, Hertwig A, Klapetek P, Koglin J, Thelen R and Tutsch R 2011 Comparison of optical and tactile layer thickness measurements of polymers and metals on silicon or SiO2 *Measurement Science & Technology* **22** 094021–1

https://doi.org/10.7795/110.20250619

[58] Hertz H 1882 Ueber die Berührung fester elastischer Körper *Journal für die reine und angewandte Mathematik (Crelles Journal)* **1882** 156–71

[59] Johnson K L 2004 *Contact mechanics* (Cambridge: Cambridge University Press)

[60] Pharr G M, Herbert E G and Gao Y 2010 The Indentation Size Effect: A Critical Examination of Experimental Observations and Mechanistic Interpretations *Annual Review of Materials Research* **40** 271–92

[61] Sneddon I N 1965 The relation between load and penetration in the axisymmetric boussinesq problem for a punch of arbitrary profile *International Journal of Engineering Science* **3** 47–57

[62] Hawam A A, Hasan E H, El Kassas A M, Mohamed G and Ahmadein M 2019 A Monte Carlo simulator for the estimation of the uncertainty of Brinell hardness 2nd *Int. Conf. on Materials Science and Engineering (ICMSE-2019) (Cairo, Egypt)*

[63] Mahmoud G M and Hegazy R S 2017 Comparison of GUM and Monte Carlo methods for the uncertainty estimation in hardness measurements *International Journal of Metrology and Quality Engineering* **8** 14

[64] Kumar H, Moona G, Arora P K, Haleem A, Singh J, Kumar R and Kumar A 2017 Monte carlo method for evaluation of uncertainty of measurement in brinell hardness scale *Indian Journal of Pure & Applied Physics (IJPAP)* **55** 445–53

[65] Dai G, Herrmann K and Menelao F 2009 Two approaches for enhancing the accuracy of the Rockwell hardness test *Measurement Science and Technology* **20** 065701

[66] Marriner R S 1955 Performance tests on indentors for Rockwell hardness testing *Engineering* 17–19

[67] Schwenk D, Herrmann K, Aggag G and Menelao F 2007 Investigation of a group standard of Rockwell diamond indenters *Proceedings of the HARDMEKO **2007**, Recent Advancement of Theory and Practice in Hardness Measurement (Tsukuba, Japan)*

https://doi.org/10.7795/110.20250619

[68] Schwenk D and Repp I 2015 Modellierung und Simulationsrechnungen zu den Auswirkungen von Abweichungen bei der Prüfvorkraft, Prüfkraft und bei der Geometrie des Eindringkörpers auf den Härtewert nach Rockwell *Tagung Werkstoffprüfung (Bad Neuenahr, Germany)*

[69] Kick F 1885 Das Gesetz der proportionalen Widerstände und seine Anwendungen: Nebst Versuchen über das Verhalten verschiedener Materialien bei gleichen Formänderungen sowohl unter der Presse als dem Schlagwerk *Verlag von Arthur Felix (Leipzig)* (in German)

[70] Wood J G and Cotter J 1985 Performance predications of Rockwell indenters *NPL Report MOM* **73**

[71] Petik F 1984 Hardness test blocks and indenters *Bureau International de Metrologie Legale (OIML) Paris*

[72] El-Sherbiny M, Hegazy R, Ibrahim M and Abuelezz A E 2012 The influence of geometrical tolerances of Vickers indenter on the accuracy of measured hardness *International Journal of Metrology and Quality Engineering* **3** 1–6

[73] Herrmann K, Jennett N M, Wegener W, Meneve J, Hasche K and Seemann R 2000 Progress in determination of the area function of indenters used for nanoindentation *Thin Solid Films* **377-378** 394–400

[74] Song J and Low S 2012 Development of NIST standard reference meterial (SRM) Rockwell hardness diamond indenters *XX IMEKO World Congress, Metrology for Green Growth (Busan, Republic of Korea)*

[75] Cui Y, Ye M, Zhang F and Liu J 2020 A method of measuring the arc radius of Rockwell diamond indenter *IOP Conference Series: Materials Science and Engineering* **784** 012011–1

[76] Barbato G, Galetto M, Germak A and Mazzoleni F 1998 Influence of the indenter shape in Rockwell hardness test *Proceedings of the HARDMEKO* **98** 53-60 *(Beijing, China)*

[77] Yamashiro S and Uemura Y 1961 Die in die Rockwell-Härteskalen eingehenden Fehler in Folge ungenauer Prüfkraft und die Form der Eindringkörper *VDI Berichte Nr*. **41** 109-121

https://doi.org/10.7795/110.20250619

[78] Germak A, Herrmann K, Dai G and Li Z 2006 Development of calibration methods for hardness indenters *VDI-Berichte Nr.* **1948** 13-26

[79] Li Z, Brand U, Menelao F, Herdin M and Felgner A 2017 A non-imaging optical system for characterisation of ball-shaped micro-indenters *Measurement* **107** 165–71

[80] Germak A and Origlia C 2011 Investigations of new possibilities in the calibration of diamond hardness indenters geometry *Measurement* **44** 351–8

[81] 2024 Good practice guide on the selection of instrumentation for optical roughness measurements with CM, CSI and FV *Project name 20IND07 TracOptic* [accessed 25 October 2024] (https://www.ptb.de/empir2021/fileadmin/documents/empir-2021/tracoptic/documents/GPG1_Instrumentation_for_Optical_Roughness_Measurements.pdf)

[82] Song J F, Low S and Ma L 2000 Form error and hardness performance of Rockwell diamond indenters *XVI IMEKO World Congress (Vienna, Austria)*

[83] Brice L, Davis F and Crawshaw A 2003 Uncertainty in hardness measurement *NPL Report CMAM* **87**

[84] Forbes A B 1991 Least-squares best-fit geometric elements *NPL Report No.: DITC* **140/89**

[85] Rachakonda P, Muralikrishnan B, Cournoyer L, Cheok G, Lee V, Shilling M and Sawyer D 2017 Methods and considerations to determine sphere center from terrestrial laser scanner point cloud data *Measurement Science and Technology* **28** 105001

[86] Nečas D and Klapetek P 2012 Gwyddion: an open-source software for SPM data analysis *Cent. Eur. J. Phys.* **10** 181–8

[87] Song J F, Low S, Ptchure D and Vorburger T V 1996 Standard grade Rockwell diamond indenters – A key to a worldwide unified Rockwell hardness scale *Proceedings of National Conference of Standard Laboratory (Anaheim, USA)*

https://doi.org/10.7795/110.20250619

[88] Ma L, Low S, Zhou J, Song J F and deWit R 2002 Simulation and prediction of hardness performance of Rockwell diamond indenters using finite-element analysis *Journal of Testing and Evaluation* **30** 265

[89] Rahlves M, Roth B and Reithmeier E 2015 Systematic errors on curved microstructures caused by aberrations in confocal surface metrology *Optics Express* **23** 9640–0

[90] Béguelin J, Scharf T, Noell W and Voelkel R 2020 Correction of spherical surface measurements by confocal microscopy *Measurement Science and Technology* **31** 075002–2

[91] Ritter M, Dziomba T, Kranzmann A and Koenders L 2007 A landmark-based 3D calibration strategy for SPM *Measurement Science and Technology* **18** 404–14

[92] Bermudez C, Felgner A, Martinez P, Matilla A, Cadevall C and Artigas R 2018 Residual flatness error correction in three-dimensional imaging confocal microscopes *Proc. SPIE* **10678**

[93] Dai G, Koenders L, Fluegge J and Hemmleb M 2018 Fast and accurate: high-speed metrological large-range AFM for surface and nanometrology *Measurement Science and Technology* **29** 054012

[94] Martínez A M and de Vicente y Oliva J 2019 Industrial calibration procedure for confocal microscopes *Materials* **12** 4137

[95] Gao S, Felgner A, Hueser D, Wyss S and Brand U 2023 Characterization of the maximum measurable slope of optical topography measuring instruments *Proc. of SPIE* **12618** 126182L

[96] Moelle C, Klose S, Szücs F, Fecht H J, Johnston C, Chalker P R and Werner M 1997 Measurement and calculation of the thermal expansion coefficient of diamond *Diamond and related materials* **6** 839–42

[97] Zong W J, Wu D and He C L 2017 Radius and angle determination of diamond Berkovich indenter *Measurement* **104** 243–52

https://doi.org/10.7795/110.20250619

[98] Puranto P, Zhang Q, Nyang'au W O, Langfahl-Klabes J, Thiesler J, Zackaria M, Li Z, Wasisto H S, Peiner E and Brand U 2021 Influence of eccentric nanoindentation on top surface of silicon micropillar arrays *Journal of physics. Conference series* **1837** 012008–8

[99] Daul L 2023 Kapazitive Verschiebesensoren: Einfluss von Oberflächenrauheit und Patch-Potentialen *Berichte aus dem Institut für Elektrische Messtechnik und Grundlagen der Elektrotechnik Mensch und Buch (Berlin*)

[100] Bei H, George E P, Hay J L and Pharr G M 2005 Influence of indenter tip geometry on elastic deformation during nanoindentation *Physical Review. Letters* **95** 045501

[101] Zhou Y, Ghim Y-S, Fard A and Davies A 2013 Application of the random ball test for calibrating slope-dependent errors in profilometry measurements *Applied optics* **52** 5925–5

[102] 2008 Evaluation of measurement data – Guide to the expression of uncertainty in measurement *JCGM **100:2008** GUM 1995 with minor corrections*

[103] 2011 Guidelines on the estimation of uncertainty in hardness measurements *EURAMET cg-16*

[104] Riehle F, Gill P, Arias F and Robertsson L 2018 The CIPM list of recommended frequency standard values: guidelines and procedures *Metrologia* **55** 188–200

[105] Stone J A, Decker J E, Gill P, Juncar P, Lewis A, Rovera G D and Viliesid M 2009 Advice from the CCL on the use of unstabilized lasers as standards of wavelength: the helium–neon laser at 633 nm *Metrologia* **46** 11–18

https://doi.org/10.7795/110.20250619

10. Appendix

https://doi.org/10.7795/110.20250619

Appendix 1: Characteristic curves for the Rockwell scale HRA

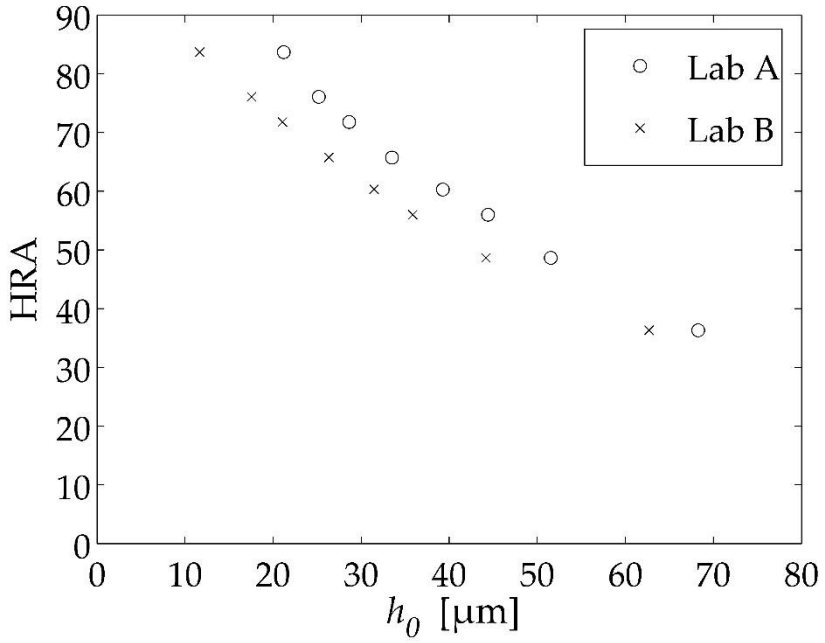

Machine-dependent characteristic curves to estimate the hardness value

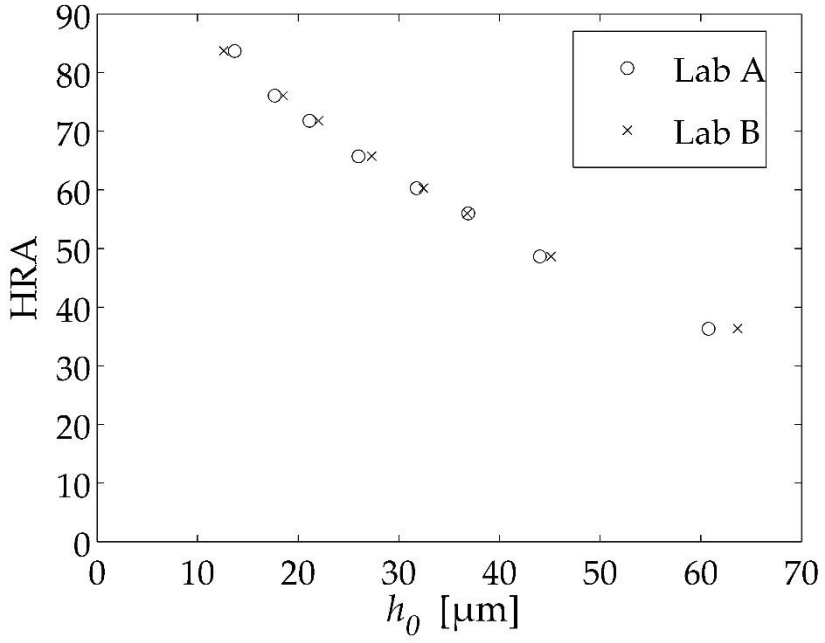

Machine-independent characteristic curves to estimate the hardness value

https://doi.org/10.7795/110.20250619

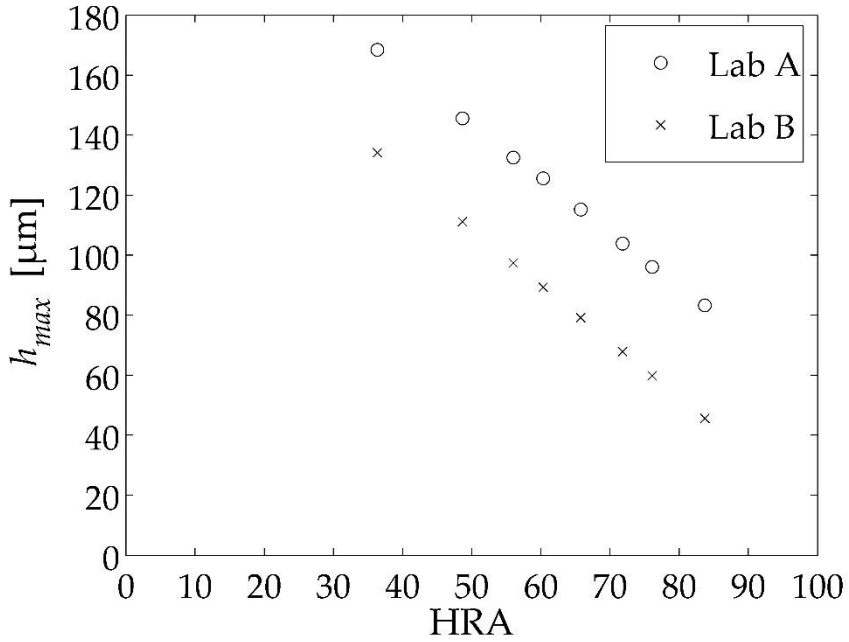

Machine-dependent characteristic curves to estimate the indentation depth h_{max}

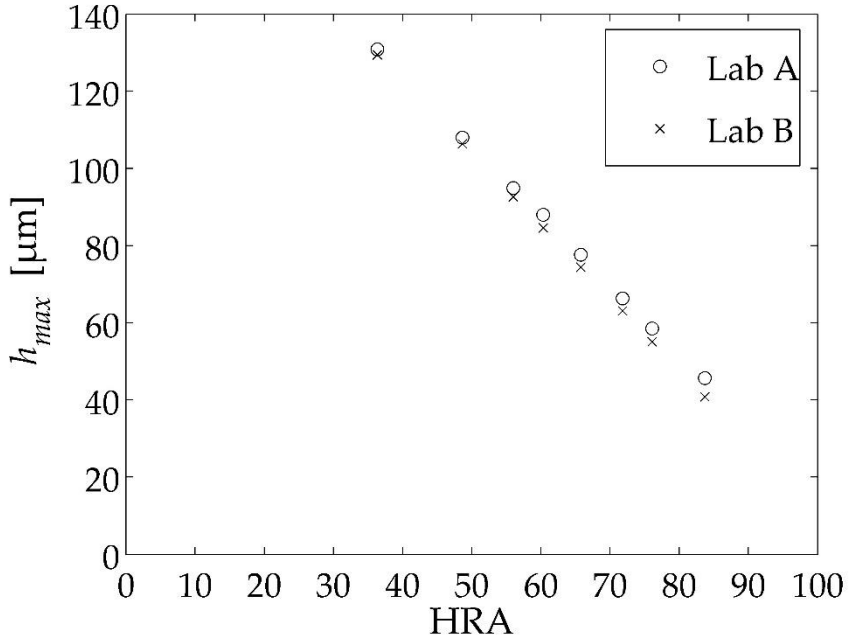

Machine-independent characteristic curves to estimate the indentation depth h_{max}

https://doi.org/10.7795/110.20250619

Appendix 2: Characteristic curves for the Rockwell scale HRD

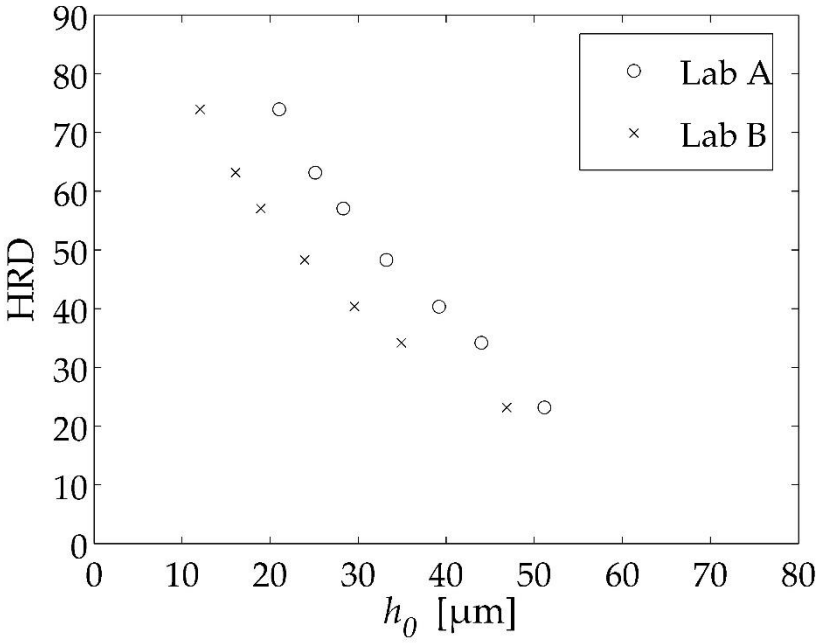

Machine-dependent characteristic curves to estimate the hardness value

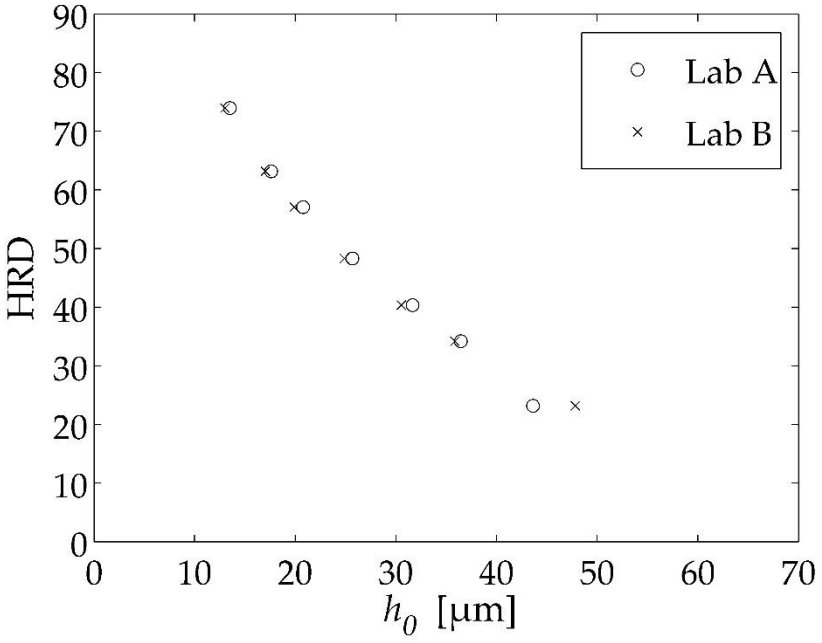

Machine-independent characteristic curves to estimate the hardness value

https://doi.org/10.7795/110.20250619

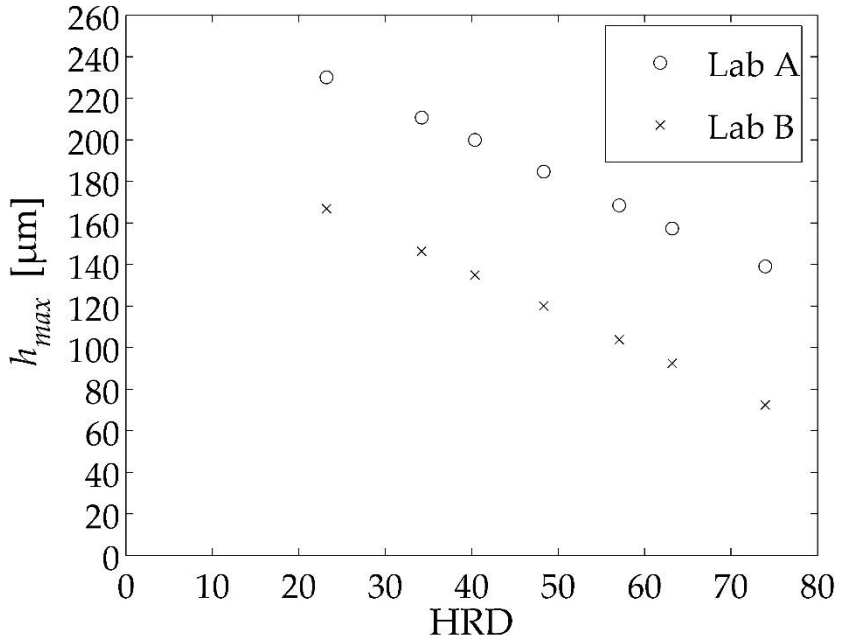

Machine-dependent characteristic curves to estimate the indentation depth h_{max}

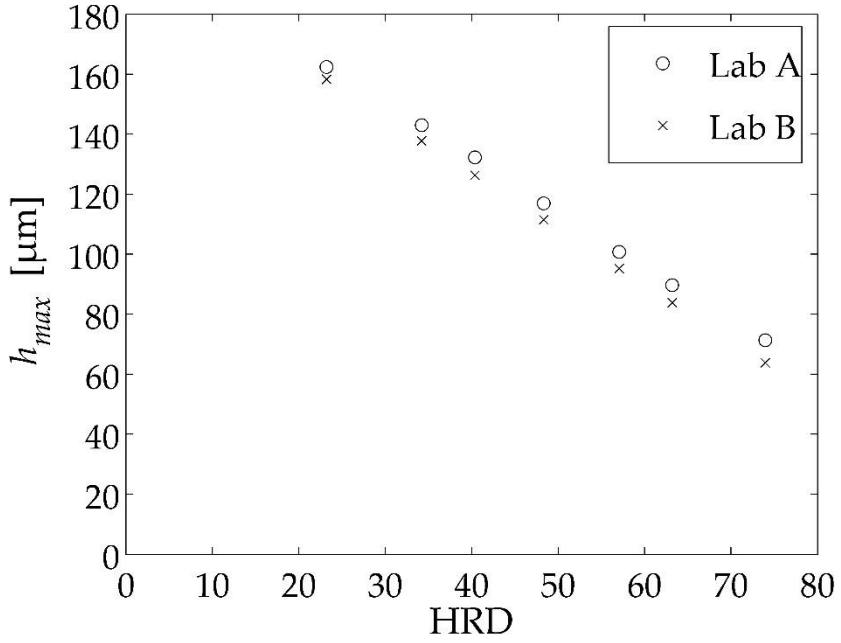

Machine-independent characteristic curves to estimate the indentation depth h_{max}

https://doi.org/10.7795/110.20250619

Appendix 3: Hardness deviations arising from the deviations in the indenter geometry (tip radius) from the nominal values

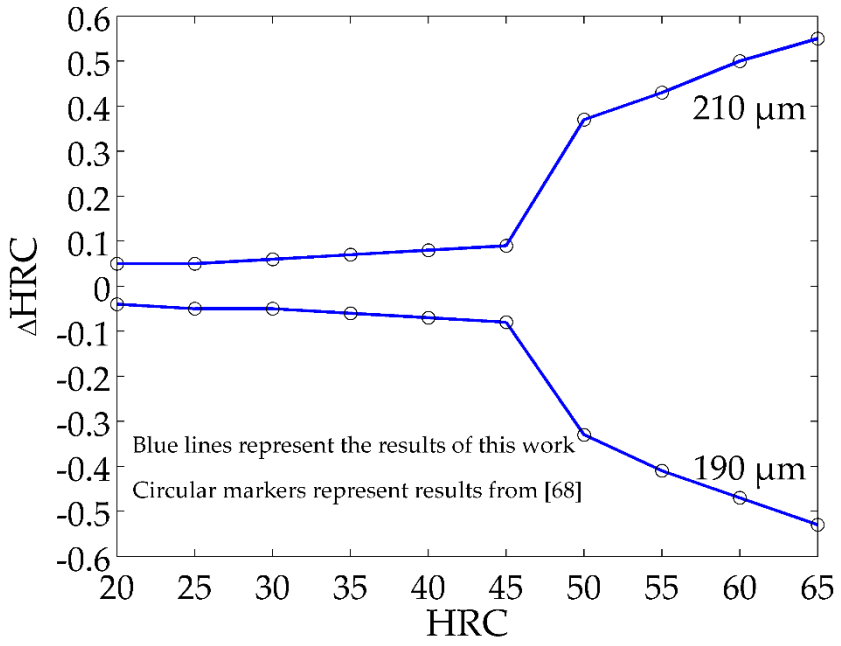

https://doi.org/10.7795/110.20250619

Appendix 4: Intensity images of indenters EDK6, EDK7, and EDK8

EDK6

EDK7

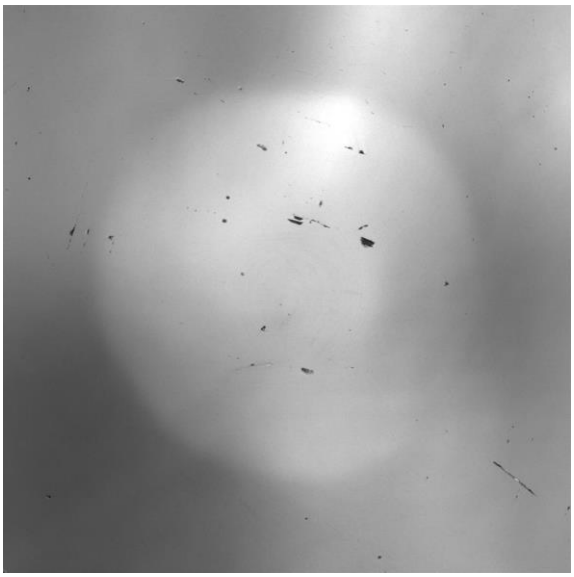

EDK8

https://doi.org/10.7795/110.20250619

Appendix 5: R-h curves for indenters EDK6, EDK7, and EDK8

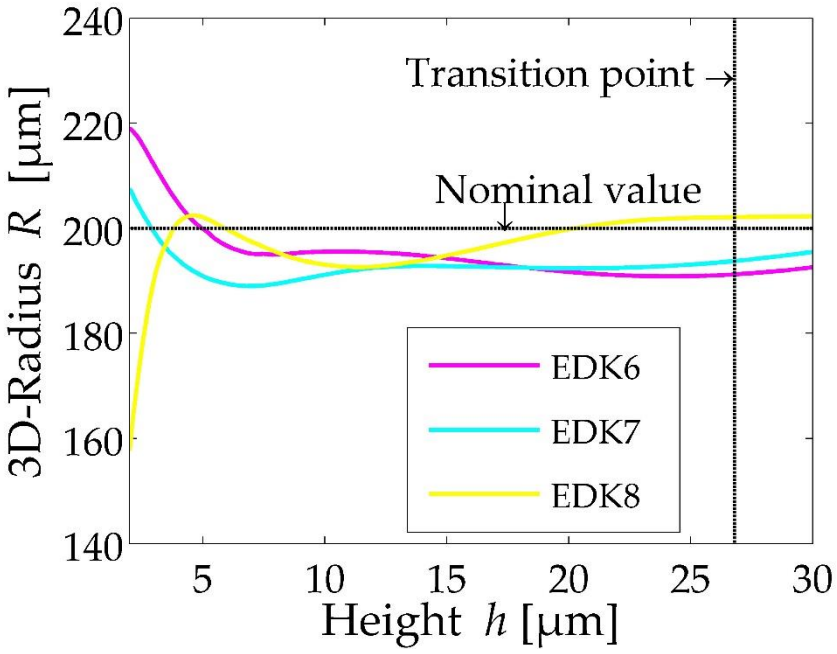

Appendix 6: Deviation plot of the measured radii from the reference instrument HRTS using two confocal microscopes

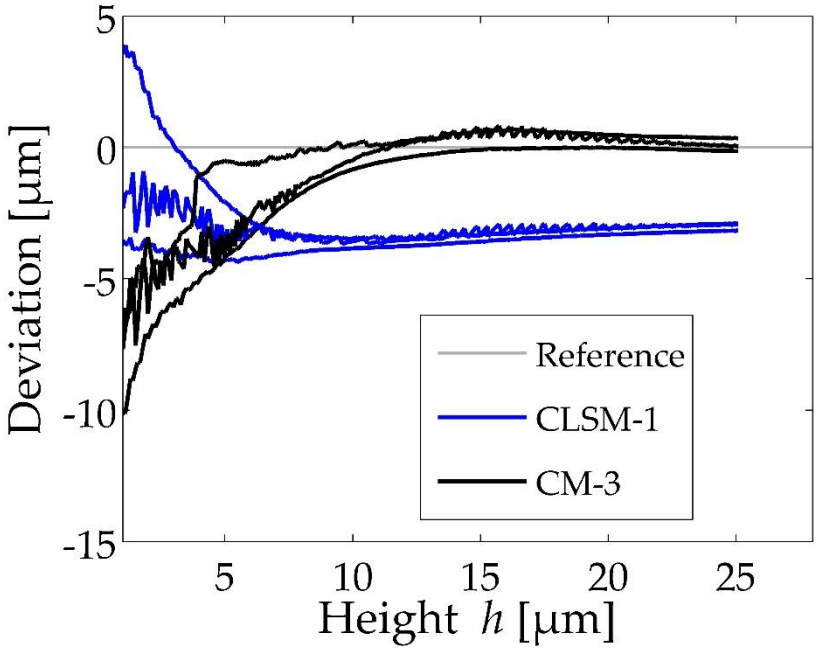

Three Rockwell hardness diamond indenters EDK1, EDK2, and EDK3 are used as measurands

https://doi.org/10.7795/110.20250619

Appendix 7: 3D surface depiction of the sphere D2000 as captured by the 10x, 20x, 50x, and 100x objective lenses of the CLSM

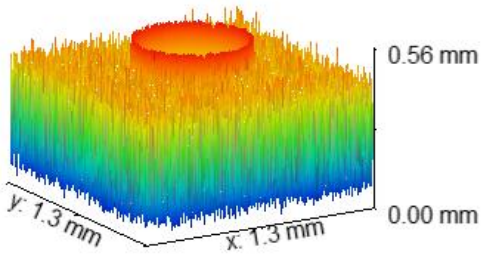

10x

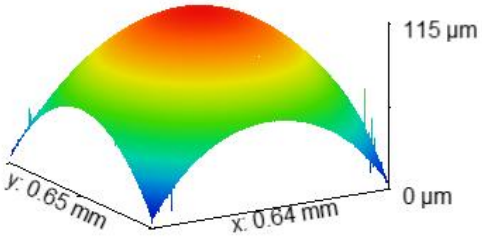

20x

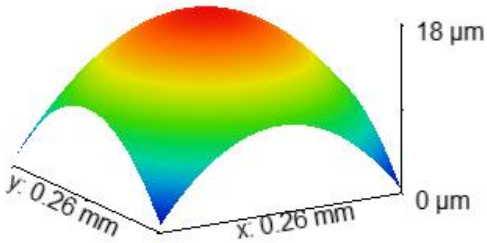

50x

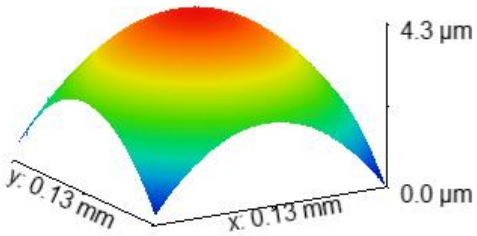

100x

https://doi.org/10.7795/110.20250619

Appendix 8: 3D surface depiction of the sphere D120 as captured by the 10x, 20x, 50x, and 100x objective lenses of the CLSM

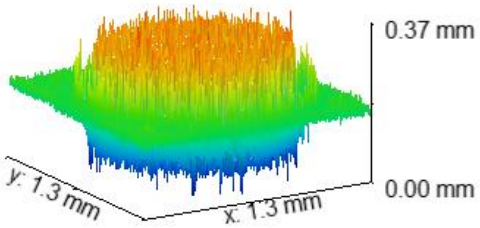

10x

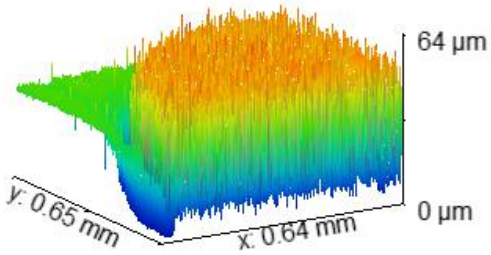

20x

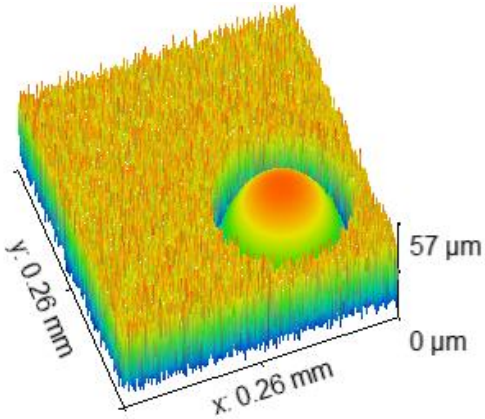

50x

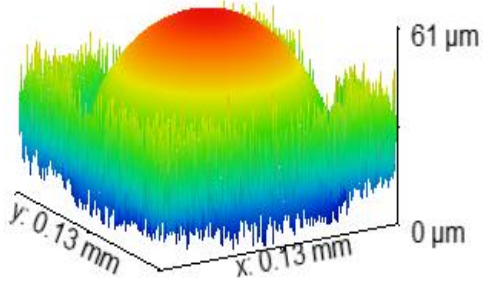

100x

https://doi.org/10.7795/110.20250619

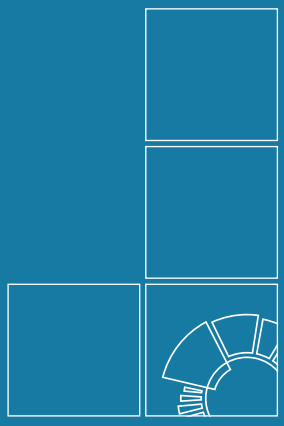

Herausgeber:
Physikalisch-Technische Bundesanstalt
ISNI: 0000 0001 2186 1887
Presse und Öffentlichkeitsarbeit
Bundesallee 100
38116 Braunschweig
Telefon: (05 31) 592-93 21
Telefax: (05 31) 592-92 92
www.ptb.de